



Universiteit  
Leiden  
The Netherlands

## Computer-aided detection of wall motion abnormalities in cardiac MRI

Suinesiaputra, A.

### Citation

Suinesiaputra, A. (2010, March 30). *Computer-aided detection of wall motion abnormalities in cardiac MRI*. *ASCI dissertation series*. Retrieved from <https://hdl.handle.net/1887/15187>

Version: Corrected Publisher's Version

License: [Licence agreement concerning inclusion of doctoral thesis in the Institutional Repository of the University of Leiden](#)

Downloaded from: <https://hdl.handle.net/1887/15187>

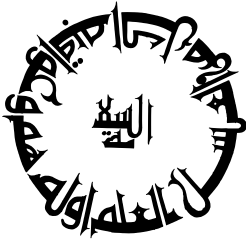
**Note:** To cite this publication please use the final published version (if applicable).

# Computer-Aided Detection of Wall Motion Abnormalities in Cardiac MRI

Avan Suinesiaputra

## Colophon

About the cover:



The cover is an Arabic calligraphy made by an 11-year old M. Zulkhairi Rhiza Tala, which was based on a Kufic inscription written on an 11th–12th century Iranian dish. The text on the dish is translated into: “Science is bitter-tasting (of thinking) at first, but sweeter than honey in the end. Peace.” The dish is currently stored in the Islamic Art collection of the Musée du Louvre, Paris.

Computer-Aided Detection of Wall Motion Abnormalities in Cardiac MRI  
Avan Suinesiaputra

ISBN: 978-90-6464-384-2

Typeset in  $\text{\LaTeX} 2_{\epsilon}$ , generated by pdfTeX ver. 3.1415926-1.40.10-2.2.

Printed by Ponsen & Looijen B.V., the Netherlands.

© 2010 Avan Suinesiaputra, Leiden, the Netherlands

All rights reserved. No part of this publication may be reproduced or transmitted in any form or by any means, electronic or mechanical, including photocopying, recording, or any information storage and retrieval system, without permission in writing from the copyright owner.

# Computer-Aided Detection of Wall Motion Abnormalities in Cardiac MRI

## **Proefschrift**

ter verkrijging van  
de graad van Doctor aan de Universiteit Leiden,  
op gezag van Rector Magnificus prof. mr. P.F. van der Heijden,  
volgens besluit van het College voor Promoties  
te verdedigen op dinsdag 30 maart 2010  
klokke 13:45 uur

door

Avan Suinesiaputra  
geboren te Jakarta, Indonesië  
in 1974

## Promotiecommissie

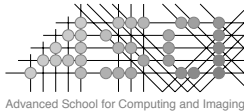
Promotor: Prof. dr. ir. J.H.C. Reiber

Co-promotor: Dr. ir. B.P.F. Lelieveldt

Overige leden: Prof. dr. J.J. Bax

Dr. N. Karssemeijer  
Radboud University Medical Centre, Nijmegen

Prof. dr. ir. M.J.T. Reinders  
Technische Universiteit Delft, Delft



This work was carried out in the ASCI graduate school.  
ASCI dissertation series number 193.

This research was supported by the Dutch Science Foundation (NWO) under an innovational research incentive grant (*vernieuwingsimpuls*) 2001.

Financial support for the publication of this thesis was kindly provided by:

- Bontius Stichting inz. Doelfonds beeldverwerking,
- Foundation Imago,
- ASCI research school, and
- Library of the University of Leiden.

*Papah/Bapak and Mamah/Mamak,  
from whom I receive most of Allah's love through.*



# CONTENTS

<b>Contents</b>	<b>iii</b>
<b>1 Introduction</b>	<b>1</b>
1.1 Imaging techniques for diagnosis of ischaemic heart disease . . . . .	4
1.1.1 Magnetic resonance imaging (MRI) . . . . .	4
1.1.1.1 Resting cine-MR images . . . . .	5
1.1.1.2 Dobutamine stress MR (DSMR) . . . . .	5
1.1.1.3 MR perfusion . . . . .	5
1.1.1.4 Contrast-enhanced MRI (CE-MRI) . . . . .	6
1.1.2 Echocardiography . . . . .	7
1.1.3 <sup>18</sup> F-fluorodeoxyglucose (FDG) PET imaging . . . . .	7
1.1.4 Electrocardiographically-gated perfusion SPECT imaging . . . . .	8
1.2 Computer-assisted diagnosis for ischaemia . . . . .	8
1.3 Motivation and objectives . . . . .	10
1.4 Outline . . . . .	10
1.5 References . . . . .	12
<b>2 Optic flow computation from cardiac MR tagging using a multiscale differential method: A comparative study with Velocity-Encoded MRI</b>	<b>21</b>
<i>Suinesiaputra et. al., Medical Image Computing and Computer-Assisted Intervention, Lecture Notes in Computer Science Series vol. 2878, 483–490, Springer, 2003.</i>	
2.1 Methodology . . . . .	24
2.1.1 Conservation principle in tagging MRI . . . . .	24
2.1.2 The First Order Density Multiscale OFCE . . . . .	24
2.1.3 The multiscale scheme . . . . .	25
2.2 Experimental results . . . . .	26
2.2.1 Clinical Data . . . . .	27
2.2.2 Results . . . . .	27
2.3 Discussion . . . . .	28
2.4 References . . . . .	30
<b>3 Extraction of myocardial contractility patterns from short-axis MR images using Independent Component Analysis</b>	<b>31</b>

*Suinesiaputra et. al., Computer Vision and Mathematical Methods in Medical and Biomedical Image Analysis, Lecture Notes in Computer Science Series vol. 3117, 75–86, Springer, 2004.*

3.1	Methodology . . . . .	34
3.1.1	ICA model . . . . .	34
3.1.2	Geometry-based sorting for ICA modes . . . . .	35
3.1.3	Cluster measurement metrics . . . . .	37
3.2	Experimental results . . . . .	38
3.2.1	Weighting coefficient matrix . . . . .	38
3.2.2	Mean cluster distance . . . . .	39
3.2.3	Cluster analysis . . . . .	40
3.2.4	Separation degree . . . . .	41
3.3	Discussion . . . . .	42
3.4	References . . . . .	43
<b>4</b>	<b>Detecting regional abnormal cardiac contraction in short-axis MR images using Independent Component Analysis</b>	<b>45</b>
	<i>Suinesiaputra et. al., Medical Image Computing and Computer-Assisted Intervention, Lecture Notes in Computer Science Series vol. 3216, 737–744, Springer, 2004.</i>	
4.1	Methodology . . . . .	47
4.1.1	ICA modeling of the normal cardiac contraction . . . . .	47
4.1.2	Determining the number of independent components . . . . .	49
4.1.3	Detection of abnormal contractility patterns . . . . .	50
4.2	Experimental Results . . . . .	51
4.3	Discussion . . . . .	52
4.4	References . . . . .	52
<b>5</b>	<b>Automatic prediction of myocardial contractility improvement in stress MRI using shape morphometrics with Independent Component Analysis</b>	<b>55</b>
	<i>Suinesiaputra et. al., Information Processing in Medical Imaging, Lecture Notes in Computer Science Series vol. 3565, 321–332, Springer, 2005.</i>	
5.1	Methodology . . . . .	58
5.1.1	Modeling contraction of healthy myocardium . . . . .	58
5.1.2	Optimal number of independent components . . . . .	59
5.1.3	Density estimation of coefficient values from the ICA model . . . . .	61
5.2	Experimental Results . . . . .	63
5.2.1	Model construction . . . . .	63
5.2.2	Qualitative prediction results of contractility improvement . . . . .	63
5.3	Discussion . . . . .	66
5.4	References . . . . .	66
<b>6</b>	<b>Automated detection of regional wall motion abnormalities based on a statistical model applied to multi-slice short-axis cardiac MR images</b>	<b>69</b>
	<i>Suinesiaputra et. al., IEEE Trans Med Imaging, 4(28):595–607, 2009.</i>	
6.1	Introduction . . . . .	72
6.1.1	Automated RWMA detection methods . . . . .	72

6.1.2	Sparse decomposition in statistical shape analysis . . . . .	73
6.1.3	Contribution of this chapter . . . . .	74
6.2	Methodology . . . . .	74
6.2.1	Statistical Shape Modeling of Cardiac Contraction . . . . .	74
6.2.2	Myocardial Shape Decomposition with ICA . . . . .	76
6.2.3	Robust Estimation of Independent Components . . . . .	77
6.2.4	Estimating Density Functions of Independent Components . . . . .	79
6.2.5	Detecting Abnormal Regions . . . . .	80
6.3	Experimental Results . . . . .	83
6.3.1	Data description and preprocessing . . . . .	83
6.3.2	Validation Method . . . . .	84
6.3.3	Classification performance . . . . .	86
6.3.4	Disagreement with visual wall motion score . . . . .	86
6.3.5	Disagreement with wall thickening . . . . .	88
6.3.6	Comparison with direct landmark density estimation . . . . .	90
6.4	Discussion . . . . .	91
6.4.1	Method performance . . . . .	91
6.4.2	Study limitations . . . . .	91
6.4.3	Clinical utility . . . . .	92
6.5	Conclusion . . . . .	92
6.6	References . . . . .	93
<b>7</b>	<b>An automated regional wall motion abnormality detection by combining rest and stress cardiac MRI: Correlation with infarct transmural-ity from contrast-enhanced MRI</b>	<b>97</b>
	<i>Suinesiaputra et. al., submitted.</i>	
7.1	Materials and Methods . . . . .	99
7.1.1	Study design . . . . .	99
7.1.2	Data acquisition . . . . .	100
7.1.3	Slice selection . . . . .	100
7.1.4	Myocardial contour delineation and segmental definition . . . . .	101
7.1.5	Normokinetic myocardial shape models . . . . .	101
7.1.6	Building RWMA probability density functions . . . . .	102
7.1.7	RWMA evaluation . . . . .	102
7.1.8	Transmural extent . . . . .	104
7.1.9	Statistical analysis . . . . .	104
7.2	Results . . . . .	105
7.2.1	Rest versus rest-stress data . . . . .	105
7.2.2	Scar tissue detection . . . . .	106
7.2.3	Correlation with infarct transmural-ity . . . . .	107
7.3	Discussion . . . . .	107
7.4	References . . . . .	109
<b>8</b>	<b>Summary</b>	<b>111</b>
8.1	Myocardial wall motion modeling . . . . .	113

8.2	Automated evaluation of regional wall motion abnormalities . . . . .	114
8.3	Automated prediction of functional improvement . . . . .	115
8.4	Future directions . . . . .	116
8.5	References . . . . .	117
<b>9</b>	<b>Samenvatting</b>	<b>119</b>
9.1	Statistische modellering van de wandbeweging van het linkerventrikel . . .	121
9.2	Automatische detectie van afwijkingen in regionale wandbeweging van het LV . . . . .	122
9.3	Automatische bepaling van functionele verbeteringen in wandbeweging .	123
9.4	Vervolgonderzoek . . . . .	124
9.5	References . . . . .	125
	<b>Publications</b>	<b>127</b>
	<b>Acknowledgements</b>	<b>129</b>
	<b>Curriculum vitae</b>	<b>131</b>



# 1

## INTRODUCTION





**Melman:** Yeah. I often doze off while I'm getting an MRI.

**Alex:** Melman, you're not getting an MRI!

**Melman:** CAT scan?

**Alex:** No! No CAT scan! It's a zoo transfer!

**Melman:** ZOO TRANSFER?!

---

MADAGASCAR (2005)

**C**ORONARY artery disease is a condition in which plaque builds up inside the coronary arteries, causing disruption of the supply of oxygen-rich blood to the myocardium. The prevalence, incidence, hospitalization rate and costs of this disease in the developed countries have steadily increased [1]. It has been a leading cause of death in Europe and North America, and it may even accelerate the progression of heart failure, and as such, it is responsible for 70% of congestive heart failure cases [2].

Ischaemia is a condition of the heart when the supply of blood to the myocardium is significantly reduced, mainly as the result of coronary artery disease. The imbalance in supply and demand of oxygen in the circulation leads to functional sequelae known as the ischaemic cascade. This starts with perfusion abnormalities, metabolic changes (*silent ischaemia*), wall motion abnormalities, diastolic dysfunction, systolic dysfunction, angina and ultimately infarction [3, 4]. As a result of chronic contractile dysfunction, myocardium may turn into a hibernating state. Hibernating myocardium is an equilibrational condition after prolonged subacute or chronic ischaemia in which metabolism and contractile function are reduced to match the blood supply. The hibernating myocardium is capable of returning to normal or near-normal function after restoration of an adequate blood supply [5]. Hibernating myocardium thus suggests the presence of viable tissue, which may gain functional improvement after treatment [6]. In the absence of a significant amount of viable myocardium, restoring the blood flow is not beneficial anymore. Assessment of dysfunctional but viable myocardium has become an important determinant in the prognosis of ischaemic heart disease for long term survival.

A common treatment for restoring blood flow to the heart is coronary revascularization. Two common revascularization procedures are coronary artery bypass grafting (CABG) and percutaneous coronary intervention (PCI). CABG restores blood flow of an obstructive coronary artery by rerouting the artery with a new vessel. PCI is performed by angioplasty, i.e., threading a balloon-tipped tube to be inflated, compressing the plaque and dilating the narrowed coronary artery to improve the blood flow again, and then followed by vascular stenting to keep the vessel open. Although overall survival has improved due to these revascularization treatments, the result remains a partial success [7]. This emphasizes the need for and the importance of an early and noninvasive diagnosis and quantification of ischaemic heart disease.

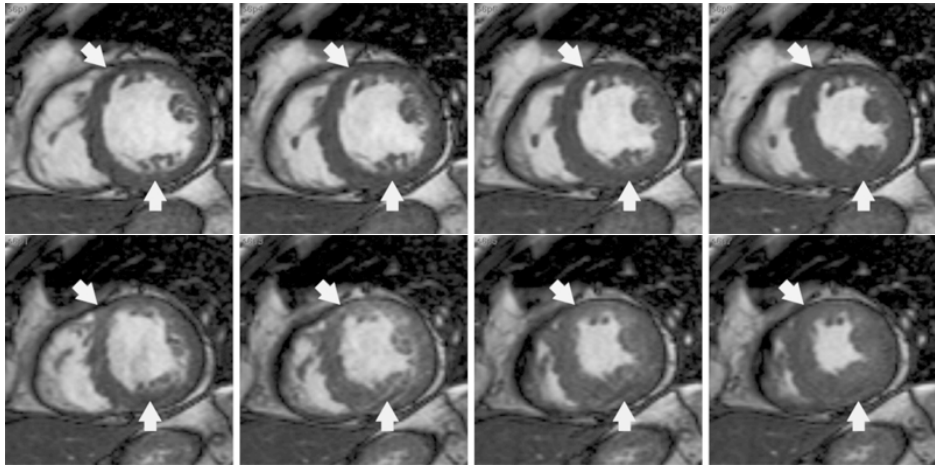


FIGURE 1.1: Resting (TOP) and dobutamine stress (BOTTOM) cine-MR images from the same patient at a single MR acquisition session. An increase of dobutamine-induced wall thickening is visible at the inferior region (the bottom arrows). This indicates a possible viable myocardium. At the anteroseptal region (the top arrows), there is no increase of LV function from rest to stress, which suggests non-viable tissue.

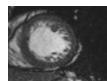
## 1.1 Imaging techniques for diagnosis of ischaemic heart disease

In the last few decades, an enormous amount of research has been carried out towards imaging of ischaemic heart disease. Different image acquisition approaches have emerged, either to detect the disease before symptoms occur, to assess the presence and the extent of the disease in the symptomatic patient, or to monitor the disease progression over time. Particularly for viability assessment, hibernating myocardium can be traced with some imaging techniques, which can detect either the presence of myocardial tissue that contracts if stimulated (wall motion analysis) or the persistence of metabolic activities within the regions of dysfunctional myocardium (perfusion analysis).

Though head-to-head comparisons between imaging techniques have been performed with respect to viability, no single test has been reported to have a perfect or nearly perfect sensitivity and specificity [8]. An integrated use of different image acquisitions is therefore needed in clinical decision making [8, 9]. In the following sections, clinical applicability of different image modalities to assess ischaemic heart disease is briefly presented.

### 1.1.1 Magnetic resonance imaging (MRI)

MRI has a unique position in the management of ischaemic heart disease because it is the only single image modality that allows visualization of all ischaemic events through



different MR protocols [3]. In a single session, perfusion defects, resting cardiac function, stress imaging and infarct images can be acquired with MRI [2, 4, 10]. Hence, MRI has the potential to be implemented as a “one-stop shop” imaging modality for the diagnosis of ischaemic heart disease.

#### 1.1.1.1 Resting cine-MR images

Cine MR images are generally used in standard clinical practice for quantification of global and regional LV functions, e.g., ejection fraction, stroke volume, wall thickening, and wall thickness, because of its superb contrast delineation of myocardium with the blood pool, right ventricle and other tissues. Cine MR imaging captures a full cardiac cycle in an MR time sequence. Hence, cine MRI allows quantification of wall motion as well as end-diastolic wall thickness (EDWT) and systolic wall thickening (SWT), which are key functional parameters for quantifying ischemic heart disease.

#### 1.1.1.2 Dobutamine stress MR (DSMR)

In the assessment of myocardial viability, the presence of contractile reserve is frequently used to identify viable myocardium. Contractile reserve can be assessed by low dose dobutamine injection prior to MR acquisition, which will produce cardiac stress MRI [2, 11]. Contractile reserve is shown by the increase of the dobutamine-induced systolic function compared against the corresponding resting cine-MRI.

The diagnostic procedure with DSMR starts from visual wall motion scoring of myocardial segments in resting MR. Four visual score levels are defined: *normokinetic* (normal), *hypokinetic* (reduced), *dyskinetic* (abnormal) and *akinetic* (no contraction). The hypokinetic score may sometimes be divided into *mild* and *severe* hypokinetic. Subsequently, observers predict functional improvement in non normokinetic segments by comparing cine MR sequences between resting MR and DSMR. Figure 1.1 shows an example of a comparison between resting and dobutamine-stress cine MRI. Observer experience inevitably affects the diagnostic quality of DSMR [12, 13]. Quantitatively, viable myocardium can also be characterized by the preserved EDWT and SWT from rest to stress MR [14, 15].

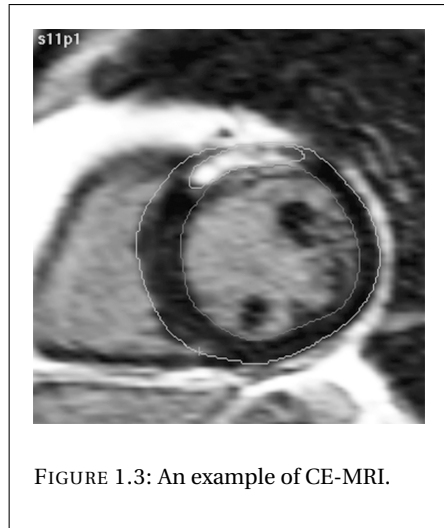
#### 1.1.1.3 MR perfusion

An MR perfusion study is performed by the injection of gadolinium pentaacetic acid (Gd-DPTA) prior acquisition. The contrast agent enables full inspection of myocardial tissue perfusion during the first-pass myocardial intensity enhancement (see Figure 1.2). First-pass MR perfusion images are usually evaluated by an upslope analysis of myocardial time-intensity curves.

Coronary artery disease can be assessed by the combination of rest and stress perfusion studies [16, 17]. During stress, the blood flow through myocardium increases three- to fourfold. The ratio of the maximum blood flow to the baseline, known as myocardial perfusion reserve index (MPRI), has been used as an index of functional severity of a coronary lesion [18].

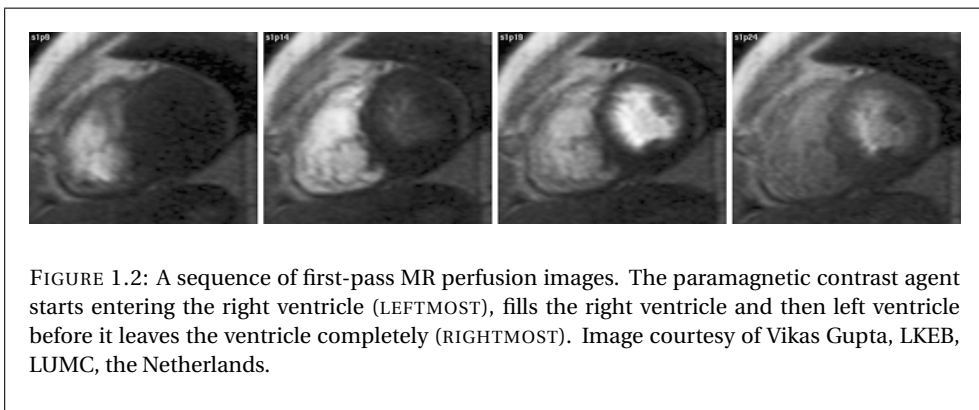
#### 1.1.1.4 Contrast-enhanced MRI (CE-MRI)

Following a rest MR perfusion study, the amount of washed-out contrast agent inside myocardium can be quantified. In an infarcted region, extracellular contrast agent passively diffuses into the intercellular space due to myocyte death. This accumulation of contrast agent increases tissue-level contrast. Chronic infarcts are characterized by the absence of living myocytes, which widens interstitial space between collagen fibres. This increases contrast agent concentration that results in hyperenhancement [2]. Figure 1.3 shows an example of a contrast-enhanced MRI in which hyperenhancement is notably present at the anterior region of the myocardium.



Typically, a contrast-enhanced MR acquisition is performed 10–20 minutes after the intravenous introduction of the contrast agent and therefore CE-MRI is often referred to delayed-enhancement or late-enhancement MRI. CE-MRI is effective in identifying the presence, location and extent of acute and chronic myocardial infarction. Transmural extent has become the main metric of infarct assessment in CE-MRI, because there is a strong correlation between infarct transmural extent and the infarct size [19].

Additionally, CE-MRI allows prediction of functional improvement in ischaemia. Viable and non-viable tissue can be distinguished by setting a threshold value on infarct transmural extent. However, it is still an open debate how to define this threshold value; some define a transmural extent of less than 75% as viable [11, 20, 21], while others prefer a more moderate 50% threshold value [22–24].





### 1.1.2 Echocardiography

Echocardiography has gained much popularity for the assessment of ischaemic heart disease because it is a noninvasive low-cost imaging technique that is available in many clinical scenarios. Echocardiographic imaging can also assess tissue viability through different protocols [25, 26], i.e. dobutamine stress echocardiography, tissue doppler imaging and myocardial contrast echocardiography.

Dobutamine stress echocardiography (DSE) assesses the functional response of the heart at stress after the administration of low-dose dobutamine infusion. Viability is noted in DSE by the improvement of ejection fraction from rest to stress, which is directly related to the number of myocardial segments with contractile reserve [27]. Applying DSE in patients with poor acoustic window however is still problematic. DSE suffers from low interobserver and interinstitutional agreement due to different interpretations of stress echocardiograms [28, 29]. Better standardization of visual assessment [30], which can be assisted by an automated method [31], is needed to allow objective evaluation of viable tissue with DSE.

Tissue Doppler imaging (TDI) is a color Doppler imaging technique which analyzes point velocities, accelerations and Doppler signal strength in the myocardium instead of in the blood pool [32]. Several efforts have been made to exploit TDI for viability assessment, but inconsistent prediction of functional recovery from TDI parameters was found [25]. From TDI, strain and strain rate imaging can be derived. Strain rate of scar tissue deteriorates as the extent of infarct transmuralitity increases and this measurement can improve the accuracy of TDI to assess viability [33]. The main drawback of TDI is the continuum of velocity measurements that often produces false abnormal velocity of a normal segment tethered by jeopardized neighboring segments.

Myocardial contrast echocardiography (MCE) is another echocardiographic imaging protocol that measures cellular viability in myocardium. Myocardial necrosis is associated with the loss of microvasculature, which can determine viable and non-viable tissue [34].

### 1.1.3 $^{18}\text{F}$ -fluorodeoxyglucose (FDG) PET imaging

Under normal resting conditions, free fatty acid (FFA) and glucose are two main energy sources of cardiac metabolism. Under ischaemia, oxygen supply decreases which reduces metabolism of FFA. Consequently, exogenous glucose becomes the primary metabolic substrate for myocardium [35]. The increase of glucose uptake by myocardium is therefore an important indicator for ischaemia.

Glucose metabolism in the organ system can be traced by the glucose analog 2-[F-18]-2-deoxy-2-fluoro-D-glucose (FDG) uptake. Myocardial FDG uptake can be imaged by using positron emission tomography (PET). For predicting LV functional improvement after revascularization, FDG-PET has been regarded as the standard of reference for other imaging techniques [36]. However, its limited availability and high costs hamper its application for daily clinical routine.

Cardiac FDG-PET images are relatively low resolution and lack anatomical detail. To provide morphological information, FDG-PET imaging is sometimes combined with other

imaging modalities, such as MR or CT images [37–41]. This approach requires a good registration method to allow an accurate quantitative analysis.

#### 1.1.4 Electrocardiographically-gated perfusion SPECT imaging

Electrocardiographically-gated SPECT (radionuclide perfusion imaging) is a tomographic imaging technique with a radioisotope perfusion tracer. The acquisition is controlled by electrocardiography (ECG) to generate full cardiac cycle of perfusion images [42, 43]. Three perfusion tracers:  $^{99m}\text{Tc}$ -sestamibi,  $^{99m}\text{Tc}$ -tetrofosmin and  $^{201}\text{Tl}$  (Thallium), are routinely used in clinical practice. Standard myocardial perfusion SPECT can be performed at rest or after pharmacologically induced stress. ECG-gated SPECT imaging provides several prognostic values for ischaemic heart disease, including myocardial viability [44, 45] and disease monitoring following a revascularization procedure [46–48].

### 1.2 Computer-assisted diagnosis for ischaemia

The first articles of computerized methods for analyzing medical image data appeared in the 1960s [49, 50], which marked the beginning of CAD development. Initially, a considerable optimism was exalted that a computerized method could provide a complete diagnosis. This expectation gradually abated over time. Instead of assigning the computer the role of a diagnostician, CAD methods have gradually shifted towards computer-generated diagnostic systems to support the physicians' own assessment [51]. A modern CAD method acts as a *second reader* that automatically highlights candidates of a lesion, providing a second opinion to the first reader (radiologist/clinician).

The role of CAD as a second reader has been fostered for the detection of lesion, that are prone to be missed by radiologists alone. That includes the detection of pulmonary nodules in chest radiographic images [52–56], the detection of colorectal polyps from CT colonographic images (virtual colonoscopy) [57–60], and the detection of breast cancer from mammography in breast screening programs [61–63]. A large body of research has been published in these fields, resulting in hundreds of proposed CAD methods with varying results [64, 65]. Common in these results was a substantial increase of sensitivity by the CAD-supported assessment, although the increase varied with the experience of the reader. The advent of CAD has helped radiologists to reduce their reading time [58, 66, 67] and it has also decreased interobserver variability among readers [68, 69].

Also in other areas, several attempts have been made to develop a CAD system to detect lesions or abnormalities. CAD was applied to identify suspected intracranial aneurysms in MR angiographic images [70, 71], to detect pulmonary embolisms [72], to identify arteriolar narrowing in fundus images [73], and mainly other tumor detection applications.

For cardiac applications, a simple computer-aided detection system cannot be applied because of the dynamic nature of the heart. A CAD system for heart disease must be based on what is known as *differential diagnosis* [65], which is based on quantitative differences between two reference points. Currently, CAD for ischaemic heart disease is still in its infancy. Most of the proposed automated methods focused on presenting direct



TABLE 1.1: Comparison of existing automated wall motion assessment methods.

	Method	Regional	Modality	Sample size
Douglass et. al. [90]	LDA	yes	gated SPECT	31
Remme et. al. [91]	SSM	no	cine MRI	13
Bosch et. al. [78]	SSM	yes (limited)	DSE	64
Herz et. al. [92]	PI	yes	3D echo	1 (canine)
Ruiz Dominguez et. al. [93]	PI	yes	echo	10
Caiani et. al. [94]	TV	yes	cine MRI	18
Kachenoura et. al. [95]	PI	yes	cine MRI	13
Lekadir et. al. [88]	SSM	yes	cine MRI	40
Qazi et. al. [96]	LDA	no	echo	—
Leung et. al. [97]	SSM	yes	DSE	129
Mansor et. al. [98]	HMM	yes	DSE	44
Suinesiaputra et. al. [99, 100]	SSM	yes	cine MRI	45

LDA = linear discriminant analysis, SSM = statistical shape model, PI = parametric image, TV = threshold value, HMM = hidden markov model

raw quantification of global or regional LV function to the clinicians [74, 75]. Much effort has been spent on the development of automated quantification of cardiac images, which includes segmentation, registration and cardiac modeling [76, 77].

The first automated classification of wall motion abnormalities (WMA) by using statistical knowledge of myocardial contours was presented by Bosch et. al. [78]. This CAD method utilized a statistical shape model (SSM) of endocardial contours, which was originally used for the segmentation of endocardial borders in echocardiograms [79]. A linear correlation was found between diagnostic predictors (active appearance motion model shape coefficients) with visual wall motion scores.

SSMs provide a morphometric analysis of biological shapes, which are characterized by a set of correspondent anatomical, geometrical or mathematical landmark points [80]. When a set of shapes from the same group is used to build the model, statistical inferences such as the mean shape and the modes of variation will only expose plausible shapes according to that group. The key problem is that the model needs to be specific enough to only generate representative examples. This is the underlying mechanism of Active Shape Models (ASM) [81], an automated segmentation method which has gained popularity for segmenting medical images in general [82, 83], and also for cardiac images [84–86].

SSMs require proper registration of training shapes to eliminate pose related variations (translation, scale and rotation). Post registration, SSMs will contain residual variations that only describe the true inter-subject differences. These variations should be small if all training shapes are taken from the same group, e.g., non pathological subjects. Fitting an SSM onto shapes from outside the model group may produce significantly large variations and errors. This particular feature becomes the main ingredient of characterizing normal and pathological shapes with SSMs [79, 87–89].

Parameterization of left ventricular (LV) motion appears to be a suitable approach to model myocardial contraction for CAD of ischaemia. Aside from SSMs, other CAD

approaches have been proposed to parameterize LV motion. A finite element model was introduced to parameterize wall motion [92]. A Hammer map projection was then applied to map the three-dimensional LV wall into continuous values of ischaemic zones: normal, hypokinesis, akinesis and dyskinesis. Finite element modeling was also combined with SSMs to estimate the deformation of the heart to distinguish normal and patients [91].

Other automated WMA classification methods include outlier detection in SSMs by inter-landmark distances [88], Hidden Markov Models [98], parametric imaging of wall motion [93, 95], linear classifiers [90, 96], and threshold-based LV function indicators [94]. A comparison of existing CAD methods for ischaemic heart disease based on wall motion analysis is given in Table 1.1.

### 1.3 Motivation and objectives

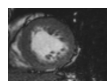
With the increasing prevalence and hospitalization rate of ischaemic heart disease, an explosive growth of diagnostic imaging for ischaemia is ongoing. Clinical decision making on revascularization procedures requires reliable viability assessment to assure long-term patient survival and to elevate cost effectiveness of the therapy and treatment. As such, the demand is increasing for a CAD method for ischaemic heart disease that supports clinicians with an objective analysis of infarct severity, a viability assessment or a prediction of potential functional improvement before performing revascularization.

The goal of this thesis was to explore novel mechanisms that can be used for CAD in ischemic heart disease, particularly through wall motion analysis from cardiac MR images. Existing diagnostic treatment of wall motion analysis from cardiac MR relies on visual wall motion scoring, which suffers from inter- and intra-observer variability. To minimize this variability, the automated method must contain essential knowledge on how the heart contracts normally. This enables quantification of hypokinetic myocardial segments, detection of segments with contractile reserve and prediction of functional improvement in stress. As such, the objectives of this thesis are threefold:

1. To find a proper shape parameterization for myocardial contraction. The dynamic nature of cardiac contraction must be represented in such a way that myocardial shapes from healthy subjects in this representation differ from shapes from ischaemic patients.
2. Define good descriptors and classifiers that are capable of detecting, locating and quantifying regional wall motion abnormalities (RWMA). Hence, locality is a key factor for providing automated segmental analysis of wall motion.
3. Investigate the possibility of applying the automated RWMA method for predicting regional functional improvement from rest to stress MR images.

### 1.4 Outline

This thesis is organized as follows.



**Chapter 1** lays out the background and motivation of this thesis and presents a survey of current imaging techniques and CAD methods for ischaemic heart disease.

**Chapter 2** describes a preliminary investigation on wall motion analysis to extract dense velocity vector fields from tagged MR imaging by using multiscale optic flow. This means velocity vectors from all pixels inside myocardium are automatically calculated over the full cardiac cycle. Quantitative validation is performed by comparing the estimated velocity vector fields with velocity-encoded (VEC) MRI.

**Chapter 3** presents an exploratory study to find a proper shape representation for myocardial contraction. To model the dynamics of myocardial contraction in the static representation of SSMs, shape vectors are defined by serially concatenating endo- and epicardial contours at end-diastole (ED) with endo- and epicardial contours at end-systole (ES). Shapes from both healthy subjects and patients are combined into one SSM. Contractility patterns are extracted by using Principal Component Analysis (PCA) and Independent Component Analysis (ICA), and a comparison between the two decomposition methods is presented. In this chapter, the advantage of ICA to extract local shape features is demonstrated.

**Chapter 4** gives the first application of ICA to detect regional wall motion abnormality (RWMA). Segments with abnormal wall motion are detected by the location of abnormal independent components (ICs) in myocardium. Qualitative evaluation of RWMA on six infarct patients is presented by correlating the position of abnormal ICs with hyperenhanced areas from the corresponding CE-MRI of the same patients.

**Chapter 5:** With the capability of ICA to detect RWMA for ischaemic patients as given in Chapter 4, we explored the method's potential use for predicting regional contractile improvement. Qualitative comparison of RWMA at rest with RWMA at stress is presented in this chapter. By comparing independent component coefficients from rest to stress, the potential to detect myocardial contractile improvement from rest to stress is investigated.

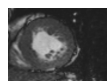
**Chapter 6** represents the core of our CAD method for automated RWMA evaluation. The methodological formulation to estimate RWMA probability density functions is refined and improved by propagating the density functions from the independent component domain to the shape domain. This allows a direct quantification of RWMA at the landmark point level without the need to project a patient shape onto the ICA model. Quantitative validation results from 45 patients with ischaemic heart disease are also presented in this chapter.

**Chapter 7:** investigates of the possibility to automatically detect regional functional improvement when rest and stress cardiac MR data are combined. The statistical model is slightly adapted to accommodate the comparison between rest and stress data during the shapes alignment. A new evaluation of RWMA probability changes from rest to stress is proposed. Correlation with infarct transmuralities from CE-MRI is presented in this chapter.

**Chapter 8** summarizes the CAD development for ischaemic heart disease. Future directions for building a computer-assisted cardiac ischaemia diagnosis method are presented at the end of this chapter.

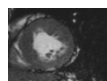
## 1.5 References

- [1] D. Lloyd-Jones, R. Adams, M. Carnethon, G. De Simone, T. B. Ferguson, K. Flegal, E. Ford, K. Furie, A. Go, K. Greenlund, N. Haase, S. Hailpern, M. Ho, V. Howard, B. Kissela, S. Kittner, D. Lackland, L. Lisabeth, A. Marelli, M. McDermott, J. Meigs, D. Mozaffarian, G. Nichol, C. O'Donnell, V. Roger, W. Rosamond, R. Sacco, P. Sorlie, R. Stafford, J. Steinberger, T. Thom, S. Wasserthiel-Smoller, N. Wong, J. Wylie-Rosett, and Y. Hong, "Heart disease and stroke statistics—2009 update: a report from the American Heart Association Statistics Committee and Stroke Statistics Subcommittee," *Circulation*, vol. 119, no. 3, pp. 480–486, Jan 2009.
- [2] H. Mahrholdt, I. Klem, and U. Sechtem, "Cardiovascular MRI for detection of myocardial viability and ischaemia," *Heart*, vol. 93, no. 1, pp. 122–129, 2007.
- [3] T. A. M. Kaandorp, H. J. Lamb, J. J. Bax, E. E. van der Wall, and A. de Roos, "Magnetic resonance imaging of coronary arteries, the ischemic cascade, and myocardial infarction." *Am Heart J*, vol. 149, no. 2, pp. 200–208, Feb 2005.
- [4] G. P. Reddy, S. Pujadas, K. G. Ordovas, and C. B. Higgins, "MR imaging of ischemic heart disease," *Magn Reson Imaging Clin N Am*, vol. 16, no. 2, pp. 201–212, May 2008.
- [5] G. Heusch, R. Schulz, and S. H. Rahimtoola, "Myocardial hibernation: a delicate balance," *Am J Physiol Heart Circ Physiol*, vol. 288, no. 3, pp. H984–99, Mar 2005.
- [6] W. Wijns, S. F. Vatner, and P. G. Camici, "Hibernating myocardium," *N Engl J Med*, vol. 339, no. 3, pp. 173–181, Jul 1998.
- [7] M. Jessup and S. Brozena, "Heart failure," *N Engl J Med*, vol. 348, no. 20, pp. 2007–2018, May 2003.
- [8] S. H. Rahimtoola, V. Dilsizian, C. M. Kramer, T. H. Marwick, and J.-L. J. Vanoverschelde, "Chronic ischemic left ventricular dysfunction: from pathophysiology to imaging and its integration into clinical practice," *JACC Cardiovasc Imaging*, vol. 1, no. 4, pp. 536–555, Jul 2008.
- [9] S. R. Underwood, J. J. Bax, J. vom Dahl, M. Y. Henein, J. Knuuti, A. C. van Rossum, E. R. Schwarz, J.-L. Vanoverschelde, E. E. van der Wall, and W. Wijns, "Imaging techniques for the assessment of myocardial hibernation. Report of a Study Group of the European Society of Cardiology," *Eur Heart J*, vol. 25, no. 10, pp. 815–836, May 2004.
- [10] H. Sakuma, "Magnetic resonance imaging for ischemic heart disease," *J Magn Reson Imaging*, vol. 26, no. 1, pp. 3–13, Jul 2007.
- [11] E. Wellnhofer, A. Olariu, C. Klein, M. Grafe, A. Wahl, E. Fleck, and E. Nagel, "Magnetic resonance low-dose dobutamine test is superior to SCAR quantification for the prediction of functional recovery," *Circulation*, vol. 109, no. 18, pp. 2172–2174, May 2004.
- [12] T. D. Karamitsos, L. E. Hudsmith, J. B. Selvanayagam, S. Neubauer, and J. M. Francis, "Operator induced variability in left ventricular measurements with cardiovascular magnetic resonance is improved after training," *J Cardiovasc Magn Reson*, vol. 9, no. 5, pp. 777–783, 2007.



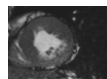
- [13] I. Paetsch, C. Jahnke, V. A. Ferrari, F. E. Rademakers, P. A. Pellikka, W. G. Hundley, D. Poldermans, J. J. Bax, K. Wegscheider, E. Fleck, and E. Nagel, "Determination of interobserver variability for identifying inducible left ventricular wall motion abnormalities during dobutamine stress magnetic resonance imaging," *Eur Heart J*, vol. 27, no. 12, pp. 1459–1464, Jun 2006.
- [14] F. M. Baer, E. Voth, C. A. Schneider, P. Theissen, H. Schicha, and U. Sechtem, "Comparison of low-dose dobutamine-gradient-echo magnetic resonance imaging and positron emission tomography with [18F]fluorodeoxyglucose in patients with chronic coronary artery disease. A functional and morphological approach to the detection of residual myocardial viability," *Circulation*, vol. 91, no. 4, pp. 1006–1015, 1995.
- [15] F. M. Baer, P. Theissen, C. A. Schneider, E. Voth, U. Sechtem, H. Schicha, and E. Erdmann, "Dobutamine magnetic resonance imaging predicts contractile recovery of chronically dysfunctional myocardium after successful revascularization," *J Am Coll Cardiol*, vol. 31, no. 5, pp. 1040–1048, 1998.
- [16] J. H. Cullen, M. A. Horsfield, C. R. Reek, G. R. Cherryman, D. B. Barnett, and N. J. Samani, "A myocardial perfusion reserve index in humans using first-pass contrast-enhanced magnetic resonance imaging," *J Am Coll Cardiol*, vol. 33, no. 5, pp. 1386–1394, Apr 1999.
- [17] W. J. Manning, D. J. Atkinson, W. Grossman, S. Paulin, and R. R. Edelman, "First-pass nuclear magnetic resonance imaging studies using gadolinium-DTPA in patients with coronary artery disease," *J Am Coll Cardiol*, vol. 18, no. 4, pp. 959–965, Oct 1991.
- [18] E. Nagel, C. Klein, I. Paetsch, S. Hettwer, B. Schnackenburg, K. Wegscheider, and E. Fleck, "Magnetic resonance perfusion measurements for the noninvasive detection of coronary artery disease," *Circulation*, vol. 108, no. 4, pp. 432–7, Jul 2003.
- [19] A. Saraste, S. Nekolla, and M. Schwaiger, "Contrast-enhanced magnetic resonance imaging in the assessment of myocardial infarction and viability," *J Nucl Cardiol*, vol. 15, no. 1, pp. 105–117, Jan-Feb 2008.
- [20] J. B. Selvanayagam, A. Kardos, J. M. Francis, F. Wiesmann, S. E. Petersen, D. P. Taggart, and S. Neubauer, "Value of Delayed-Enhancement Cardiovascular Magnetic Resonance Imaging in Predicting Myocardial Viability After Surgical Revascularization," *Circulation*, vol. 110, no. 12, pp. 1535–1541, Sep 2004.
- [21] L. Van Hoe and M. Vanderheyden, "Ischemic cardiomyopathy: value of different MRI techniques for prediction of functional recovery after revascularization," *AJR Am J Roentgenol*, vol. 182, no. 1, pp. 95–100, Jan 2004.
- [22] P. R. Schwartzman, M. B. Srichai, R. A. Grimm, N. A. Obuchowski, D. F. Hammer, P. M. McCarthy, J. M. Kasper, and R. D. White, "Nonstress delayed-enhancement magnetic resonance imaging of the myocardium predicts improvement of function after revascularization for chronic ischemic heart disease with left ventricular dysfunction," *Am Heart J*, vol. 146, no. 3, pp. 535–541, Sep 2003.
- [23] H. P. Kuhl, C. S. A. Lipke, G. A. Krombach, M. Katoh, T. F. Battenberg, B. Nowak, N. Heussen, A. Buecker, and W. M. Schaefer, "Assessment of reversible myocardial dysfunction in chronic ischaemic heart disease: comparison of contrast-enhanced cardiovascular magnetic resonance and a combined positron emission tomography-single photon emission computed tomography imaging protocol," *Eur Heart J*, vol. 27, no. 7, pp. 846–853, Apr 2006.

- [24] M. Gutberlet, M. Frohlich, S. Mehl, H. Amthauer, H. Hausmann, R. Meyer, H. Siniawski, J. Ruf, M. Plotkin, T. Denecke, B. Schnackenburg, R. Hetzer, and R. Felix, "Myocardial viability assessment in patients with highly impaired left ventricular function: Comparison of delayed enhancement, dobutamine stress MRI, end-diastolic wall thickness, and TI201-SPECT with functional recovery after revascularization," *Eur Radiol*, vol. 15, no. 5, pp. 872–880, May 2005.
- [25] D. S. McLean, A. V. Anadiotis, and S. Lerakis, "Role of echocardiography in the assessment of myocardial viability," *Am J Med Sci*, vol. 337, no. 5, pp. 349–354, May 2009.
- [26] S. A. Mollema, G. Nucifora, and J. J. Bax, "Prognostic value of echocardiography after acute myocardial infarction," *Heart*, Mar 2009.
- [27] J. Meluzin, C. G. Cigarroa, M. E. Brickner, J. Cerny, L. Spinarova, M. Frelich, F. Stetka, L. Groch, and P. A. Grayburn, "Dobutamine echocardiography in predicting improvement in global left ventricular systolic function after coronary bypass or angioplasty in patients with healed myocardial infarcts," *Am J Cardiol*, vol. 76, no. 12, pp. 877–880, Nov 1995.
- [28] R. Hoffmann, H. Lethen, T. Marwick, M. Arnese, P. Fioretti, A. Pingitore, E. Picano, T. Buck, R. Erbel, F. A. Flachskampf, and P. Hanrath, "Analysis of interinstitutional observer agreement in interpretation of dobutamine stress echocardiograms," *J Am Coll Cardiol*, vol. 27, no. 2, pp. 330–336, Feb 1996.
- [29] E. Picano, F. Lattanzi, A. Orlandini, C. Marini, and A. L'Abbate, "Stress echocardiography and the human factor: the importance of being expert," *J Am Coll Cardiol*, vol. 17, no. 3, pp. 666–669, Mar 1991.
- [30] R. Hoffmann, H. Lethen, T. Marwick, R. Rambaldi, P. Fioretti, A. Pingitore, E. Picano, T. Buck, R. Erbel, F. A. Flachskampf, and P. Hanrath, "Standardized guidelines for the interpretation of dobutamine echocardiography reduce interinstitutional variance in interpretation," *Am J Cardiol*, vol. 82, no. 12, pp. 1520–1524, Dec 1998.
- [31] A. Nemes, K. Y. E. Leung, G. van Burken, M. van Stralen, J. G. Bosch, O. I. I. Soliman, B. J. Krenning, W. B. Vletter, F. J. ten Cate, and M. L. Geleijnse, "Side-by-side viewing of anatomically aligned left ventricular segments in three-dimensional stress echocardiography," *Echocardiography*, vol. 26, no. 2, pp. 189–195, Feb 2009.
- [32] G. R. Sutherland, M. J. Stewart, K. W. Groundstroem, C. M. Moran, A. Fleming, F. J. Guell-Peris, R. A. Riemersma, L. N. Fenn, K. A. Fox, and W. N. McDicken, "Color Doppler myocardial imaging: a new technique for the assessment of myocardial function," *J Am Soc Echocardiogr*, vol. 7, no. 5, pp. 441–458, Sep-Oct 1994.
- [33] J. Chan, L. Hanekom, C. Wong, R. Leano, G.-Y. Cho, and T. H. Marwick, "Differentiation of subendocardial and transmural infarction using two-dimensional strain rate imaging to assess short-axis and long-axis myocardial function," *J Am Coll Cardiol*, vol. 48, no. 10, pp. 2026–2033, Nov 2006.
- [34] K. Wita, A. Filipecki, A. Drzewiecka-Gerber, M. Turski, A. Rybicka-Musialik, Z. Tabor, M. Nowak, W. Wrobel, J. Krauze, J. Szczogiel, and M. Trusz-Gluzza, "The use of myocardial contrast echocardiography in the assessment of left ventricular function recovery after primary percutaneous coronary intervention in the setting of acute myocardial infarction," *Kardiologia Pol*, vol. 64, no. 7, pp. 713–721, Jul 2006.



- [35] J. J. Bax, F. C. Visser, A. van Lingen, J. H. Cornel, P. M. Fioretti, and E. E. van der Wall, "Metabolic imaging using F18-fluorodeoxyglucose to assess myocardial viability," *Int J Card Imaging*, vol. 13, no. 2, pp. 145–155, Apr 1997.
- [36] V. Dilsizian and R. O. Bonow, "Current diagnostic techniques of assessing myocardial viability in patients with hibernating and stunned myocardium," *Circulation*, vol. 87, no. 1, pp. 1–20, Jan 1993.
- [37] D. W. Townsend, "Dual-modality imaging: combining anatomy and function," *J Nucl Med*, vol. 49, no. 6, pp. 938–955, Jun 2008.
- [38] E. Inglese, L. Leva, R. Matheoud, G. Sacchetti, C. Secco, P. Gandolfo, M. Brambilla, and G. Sambuceti, "Spatial and temporal heterogeneity of regional myocardial uptake in patients without heart disease under fasting conditions on repeated whole-body 18F-FDG PET/CT," *J Nucl Med*, vol. 48, no. 10, pp. 1662–1669, Oct 2007.
- [39] G. Brix, E. A. Nekolla, D. Nosske, and J. Griebel, "Risks and safety aspects related to PET/MR examinations," *Eur J Nucl Med Mol Imaging*, vol. 36 Suppl 1, pp. S131–8, Mar 2009.
- [40] P. Kaufmann, "Cardiac hybrid imaging: state-of-the-art." *Ann Nucl Med*, Apr 2009.
- [41] S. G. Nekolla, A. Martinez-Moeller, and A. Saraste, "PET and MRI in cardiac imaging: from validation studies to integrated applications," *Eur J Nucl Med Mol Imaging*, vol. 36 Suppl 1, pp. S121–30, Mar 2009.
- [42] A. K. Paul and H. A. Nabi, "Gated myocardial perfusion SPECT: basic principles, technical aspects, and clinical applications," *J Nucl Med Technol*, vol. 32, no. 4, pp. 179–187, Dec 2004.
- [43] V. Go, M. R. Bhatt, and R. C. Hendel, "The diagnostic and prognostic value of ECG-gated SPECT myocardial perfusion imaging," *J Nucl Med*, vol. 45, no. 5, pp. 912–921, May 2004.
- [44] A. Maruyama, S. Hasegawa, A. K. Paul, M. Xiuli, J. Yoshioka, K. Maruyama, M. Hori, and T. Nishimura, "Myocardial viability assessment with gated SPECT Tc-99m tetrofosmin % wall thickening: comparison with F-18 FDG-PET," *Ann Nucl Med*, vol. 16, no. 1, pp. 25–32, Feb 2002.
- [45] M. G. Levine, C. C. McGill, A. W. Ahlberg, M. P. White, S. Giri, B. Shareef, D. Waters, and G. V. Heller, "Functional assessment with electrocardiographic gated single-photon emission computed tomography improves the ability of technetium-99m sestamibi myocardial perfusion imaging to predict myocardial viability in patients undergoing revascularization," *Am J Cardiol*, vol. 83, no. 1, pp. 1–5, Jan 1999.
- [46] W. J. Kang, D. S. Lee, J. C. Paeng, K.-B. Kim, J.-K. Chung, and M. C. Lee, "Prognostic value of rest (201)Tl-dipyridamole stress (99m)Tc-sestamibi gated SPECT for predicting patient-based clinical outcomes after bypass surgery in patients with ischemic left ventricular dysfunction," *J Nucl Med*, vol. 44, no. 11, pp. 1735–1740, Nov 2003.
- [47] J. Taki, T. Higuchi, K. Nakajima, I. Matsunari, E.-H. Hwang, H. Bunko, M. Kawasuji, G. Watanabe, and N. Tonami, "Electrocardiographic gated (99m)Tc-MIBI SPECT for functional assessment of patients after coronary artery bypass surgery: comparison of wall thickening and wall motion analysis," *J Nucl Med*, vol. 43, no. 5, pp. 589–595, May 2002.

- [48] S. Hida, T. Chikamori, Y. Usui, H. Yanagisawa, T. Morishima, and A. Yamashina, "Effect of percutaneous coronary angioplasty on myocardial perfusion, function, and wall thickness as assessed by quantitative gated single-photon emission computed tomography," *Am J Cardiol*, vol. 91, no. 5, pp. 591–594, Mar 2003.
- [49] P. H. Meyers, C. M. Nice, Jr, H. C. Becker, W. J. Nettleton, Jr, J. W. Sweeney, and G. R. Meckstroth, "Automated computer analysis of radiographic images," *Radiology*, vol. 83, pp. 1029–34, Dec 1964.
- [50] G. S. Lodwick, A. H. Turner, Jr, L. B. Lusted, and A. W. Templeton, "Computer-aided analysis of radiographic images," *J Chronic Dis*, vol. 19, no. 4, pp. 485–96, Apr 1966.
- [51] R. L. Engle, Jr, "Attempts to use computers as diagnostic aids in medical decision making: a thirty-year experience," *Perspect Biol Med*, vol. 35, no. 2, pp. 207–19, 1992.
- [52] B. van Ginneken, B. M. ter Haar Romeny, and M. A. Viergever, "Computer-aided diagnosis in chest radiography: a survey." *IEEE Trans Med Imaging*, vol. 20, no. 12, pp. 1228–1241, Dec 2001.
- [53] C. S. White, R. Pugatch, T. Koonce, S. W. Rust, and E. Dharaiya, "Lung nodule CAD software as a second reader: a multicenter study," *Acad Radiol*, vol. 15, no. 3, pp. 326–333, Mar 2008.
- [54] J. J. Chen and C. S. White, "Use of CAD to evaluate lung cancer on chest radiography," *J Thorac Imaging*, vol. 23, no. 2, pp. 93–96, May 2008.
- [55] T. Mang, P. Peloschek, C. Plank, A. Maier, A. Graser, M. Weber, C. Herold, L. Bogoni, and W. Schima, "Effect of computer-aided detection as a second reader in multidetector-row CT colonography," *Eur Radiol*, vol. 17, no. 10, pp. 2598–607, Oct 2007.
- [56] B. Sahiner, H.-P. Chan, L. M. Hadjiiski, P. N. Cascade, E. A. Kazerooni, A. R. Chughtai, C. Poopat, T. Song, L. Frank, J. Stojanovska, and A. Attili, "Effect of CAD on radiologists' detection of lung nodules on thoracic CT scans: analysis of an observer performance study by nodule size," *Acad Radiol*, vol. 16, no. 12, pp. 1518–30, Dec 2009.
- [57] S. Halligan, D. G. Altman, S. Mallett, S. A. Taylor, D. Burling, M. Roddie, L. Honeyfield, J. McQuillan, H. Amin, and J. Dehmeshki, "Computed tomographic colonography: assessment of radiologist performance with and without computer-aided detection," *Gastroenterology*, vol. 131, no. 6, pp. 1690–9, Dec 2006.
- [58] N. Petrick, M. Haider, R. M. Summers, S. C. Yeshwant, L. Brown, E. M. Iuliano, A. Louie, J. R. Choi, and P. J. Pickhardt, "CT colonography with computer-aided detection as a second reader: observer performance study," *Radiology*, vol. 246, no. 1, pp. 148–156, Jan 2008.
- [59] M. E. Baker, L. Bogoni, N. A. Obuchowski, C. Dass, R. M. Kendzierski, E. M. Remer, D. M. Einstein, P. Cathier, A. Jerebko, S. Lakare, A. Blum, D. F. Caroline, and M. Macari, "Computer-aided detection of colorectal polyps: can it improve sensitivity of less-experienced readers? preliminary findings," *Radiology*, vol. 245, no. 1, pp. 140–9, Oct 2007.
- [60] L. Bogoni, P. Cathier, M. Dundar, A. Jerebko, S. Lakare, J. Liang, S. Periaswamy, M. E. Baker, and M. Macari, "Computer-aided detection (CAD) for CT colonography: a tool to address a growing need," *Br J Radiol*, vol. 78 Spec No 1, pp. S57–62, 2005.



- [61] D. Georgian-Smith, R. H. Moore, E. Halpern, E. D. Yeh, E. A. Rafferty, H. A. D'Alessandro, M. Staffa, D. A. Hall, K. A. McCarthy, and D. B. Kopans, "Blinded comparison of computer-aided detection with human second reading in screening mammography," *AJR Am J Roentgenol*, vol. 189, no. 5, pp. 1135–1141, Nov 2007.
- [62] N. Karssemeijer, A. M. Bluekens, D. Beijerinck, J. J. Deurenberg, M. Beekman, R. Visser, R. van Engen, A. Bartels-Kortland, and M. J. Broeders, "Breast cancer screening results 5 years after introduction of digital mammography in a population-based screening program," *Radiology*, vol. 253, no. 2, pp. 353–8, Nov 2009.
- [63] J. Tang, R. M. Rangayyan, J. Xu, I. El Naqa, and Y. Yang, "Computer-aided detection and diagnosis of breast cancer with mammography: recent advances," *IEEE Trans Inf Technol Biomed*, vol. 13, no. 2, pp. 236–51, Mar 2009.
- [64] K. Doi, "Computer-aided diagnosis in medical imaging: historical review, current status and future potential," *Comput Med Imaging Graph*, vol. 31, no. 4-5, pp. 198–211, 2007.
- [65] M. L. Giger, H.-P. Chan, and J. Boone, "Anniversary paper: History and status of CAD and quantitative image analysis: the role of Medical Physics and AAPM," *Med Phys*, vol. 35, no. 12, pp. 5799–820, Dec 2008.
- [66] D. Hock, R. Ouhadi, R. Materne, A.-S. Aouchria, I. Mancini, T. Broussaud, P. Magotteaux, and A. Nchimi, "Virtual dissection CT colonography: evaluation of learning curves and reading times with and without computer-aided detection," *Radiology*, vol. 248, no. 3, pp. 860–8, Sep 2008.
- [67] F. Beyer, L. Zierott, E. M. Fallenberg, K. U. Juergens, J. Stoeckel, W. Heindel, and D. Wormanns, "Comparison of sensitivity and reading time for the use of computer-aided detection (cad) of pulmonary nodules at mdct as concurrent or second reader," *Eur Radiol*, vol. 17, no. 11, pp. 2941–7, Nov 2007.
- [68] D. Bielen and G. Kiss, "Computer-aided detection for ct colonography: update 2007," *Abdom Imaging*, vol. 32, no. 5, pp. 571–81, 2007.
- [69] M. Freedman and T. Osicka, "Reader variability: what we can learn from computer-aided detection experiments," *J Am Coll Radiol*, vol. 3, no. 6, pp. 446–55, Jun 2006.
- [70] T. Hirai, Y. Korogi, H. Arimura, S. Katsuragawa, M. Kitajima, M. Yamura, Y. Yamashita, and K. Doi, "Intracranial aneurysms at MR angiography: effect of computer-aided diagnosis on radiologists' detection performance," *Radiology*, vol. 237, no. 2, pp. 605–10, Nov 2005.
- [71] S. Kakeda, Y. Korogi, H. Arimura, T. Hirai, S. Katsuragawa, T. Aoki, and K. Doi, "Diagnostic accuracy and reading time to detect intracranial aneurysms on MR angiography using a computer-aided diagnosis system," *AJR Am J Roentgenol*, vol. 190, no. 2, pp. 459–65, Feb 2008.
- [72] S. Buhmann, P. Herzog, J. Liang, M. Wolf, M. Salganicoff, C. Kirchhoff, M. Reiser, and C. H. Becker, "Clinical evaluation of a computer-aided diagnosis (CAD) prototype for the detection of pulmonary embolism," *Acad Radiol*, vol. 14, no. 6, pp. 651–8, Jun 2007.
- [73] Y. Hatanaka, T. Nakagawa, A. Aoyama, X. Zhou, T. Hara, H. Fujita, M. Kakogawa, Y. Hayashi, Y. Mizukusa, and A. Fujita, "Automated detection algorithm for arteriolar narrowing on fundus images," *Conf Proc IEEE Eng Med Biol Soc*, vol. 1, pp. 286–9, 2005.

- [74] R. J. van der Geest and J. H. Reiber, "Quantification in cardiac MRI," *J Magn Reson Imaging*, vol. 10, no. 5, pp. 602–608, Nov 1999.
- [75] P. Balzer, A. Furber, S. Delepine, F. Rouleau, F. Lethimonnier, O. Morel, A. Tadei, P. Jallet, P. Geslin, and J. J. le Jeune, "Regional assessment of wall curvature and wall stress in left ventricle with magnetic resonance imaging," *Am J Physiol*, vol. 277, no. 3 Pt 2, pp. H901–10, Sep 1999.
- [76] A. F. Frangi, W. J. Niessen, and M. A. Viergever, "Three-dimensional modeling for functional analysis of cardiac images: a review," *IEEE Trans Med Imaging*, vol. 20, no. 1, pp. 2–25, Jan 2001.
- [77] A. A. Young and A. F. Frangi, "Computational cardiac atlases: from patient to population and back," *Exp Physiol*, vol. 94, no. 5, pp. 578–596, May 2009.
- [78] J. G. Bosch, F. Nijland, S. C. Mitchell, B. P. F. Lelieveldt, O. Kamp, J. H. C. Reiber, and M. Sonka, "Computer-aided diagnosis via model-based shape analysis: automated classification of wall motion abnormalities in echocardiograms," *Acad Radiol*, vol. 12, no. 3, pp. 358–367, Mar 2005.
- [79] J. G. Bosch, S. C. Mitchell, B. P. F. Lelieveldt, F. Nijland, O. Kamp, M. Sonka, and J. H. C. Reiber, "Automatic segmentation of echocardiographic sequences by active appearance motion models," *IEEE Trans Med Imaging*, vol. 21, no. 11, pp. 1374–1383, Nov 2002.
- [80] I. L. Dryden and K. V. Mardia, *Statistical Shape Analysis*. John Wiley & Sons, Inc., 1998.
- [81] T. Cootes, D. Cooper, C. Taylor, and J. Graham, "Active Shape Models - their training and application," *Computer Vision and Image Understanding*, vol. 61, no. 1, pp. 38–59, Jan 1995.
- [82] C. J. Taylor, T. F. Cootes, A. Lanitis, G. Edwards, P. Smyth, and A. C. Kotcheff, "Model-based interpretation of complex and variable images," *Philos Trans R Soc Lond B Biol Sci*, vol. 352, no. 1358, pp. 1267–1274, Aug 1997.
- [83] T. F. Cootes and C. J. Taylor, "Anatomical statistical models and their role in feature extraction," *Br J Radiol*, vol. 77 Spec No 2, pp. S133–9, 2004.
- [84] S. C. Mitchell, J. G. Bosch, B. P. F. Lelieveldt, R. J. van der Geest, J. H. C. Reiber, and M. Sonka, "3-D active appearance models: segmentation of cardiac MR and ultrasound images," *IEEE Trans Med Imaging*, vol. 21, no. 9, pp. 1167–1178, Sep 2002.
- [85] H. van Assen, M. Danilouchkine, A. Frangi, S. Ordas, J. Westenberg, J. Reiber, and B. Lelieveldt, "SPASM: A 3D-ASM for segmentation of sparse and arbitrarily oriented cardiac MRI data," *Medical Image Analysis*, vol. 10, no. 2, pp. 286–303, APR 2006.
- [86] A. Andreopoulos and J. K. Tsotsos, "Efficient and generalizable statistical models of shape and appearance for analysis of cardiac MRI," *Med Image Anal*, vol. 12, no. 3, pp. 335–357, Jun 2008.
- [87] S. C. Mitchell, B. P. F. Lelieveldt, H. G. Bosch, J. H. C. Reiber, and M. Sonka, "Disease characterization of active appearance model coefficients," in *Proc. SPIE Medical Imaging 2003, Vol. 5032*, M. Sonka and J. M. Fitzpatrick, Eds., San Diego, USA, May 2003, pp. 38–49.
- [88] K. Lekadir, R. Merrifield, and G.-Z. Yang, "Outlier detection and handling for robust 3-D active shape models search," *IEEE Trans Med Imaging*, vol. 26, no. 2, pp. 212–222, Feb 2007.



- [89] M. Sonka, J. G. Bosch, B. P. Lelieveldt, S. C. Mitchell, and J. H. Reiber, “Computer-aided diagnosis via model-based shape analysis: cardiac MR and Echo,” in *Computer Assisted Radiology and Surgery (CARS) 2003*, ser. International Congress Series, vol. 1256, Jun 2003, pp. 1013–1018.
- [90] K. H. Douglass, J. M. Links, D. C. Chen, D. F. Wong, and H. N. J. Wagner, “Linear discriminant analysis of regional ejection fractions in the diagnosis of coronary artery disease.” *Eur J Nucl Med*, vol. 12, no. 12, pp. 602–604, 1987.
- [91] E. W. Remme, A. A. Young, K. F. Augenstein, B. Cowan, and P. J. Hunter, “Extraction and quantification of left ventricular deformation modes,” *IEEE Trans Biomed Eng*, vol. 51, no. 11, pp. 1923–1931, Nov 2004.
- [92] S. L. Herz, C. M. Ingrassia, S. Homma, K. D. Costa, and J. W. Holmes, “Parameterization of left ventricular wall motion for detection of regional ischemia,” *Annals of Biomedical Engineering*, vol. 33, no. 7, pp. 912–919, Jul 2005.
- [93] C. Ruiz Dominguez, N. Kachenoura, A. De Cesare, A. Delouche, P. Lim, O. Gerard, A. Herment, B. Diebold, and F. Frouin, “Assessment of left ventricular contraction by parametric analysis of main motion (PAMM): theory and application for echocardiography,” *Phys Med Biol*, vol. 50, no. 14, pp. 3277–3296, Jul 2005.
- [94] E. G. Caiani, E. Toledo, P. MacEneaney, D. Bardo, S. Cerutti, R. M. Lang, and V. Mor-Avi, “Automated interpretation of regional left ventricular wall motion from cardiac magnetic resonance images,” *J Cardiovasc Magn Reson*, vol. 8, no. 3, pp. 427–433, 2006.
- [95] N. Kachenoura, A. Redheuil, D. Balvay, C. Ruiz-Dominguez, A. Herment, E. Mousseaux, and F. Frouin, “Evaluation of regional myocardial function using automated wall motion analysis of cine MR images: Contribution of parametric images, contraction times, and radial velocities,” *J Magn Reson Imaging*, vol. 26, no. 4, pp. 1127–1132, Oct 2007.
- [96] M. Qazi, G. Fung, S. Krishnan, J. Bi, R. B. Rao, and A. S. Katz, “Automated heart abnormality detection using sparse linear classifiers,” *IEEE Eng Med Biol Mag*, vol. 26, no. 2, pp. 56–63, Mar-Apr 2007.
- [97] K. Y. E. Leung and J. G. Bosch, “Segmental wall motion classification in echocardiograms using compact shape descriptors,” *Acad Radiol*, vol. 15, no. 11, pp. 1416–1424, Nov 2008.
- [98] S. Mansor, N. P. Hughes, and J. A. Noble, “Wall motion classification of stress echocardiography based on combined rest-and-stress data,” *Med Image Comput Comput Assist Interv Int Conf Med Image Comput Comput Assist Interv*, vol. 11, no. Pt 2, pp. 139–146, 2008.
- [99] A. Suinesiaputra, A. F. Frangi, H. J. Lamb, J. H. C. Reiber, and B. P. F. Lelieveldt, “Automatic prediction of myocardial contractility improvement in stress MRI using shape morphometrics with independent component analysis,” *Inf Process Med Imaging*, vol. 19, pp. 321–332, 2005.
- [100] A. Suinesiaputra, A. F. Frangi, T. A. M. Kaandorp, H. J. Lamb, J. J. Bax, J. H. C. Reiber, and B. P. F. Lelieveldt, “Automated detection of regional wall motion abnormalities based on a statistical model applied to multislice short-axis cardiac MR images,” *IEEE Trans Med Imaging*, vol. 28, no. 4, pp. 595–607, Apr 2009.



# 2

**OPTIC FLOW COMPUTATION FROM CARDIAC MR  
TAGGING USING A MULTISCALE DIFFERENTIAL  
METHOD: A COMPARATIVE STUDY WITH  
VELOCITY-ENCODED MRI**

## Abstract

The computation of an optic flow field to reconstruct a dense velocity field from a sequence of tagged MR images faces a major difficulty: a non-constant pixel intensity. In this chapter, this problem was resolved by regarding the MRI sequence as density images, which adhere to a principle of conservation of intensity. Based on this principle, optic flow equations were developed based on Gaussian derivatives as differential operators. The multiscale optic flow method was applied to cardiac tagged MRI. A quantitative analysis is presented comparing the reconstructed dense velocity field with a directly acquired velocity field using the velocity-encoded (VEC) MRI.

This chapter was adapted from:

A. Suinesiaputra, L. M. J. Florack, J. J. M. Westenberg, B. M. ter Haar Romeny, J. H. C. Reiber, and B. P. F. Lelieveldt. Optic flow computation from cardiac MR tagging using a multiscale differential method: A comparative study with velocity-encoded MRI. In R. E. Ellis and T. M. Peters, editors, *Medical Image Computing and Computer-Assisted Intervention - MICCAI 2003*, volume 2878 of *Lecture Notes in Computer Science*, pages 483–490. Springer, Nov 2003.

There is an optical illusion about every person we meet.

---

Essay II – Experience  
RALPH WALDO EMERSON



**M**OTION analysis is becoming increasingly important in cardiovascular imaging. The cine-MR tagging protocol [1] enables the inspection of myocardial motion, because of temporary tag pattern in the myocardium wall. The tag pattern is induced within a tissue, which will follow the tissue deformation. The tissue motion is clearly visible through the deformed pattern.

Automatic reconstruction of a dense velocity field from tagged MRI is the next step toward a detailed cardiac motion analysis. The velocity field can be computed directly by following the apparent pixel movement, which can be derived using optic flow (OF) methods [2]. A large number of different optic flow methods have been proposed (see [3] for a comparison between various OF methods). However, only a few were proposed for extracting the dense OF field from tagged MRI because of one major problem: the *brightness variation* problem.

In the OF computation, a constant pixel intensity is assumed. This is contained in the formulation that a total derivative of the image function  $L$  is zero.

$$\frac{dL}{dt} = 0 \quad \text{or} \quad \nabla L \cdot \mathbf{v} = 0; \mathbf{v} \in \mathbb{R}^3 \quad (2.1)$$

The MR signal however, linearly depends on the accumulated protons in a certain area. Therefore the tissue deformation causes variation in the pixel intensity due to the divergence of the flow. This chapter presents:

- a new dense optic flow framework, that does not assume a constant pixel intensity, but a constant density. This greatly reduces the sensitivity to brightness variation over time, and therefore enables a more reliable reconstruction of a dense velocity field from tagging MR images, and
- the first direct comparison between reconstructed and directly acquired (using VEC MRI) dense velocity field in clinically representative cases.

The remainder of this chapter is structured as follows. Section 2.1 discusses the proposed approach to the brightness variation problem in tagging MRI and the OF method in detail. In Section 2.2, results from applying the optic flow method to cardiac MR tagging sequences are presented, and statistically compared to the corresponding velocity-encoded (VEC) MR images. Section 4 concludes with a discussion.

## 2.1 Methodology

### 2.1.1 Conservation principle in tagging MRI

Let  $L : \mathbb{R}^3 \rightarrow \mathbb{R}$  be a raw image function and  $\mathcal{L}_{\mathbf{v}}$  be the Lie derivative, a generalization notion of the directional derivative of a function, with respect to a spatiotemporal vector  $\mathbf{v} \in \mathbb{R}^3$ . The optic flow field is defined as a spatiotemporal vector field that satisfies the following constraint

$$\mathcal{L}_{\mathbf{v}} L = 0 \quad (2.2)$$

This is called the *Optic Flow Constraint Equation* (OFCE). It defines the mathematical concept of the optic flow field in a more general formulation than (2.1).

Florack et. al. defined two different kind of pixel flows in an image: scalar and density images [4]. In scalar images, the pixel intensity is assumed to be constant. Horn & Schunck's OF equation [2] deals with these images. In density images, the conserved quantity is not a single pixel value, but the intensity is integrated over a local region. Pixel intensities in the density images may vary, but its total integral is conserved: the local "intensity mass" is preserved.

Tagging MRI is a typical example of density images, because the MR signal is formed by the net magnetization of excited protons [5]. The total number of protons in a tissue is preserved, even if the tissue is deformed. Optic flow analysis of tagging MRI therefore greatly benefits from the derivation of OFCE based on the density conservation principle.

Let  $L_{\rho} : \mathbb{R}^3 \rightarrow \mathbb{R}$  be a raw image function that holds the density images property. The Lie derivative of  $L_{\rho}$  with respect to a vector  $\mathbf{v}$  is defined by taking the derivative of the density function together with the vector field.

$$\mathcal{L}_{\mathbf{v}} L_{\rho} = \sum_{\mu=1}^3 \partial_{\mu} (L_{\rho} \mathbf{v}^{\mu}) = \nabla \cdot (L_{\rho} \mathbf{v}) = 0 \quad (2.3)$$

Equation (2.3) is the OFCE definition for the density images. It has an interesting physical interpretation as the divergence of a vector  $\mathbf{v}$  representing the rate of expansion per unit volume under the flow. Thus it accounts for the change of volume of the local integrated region. In the next sections, unless stated otherwise, we use the notation of  $L$  for the density images.

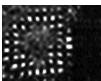
### 2.1.2 The First Order Density Multiscale OFCE

Let  $\mathbf{v}^T = (w(\mathbf{x}), u(\mathbf{x}), v(\mathbf{x}))$ ,  $\mathbf{x} \in \mathbb{R}^3$  be the optic flow vector, which equals the spatiotemporal vector  $\mathbf{v}$  in (2.2), but in a more general form. The function  $w : \mathbb{R}^3 \rightarrow \mathbb{R}_+$  is the temporal component and  $u, v : \mathbb{R}^3 \rightarrow \mathbb{R}$  are the spatial components in  $x$  and  $y$  directions respectively.

As the Lie derivative vanishes in (2.3), its convolution with a Gaussian kernel in the scale-space framework also vanishes. Therefore (2.3) in the Gaussian scale-space framework will be

$$-\int_{\mathbb{R}^3} L (\nabla \phi_{\sigma, \tau} \cdot \mathbf{v}) d\mathbf{x} = 0, \quad \sigma, \tau \in \mathbb{R}_+ \quad (2.4)$$

where  $\phi_{\sigma, \tau}$  is a three dimensional Gaussian kernel with an isotropic spatial scale  $\sigma$  and a temporal scale  $\tau$ .



To eliminate the aperture problem [6], an additional constraint is required. Since the exact cardiac motion is not a-priori known, a perpendicular vector to the tangential vector is applied as the additional constraint: the *normal flow* constraint. If  $\mathbf{v}^T = (u, v)$  is the normal vector, then  $\mathbf{v}_t^T = (0, -v, u)$  is its tangential vector. The vectors  $\mathbf{v}$  and  $\mathbf{v}_t$  can be substituted into (2.4) to get a unique solution.

Another constraint is the *temporal gauge* constraint, which means fixing  $w(\mathbf{x}) \rightarrow 1$ . This states that there are no creation or elimination of pixel intensities. Using (2.4) for the normal and tangential vector and imposing the temporal gauge condition, the first order OFCE can be defined for the density image. It consists of 8 unknowns (the two components of flow vectors and their derivatives with respect to  $x$ ,  $y$  and  $t$ ) in 8 linear equations:

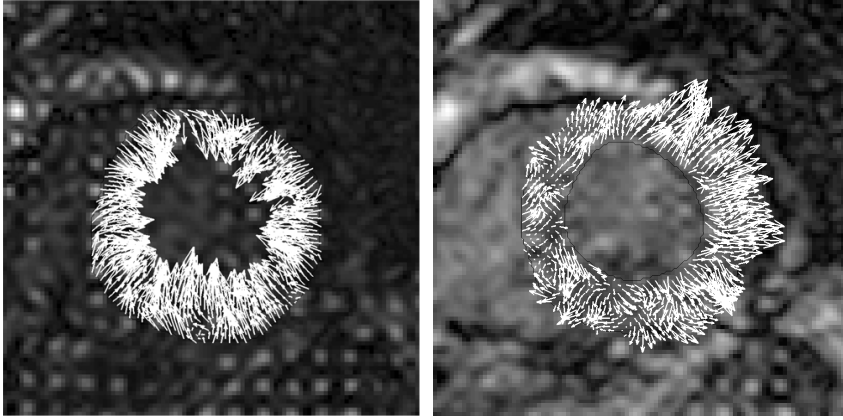
$$\begin{aligned}
 -L_t &= L_x u + L_y v + \tau^2 L_{xt} u_t + \tau^2 L_{yt} v_t + (L + \sigma^2 L_{xx}) u_x + \sigma^2 L_{xy} v_x + \\
 &\quad \sigma^2 L_{xy} u_y + (L + \sigma^2 L_{yy}) v_y \\
 -L_{tt} &= L_{xt} u + L_{yt} v + (L_x + \tau^2 L_{xtt}) u_t + (L_y + \tau^2 L_{ytt}) v_t + (L_t + \sigma^2 L_{xxt}) u_x + \\
 &\quad \sigma^2 L_{xyt} v_x + \sigma^2 L_{xyt} u_y + (L_t + \sigma^2 L_{yyt}) v_y \\
 -L_{xt} &= L_{xx} u + L_{xy} v + \tau^2 L_{xxt} u_t + \tau^2 L_{xyt} v_t + (2L_x + \sigma^2 L_{xxx}) u_x + \\
 &\quad (L_y + \sigma^2 L_{xxy}) v_x + \sigma^2 L_{xxy} u_y + (L_x + \sigma^2 L_{xyy}) v_y \\
 -L_{yt} &= L_{xy} u + L_{yy} v + \tau^2 L_{xyt} u_t + \tau^2 L_{yyt} v_t + (L_y + \sigma^2 L_{xxy}) u_x + \sigma^2 L_{xyy} v_x + \\
 &\quad (L_x + \sigma^2 L_{xyy}) u_y + (2L_y + \sigma^2 L_{yyy}) v_y \\
 0 &= -L_y u + L_x v - \tau^2 L_{yt} u_t + \tau^2 L_{xt} v_t - \sigma^2 L_{xy} u_x + (L + \sigma^2 L_{xx}) v_x - \\
 &\quad (L + \sigma^2 L_{yy}) u_y + \sigma^2 L_{xy} v_y \\
 0 &= L_{yt} u - L_{xt} v + (L_y + \tau^2 L_{ytt}) u_t - (L_x + \tau^2 L_{xtt}) v_t + \sigma^2 L_{xyt} u_x - \\
 &\quad (L_t + \sigma^2 L_{xxt}) v_x + (L_t + \sigma^2 L_{yyt}) u_y - \sigma^2 L_{xyt} v_y \\
 0 &= L_{xy} u - L_{xx} v + \tau^2 L_{xyt} u_t - \tau^2 L_{xxt} v_t + (L_y + \sigma^2 L_{xxy}) u_x - \\
 &\quad (2L_x + \sigma^2 L_{xxx}) v_x + (L_x + \sigma^2 L_{xyy}) u_y - \sigma^2 L_{xxy} v_y \\
 0 &= L_{yy} u - L_{xy} v + \tau^2 L_{yyt} u_t - \tau^2 L_{xyt} v_t + \sigma^2 L_{xyy} u_x - (L_y + \sigma^2 L_{xxy}) v_x + \\
 &\quad (2L_y + \sigma^2 L_{yyy}) u_y - (L_x + \sigma^2 L_{xyy}) v_y
 \end{aligned} \tag{2.5}$$

$L_\mu$  is the image derivative in the Gaussian scale space representation, defined as the convolution of the original image  $L$  (as the initial condition) with the Gaussian derivative kernel  $\phi_{\sigma, \tau}$  in the  $\mu$  dimension [7]. Although there are derivatives of each velocity component in (2.5), this chapter only presents the  $u$  and  $v$  component, as  $x$  and  $y$  velocity component respectively.

### 2.1.3 The multiscale scheme

Two parameters are left undefined in (2.5): the scale parameters  $\sigma$  and  $\tau$ . Although the scale is a free parameter, one proper scale is enough to get a unique solution. Niessen et. al. [8] has studied a scale selection method based on a numerical stability of the solution. The "best result" is defined numerically as the most stable solution of the linear equation system in (2.5). By using the Frobenius norm of the coefficient matrix of (2.5), numerical stable solutions can be estimated.

The next step after solving (2.5) is the *integration of scale space*, which smoothes the output optic flow field [9]. The energy minimization in [9] is modified into the convolution with Gaussian kernels.



(a) Mid-systole dense OF

(b) Mid-diastole dense OF

FIGURE 2.1: One sample comparison result between dense OF from tagging and VEC MRI.

Let  $\tilde{\mathbf{v}}(\mathbf{x}), \mathbf{x} \in \mathbb{R}^3$  be an optic flow vector after the integration and  $\mathbf{v}_{\sigma,\tau}(\mathbf{x})$  be an optic flow vector after the computation of (2.5) with spatial scale  $\sigma$  and temporal scale  $\tau$ . The notion of  $\sigma, \tau$  in the vector  $\mathbf{v}$  is added to incorporate the scale selection scheme. The integration of scale space is given by the following convolution process:

$$\tilde{v}^{\mu}(\mathbf{x}_0) = \int_{\mathbf{x} \in \mathbb{R}^3} p(\mathbf{x}_0) v_{\sigma,\tau}^{\mu}(\mathbf{x}_0) \phi_{\sigma,\tau}(\mathbf{x} - \mathbf{x}_0) d\mathbf{x} \quad (2.6)$$

where  $\mu$  is one of vector's components,  $p(\mathbf{x})$  is a penalty function and  $\phi_{\sigma,\tau}(\mathbf{x})$  is the Gaussian kernel. The penalty function  $p(\mathbf{x})$  in (2.6) is defined as:

$$p(\mathbf{x}) = \exp\left(-\frac{\lambda \kappa(\mathbf{x})}{N_{\kappa}}\right) \quad (2.7)$$

where  $\kappa(\mathbf{x})$  is the Frobenius norm of the coefficient matrix of (2.5) at the spatiotemporal position  $\mathbf{x}$ . The value  $\lambda$  is a constant in the range of (0..1] and  $N_{\kappa}$  is a normalization factor. The value of (2.7) decreases exponentially when  $\kappa$  is large, which means that the more unstable solution contributes less in the final optic flow result.

## 2.2 Experimental results

The multiscale OF method for tagged MRI has been tested and validated on several analytical images and tagging MRI of a phantom agar [10]. In this chapter, the method is applied to real cardiac tagged MR images from a number of cardiac-healthy subjects. The OF method is restricted to estimate only for in-planar motion (2D) in tagging MRI. The results are compared to directly acquired VEC MRI.

TABLE 2.1: Correlation coefficients

Components	Full cycle	Systolic	Diastolic
Radial	$r = 0.86$ ( $SD = 0.04$ )	$r = 0.98$ ( $SD = 0.01$ )	$r = 0.71$ ( $SD = 0.13$ )
Circumferential	$r = 0.42$ ( $SD = 0.17$ )	$r = 0.52$ ( $SD = 0.18$ )	$r = 0.23$ ( $SD = 0.29$ )

## 2.2.1 Clinical Data

Eight healthy volunteers were selected without history of valvular disease, proven from echocardiography. VEC MR images were acquired in a short-axis orientation at a mid-ventricular level. A standard spoiled gradient-echo was applied with velocity-encoding in three directions (maximal velocity sensitivity is 20 cm/s). Retrospective gating with delayed reconstruction was used to cover the full cardiac cycle (30 phases). This acquisition was performed during free breathing.

An MR tissue tagging sequence is used in the same short-axis orientation and position for comparison. Rectangular grid tagging is performed with tag grid spacing = 8.3 mm. Prospective triggering is used with maximum number of heart phases reconstructed, resulting in typical 20-30 phases during one cardiac cycle. This acquisition is performed under breath-holding (in expiration).

Both the VEC and tagging MR images for all patients were acquired in the same study time, with same patient positioning. Due to different breathing conditions, the left ventricular (LV) contours were drawn separately. Contours for tagging images were drawn manually using a dedicated cardiac MR analytical software package (MASS, v5.0, Medis, Leiden, the Netherlands [11]). Contours were drawn in the regular short-axis image, at the closest slice position to the tagging image, because of the better visibility of the myocardial contours in (non-tagged) short-axis slices. Contours for the VEC MRI were drawn manually in the through-plane velocity image, because it gives clearer definition of the myocardial wall than the in-plane velocity images.

In the analysis, time phases of tagging and VEC sequences were normalized into a single cycle. Since the number of phases in tagging images was not equal, MR tagging images were interpolated 30 time frames according to the time steps in the VEC MRI.

## 2.2.2 Results

The region of interest is the LV myocardium. Figure 2.1 and Figure 2.2 shows one sample result of the OF field from a subject compared visually with their corresponding VEC MR images at mid-systole and mid-diastole phases. Only vectors inside the LV myocardium are shown. Notice how the tagging patterns are fading at later phases.

For this comparison between VEC MRI and the computed OF from tagging, only the in-plane motion of the VEC MRI was analyzed. Therefore the z-velocity components were discarded. The comparison is focused at the global LV wall motion, instead of regional wall motion, because the scope of this paper is to investigate how the LV wall motion from optic flow globally relates to VEC MRI.



(a) Mid-systole VEC

(b) Mid-diastole VEC

FIGURE 2.2: One sample comparison result between dense OF from tagging and VEC MRI.

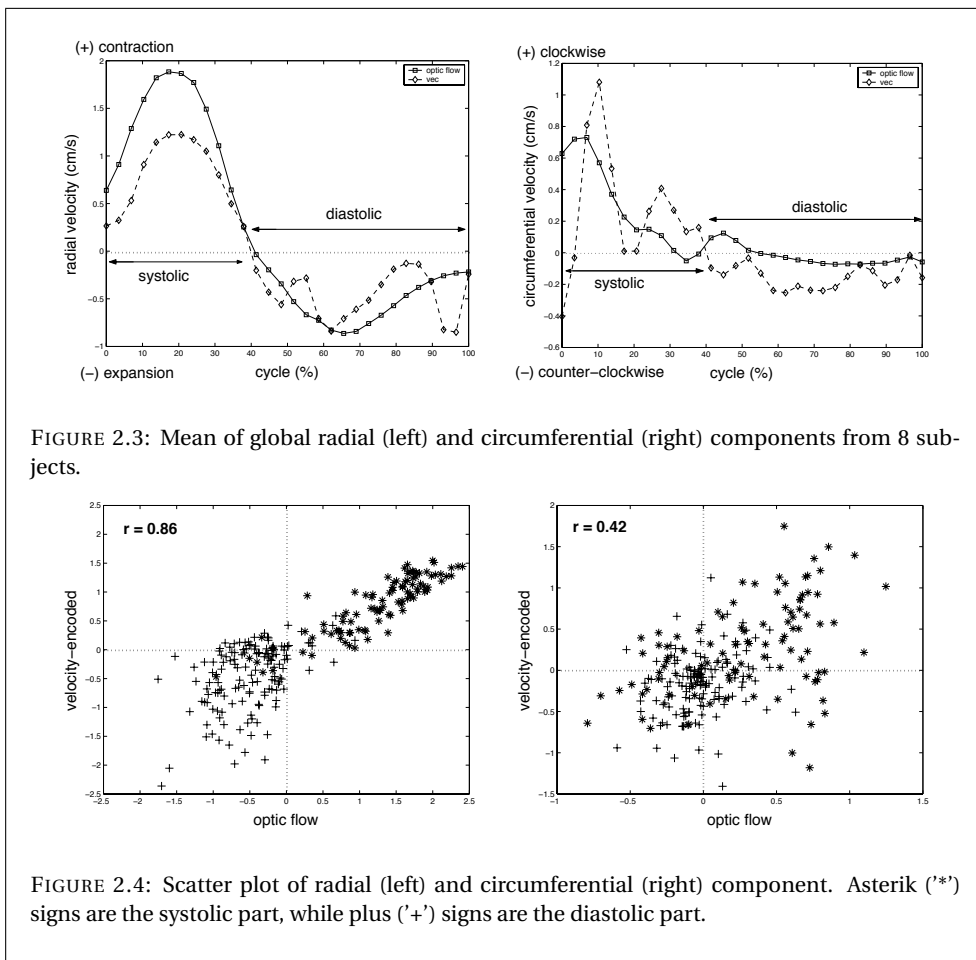
The LV wall undergoes two basic motions, i.e. radial and circumferential components. The radial component defines contraction motion relative to the center of the LV, while the circumferential defines the torsion movement. Figure 2.3 shows the comparison of the mean global radial and circumferential velocity components between the computed OF and VEC MRI.

The correlation coefficient for each components were calculated to investigate the relation between the OF and VEC MRI. As can be seen in Figure 2.4, the OF and the VEC radial velocity has high correlation ( $r = 0.86$ ). This is not the case for the circumferential velocity ( $r = 0.42$ ). Also the radial velocity correlates better at the systolic part of the cycle, while the diastolic half (second half cycle) is less correlated (Table 2.1). In the scatter plot (Figure 2.4), this phenomenon is shown by a cluster of systolic plots (asterisk signs) and diastolic plots (plus signs).

### 2.3 Discussion

The circumferential component correlates less good ( $r = 0.42$ ). This can be explained by two factors. The circumferential movements in the VEC images are more visually apparent than the circumferential movements in the tagging images. This may be caused by the longer trigger delay time of the tagging images, i.e. the rapid torsion at the start of the contraction is not sufficiently covered by the tagging sequence. Therefore the optic flow method is unable to produce the motion that is not sufficiently present in the image data.

Moreover the aperture problem was solved using the normal flow constraint, which reduces all pixel motions to be in the direction of the image gradient. In order to over-



come this limitation, the normal flow constraint should be replaced by a more knowledge-driven motion constraint. If a-priori knowledge of the LV wall motion is integrated, for instance taking into account the torsion movement, then it would be better to replace the normal flow constraint with this knowledge.

The computed dense OF field from tagged MRI shows a very good correlation with the VEC MRI for the LV wall radial contraction. Especially in the systolic part of the cardiac cycle this correlation is stronger ( $r = 0.98$  in systole and  $r = 0.71$  in diastole). In most cases, the cardiac systolic function is clinically more meaningful than the diastolic part. Systolic function gives information of how well the heart can pump the blood to the whole body. Based on this observation, the proposed dense OF method shows a promising non-invasive technique to assess the velocity field during the systolic part of the cardiac cycle.

The proposed method has the flexibility to be extended to 4D by adding one more spa-

tial component in the spatiotemporal vector definition. The optic flow equations would become more complex and more additional constraint equations are needed.

## 2.4 References

- [1] L. Axel and L. Dougherty, "MR imaging of motion with spatial modulation of magnetization," *Radiology*, vol. 171, no. 3, pp. 841–5, Jun 1989.
- [2] B. K. P. Horn and B. G. Schunck, "Determining optical flow," *Artif. Intell.*, vol. 17, no. 1-3, pp. 185–203, 1981.
- [3] S. S. Beauchemin and J. L. Barron, "The computation of optical flow," *ACM Comput. Surv.*, vol. 27, no. 3, pp. 433–467, 1995.
- [4] L. M. J. Florack, W. J. Niessen, and M. Nielsen, "The intrinsic structure of optic flow incorporating measurement duality," *International Journal of Computer Vision*, vol. 27, no. 3, pp. 263–286, 1998.
- [5] W. R. Nitz and P. Reimer, "Contrast mechanisms in MR imaging," *Eur Radiol*, vol. 9, no. 6, pp. 1032–46, 1999.
- [6] D. Marr, *Vision*. San Francisco: W.H. Freeman & Co., 1982.
- [7] T. Lindeberg, *Scale Space Theory in Computer Vision*. Dordrecht: Kluwer Academic, 1994.
- [8] W. Niessen and R. Mass, "Optic flow and stereo," in *Gaussian Scale-Space Theory*, J. Sporring, Ed. Kluwer, 1997, pp. 31–42.
- [9] K. S. Pedersen and M. Nielsen, "Computing optic flow by scale-space integration of normal flow," in *Scale-Space and Morphology in Computer Vision*, ser. Lecture Notes in Computer Science, M. Kerckhove, Ed., vol. 2106. Springer, 2001, pp. 14–25.
- [10] A. Suinesiaputra, "Multiscale optic flow analysis for magnetic resonance tagging," Department of Biomedical Engineering, Technische Universiteit Eindhoven, BMT-Report 2002-01, Jan. 2002.
- [11] R. J. van der Geest, V. G. Buller, E. Jansen, H. J. Lamb, L. H. Baur, E. E. van der Wall, A. de Roos, and J. H. Reiber, "Comparison between manual and semiautomated analysis of left ventricular volume parameters from short-axis MR images," *J Comput Assist Tomogr*, vol. 21, no. 5, pp. 756–65, 1997.

# 3

## **EXTRACTION OF MYOCARDIAL CONTRACTILITY PATTERNS FROM SHORT-AXIS MR IMAGES USING INDEPENDENT COMPONENT ANALYSIS**

## Abstract

Regional wall motion analysis has been used in clinical routine to assess myocardial disease, particularly in ischaemia. This disease can be distinguished from normals by looking at the local abnormality of cardiac motion. In this chapter, the first result of a feature extraction experiment using Independent Component Analysis (ICA) is presented, where abnormal patterns of myocardial contraction from patients are recognizable and distinguishable from normal subjects.

This chapter was adapted from:

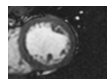
A. Suinesiaputra, A. F. Frangi, M. Üzümcü, J. H. C. R. Reiber, and B. P. F. Lelieveldt. Extraction of myocardial contractility patterns from short-axis MR images using independent component analysis. In M. Sonka, I. A. Kakadiaris, and J. Kybic, editors, *Computer Vision and Mathematical Methods in Medical and Biomedical Image Analysis*, volume 3117 of *Lecture Notes in Computer Science*, pages 75–86. Springer, 2004.

There are things we know that we know. There are known unknowns. That is to say there are things that we now know we don't know. But there are also unknown unknowns. There are things we don't know we don't know.

---

NATO Press Conference, 6 June 2002

DONALD RUMSFELD



**M**YOCARDIAL contractility is an important quantitative indicator for the diagnosis of myocardial diseases. This function can be visually examined and quantified by using a cine MRI sequence. Two most important phases for myocardial contraction are the *end-diastole* (ED), or the start of contraction, and the *end-systole* (ES), or the end of contraction.

Abnormal myocardial contraction is mainly caused by the occlusion of coronary arteries. Coronary artery occlusion causes the imbalance of oxygen supply to the heart which triggers the so-called *ischaemic events* starting from perfusion abnormalities, wall motion abnormalities and finally myocardial infarction. Figure 3.1 shows two examples of MRI images from a healthy volunteer and an infarct patient, both at ES phase. Note that the inferior region (indicated by a white arrow) of the infarct patient does not contract. This region has a small wall thickness value.

To extract myocardial contractility patterns, shape decomposition technique is applied through subspace analysis. Subspace analysis techniques have been used in many areas, including appearance-based modeling and recognition. Principal Component Analysis (PCA) is the common subspace analysis for dimensionality reduction. Independent Component Analysis (ICA) is another subspace analysis, which seeks statistically independent components of the observed data. ICA is commonly used for blind source separation of an observed signal.

In machine learning, both PCA and ICA can be used for feature extraction [1–3]. There exists some literature showing a comparison between both methods with different results. Moghaddam [4] shows no statistical differences between PCA and ICA. Draper et al. [5] compared ICA and PCA for face recognition and reported that some ICA algorithms give better performance than PCA, but some do not.

Regardless of these comparisons, PCA and ICA are both linear generative models, because every training shape can be approximated by a linear combination of the components. An important difference between ICA and PCA lies in the shape variation. Independent components from ICA create local shape variation, while principal components from PCA give a global shape variation [6]. This indicates that ICA is more suitable for extracting local shape features compared to PCA. Local feature extraction is a desirable property specifically in this study.

In this chapter, an ICA-based local feature extraction method for the diagnosis of myocardial disease is presented, especially for myocardial infarction. Section 3.1 describes the myocardial shape model, the ICA method and a new sorting method for ICA modes. Section 3.2 presents experimental results, followed by a discussion in Section 3.3.

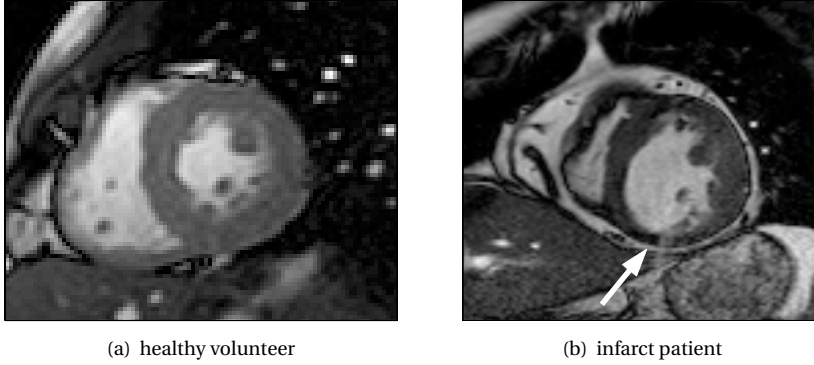


FIGURE 3.1: MRI images of a healthy volunteer and an infarct patient at end-systole (the final contraction phase in the cardiac cycle). White arrow points to the infarcted tissue of the patient, where that myocardial region has a small contraction.

### 3.1 Methodology

#### 3.1.1 ICA model

In this study, the observation data are left ventricular (LV) myocardial contours, manually drawn from short-axis cardiac MR images at ED and ES phases. Samples for each observation are landmark points, defined by equal angular distance along each contour.

To model the contractility pattern between ED and ES, contours for each subject are combined serially into one *shape* vector. A shape  $\mathbf{x} \in \mathbb{R}^{2m}$  is defined by  $m$  landmark points from 4 contours together in the following order: endocardium (inner) contour at ED, epicardium (outer) contour at ED, endocardium contour at ES and epicardium contour at ES. Thus the shape analysis is performed on all concatenated contours together, preserving the aspect ratio between ED and ES. This keeps the contractility patterns among different subjects (shapes).

The shape vector  $\mathbf{x}$  consists of  $m$  pairs of  $(x, y)$  coordinates of landmark points:

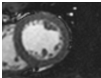
$$\mathbf{x} = (x_1, y_1, x_2, y_2, \dots, x_m, y_m)^T \quad (3.1)$$

The mean shape  $\bar{\mathbf{x}}$  from  $n$  shapes is defined by

$$\bar{\mathbf{x}} = \frac{1}{n} \sum_{i=1}^n \mathbf{x}_i \quad (3.2)$$

Each observed data (shape)  $\mathbf{x}$  can be generated by a linear combination of a component matrix  $\Phi \in \mathbb{R}^{2m \times p}$ . This linear generative model is formulated as follows

$$\mathbf{x} \approx \bar{\mathbf{x}} + \Phi \mathbf{b}, \quad (3.3)$$



where  $\bar{\mathbf{x}}$  is the mean shape and  $\mathbf{b} \in \mathbb{R}^p$  is the component weighting vector.

In ICA, the basis of the subspace is sought to be statistically independent, with the main assumption of the non-gaussian distribution of the observed data [7]. The resulting subspace is non orthogonal and unordered. There is no closed form solution for ICA. Several numerical algorithms to estimate ICA are available (see [8] for the survey of ICA algorithms).

When applied to shape modeling, there is an important property of ICA in its *modes*. As the number of computed independent components increases, the component gives more localized shape variations. On the contrary, if the number of independent components is too small, then the component gives global shape variation, much like PCA modes. A shape variation in ICA has a general shape of a local bump, whereas the remainder of the shape is unaffected (see Figure 3.2(a)). This is the difference between ICA and PCA: PCA modes give global shape variations, distributed over the entire contour (see Figure 3.2(b)). Üzümcü et. al. [6] have presented the comparison between PCA and ICA in the modelling of cardiac shapes.

### 3.1.2 Geometry-based sorting for ICA modes

In subspace analysis, the number of selected components is usually less than the dimension of the observed data. This allows a lower dimensional representation that still covers enough information of the observed data, either for description, detection or recognition.

Principal components are ordered from higher variance to the lowest, making it straightforward to select which and how many components to retain for further analysis; this is however not the case in ICA. There is no natural sorting criteria for independent components. One needs to define a sorting method for independent components that is suitable for a specific application. Since ICA components are local, they can be sorted based on their local position along the contour and this sorting criterion gives a more intuitive interpretation of local shape variations.

Let  $i$ th mode  $\hat{\mathbf{x}}_i$  be defined as the shape variation at the  $i$ th column of  $\Phi$ :

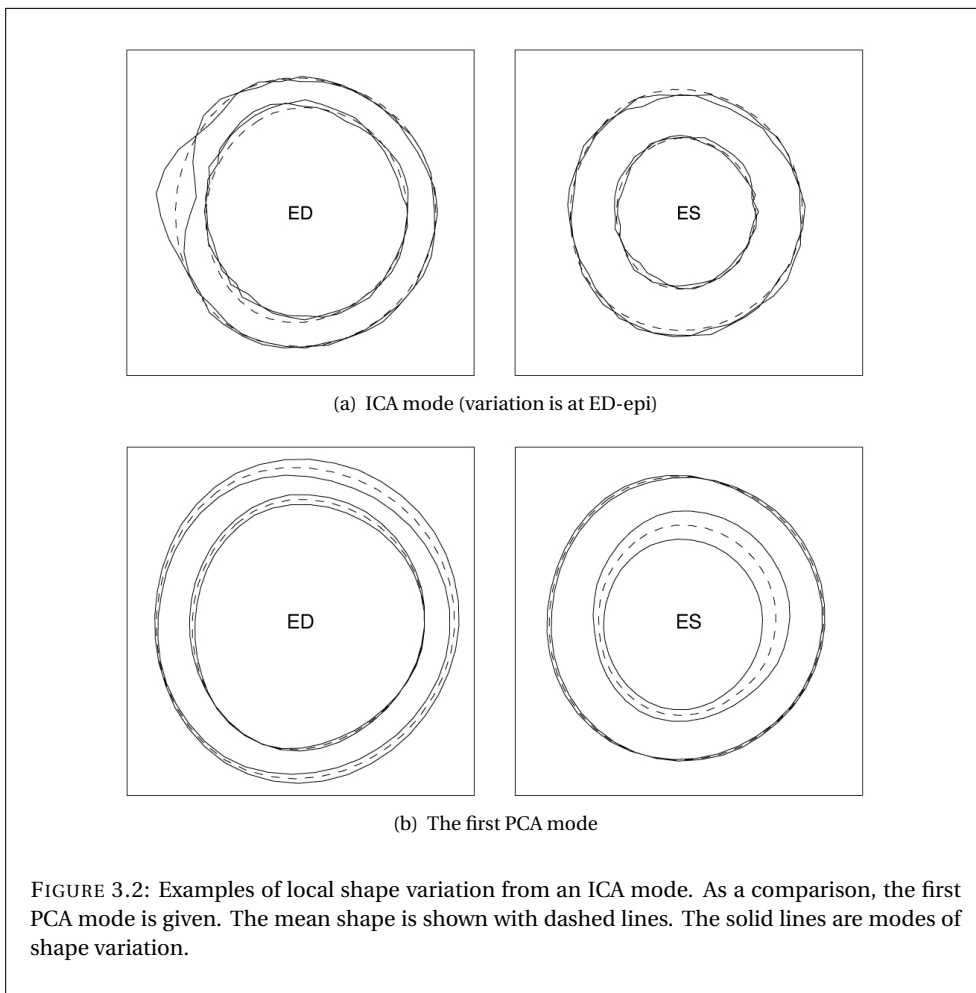
$$\hat{\mathbf{x}}_i = \bar{\mathbf{x}} + \Phi \mathbf{e}_i \quad (3.4)$$

where  $1 \leq i \leq p$  and  $\mathbf{e}_i \in \mathbb{R}^p$  is a vector that has element 1 at the  $i$ th position whereas the rest are 0. Thus,  $\hat{\mathbf{x}}_i$  describes the  $i$ th mode of shape variation.

To locate the position of each  $\hat{\mathbf{x}}_i$  along a contour, a bank of Gaussian filters were applied and then followed by the normalized cross-correlation of each of the filters with a *distance vector* of each mode  $\hat{\mathbf{x}}_i$ . The  $i$ th mode distance vector  $\mathbf{d}_i \in \mathbb{R}_+^m$  is defined as the distance of each landmark point in the shape variation  $\mathbf{x}_i$  to the mean shape. Each element  $j$  of the  $i$ th distance vector is defined by

$$\mathbf{d}_i^{(j)} = \sqrt{\sum_{k=2j-1}^{2j} \left( \hat{\mathbf{x}}_i^{(k)} - \bar{\mathbf{x}}^{(k)} \right)^2}, \quad (3.5)$$

where  $j = 1, 2, \dots, m$ . The cross-correlation is performed only on a particular contour, circularly. Thus there are four cross-correlation processes, because there are four contours for each shape.



The Gaussian filter giving the maximum cross-correlation for vector  $\mathbf{d}_i$  is stored. The center of this filter defines the position of the  $i$ -th component; the width of the Gaussian filter represents the width of the component. Figure 3.3(a) shows an example of the cross-correlation response from a component.

There is an extra advantage of using the normalized cross-correlation for sorting ICA modes. Modes that consist of noise are automatically detected and thus can be eliminated. Noise modes have a global wrinkled shape variation along the whole contour, which correlates best with the widest Gaussian filter. Figure 3.3(b) shows an example of the cross-correlation response for a noise component. After all modes have been cross-correlated, positions of all modes are determined. Subsequently, ICA modes are sorted based on position along the contour.

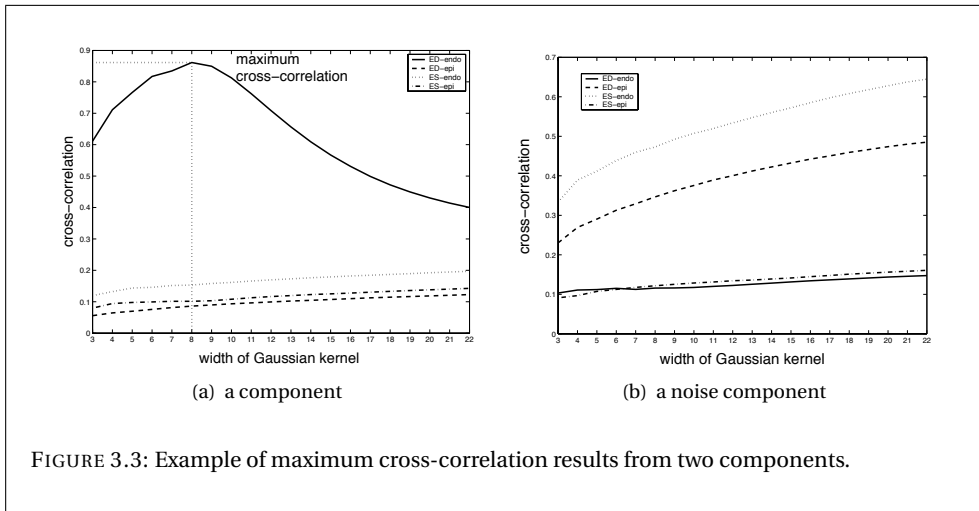
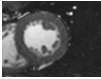


FIGURE 3.3: Example of maximum cross-correlation results from two components.

### 3.1.3 Cluster measurement metrics

To evaluate the cluster formation between normal and patient subjects, a number of  $q$  components ( $q \leq p$ ) are selected from the weighting coefficient matrix  $\mathbf{b}$ .

Let  $\mathcal{D} = \sum_i^c \mathcal{D}_i \subset \mathbb{R}^q$  be a subset of the weighting coefficient matrix  $\mathbf{b}$ , after  $q$  components are selected. Let  $c$  be the number of classes. In this case,  $c = 2$ , because there are only two classes, i.e. normals and patients.

The first measurement is called *within-cluster scatter matrix*, which measures the compactness of a cluster. The within-cluster scatter matrix  $\mathbf{S}_W$  is defined as the sum of scatter matrices for each group:

$$\mathbf{S}_W = \sum_{i=1}^c \sum_{\mathbf{x} \in \mathcal{D}_i} (\mathbf{x} - \mathbf{m}_i)(\mathbf{x} - \mathbf{m}_i)^T, \quad (3.6)$$

where  $\mathbf{m}_i$  is the mean ("center of gravity") of the cluster  $i$ .

A scalar value representing the measurement of the compactness from this metric is simply its trace. The trace of a scatter matrix accounts for the square of the scattering radius, because it is actually the sum of the variances in each coordinate direction. This scalar value is equal to the sum-of-squared error. Thus one seeks the minimum of this value to get the best representation of a cluster. The compactness measurement  $J_W$  can be defined as follows

$$J_W = \text{tr}[\mathbf{S}_W] \quad (3.7)$$

The second measurement is *between-cluster scatter matrix* measurement  $\mathbf{S}_B$ , which represents how far clusters are separated. It is defined as follows

$$\mathbf{S}_B = \sum_{i=1}^c n_i (\mathbf{m}_i - \mathbf{m})(\mathbf{m}_i - \mathbf{m})^T, \quad (3.8)$$

where  $n_i$  is the number of subject of the  $i$ th cluster and  $\mathbf{m}$  is the total mean:

$$\mathbf{m} = \frac{1}{n} \sum_{\mathbf{x} \in \mathcal{D}} \mathbf{x} \quad (3.9)$$

The scalar measurement value of the between-cluster scatter matrix is also its trace:

$$J_B = \text{tr}[\mathbf{S}_B] \quad (3.10)$$

The within-cluster and between-cluster scatter matrices are mostly used to design cluster validity indices for clustering methods [3]. In this study, these measurements are used to compare the quality of the cluster representation given by PCA and ICA components.

To visualize the cluster distribution, the Fisher discriminant line [3] is calculated and coefficient values from the selected components are projected to the Fisher line. Fisher linear discriminant accounts the ratio between the between-cluster and the within-cluster matrix measurements and it is given by:

$$\mathbf{w} = \mathbf{S}_W^{-1} (\mathbf{m}_1 + \mathbf{m}_2), \quad (3.11)$$

where  $\mathbf{w}$  is a vector with the direction that maximizes the separation between the two clusters  $\mathbf{m}_1$  and  $\mathbf{m}_2$ .

## 3.2 Experimental results

Forty-two normal subjects and forty-seven patients suffering from myocardial infarction were investigated. For each subject, endocardial and epicardial contours at ED and ES phases from short-axis view MRI were drawn manually by experts.

All contours were resampled to 40 landmarks defined by equi-angular sampling, starting from the intersection point between the lower right ventricular myocardium with the left ventricular myocardium. The total number of landmark points for each shape were 160 points.

ICA calculation was performed by using the JADE algorithm [9], implemented in Matlab (Matlab v7.0, The Mathworks, Natick, MA, USA). The number of ICA modes was selected carefully to 40 in this study, that gives enough local shape variations for each of the four contours. If the number is too small, then the shape variations become more global. If the number is too large, then too many local shape variations may occur, which look like noise components.

For the ICA mode sorting, 20 Gaussian filters were used, ranging from width 3 to 22. Modes correlating with a Gaussian filter, which has width larger than 20 (half of a contour), were considered to be noise. From the original 40 ICA modes, the sorting method retained 35 modes, thus eliminated 5 noise modes.

### 3.2.1 Weighting coefficient matrix

Figure 3.4(a) shows the weighting matrix  $\mathbf{b}$  of the ICA model that is constructed from shapes of normal subjects and infarct patients. The weighting coefficient matrix contains values that are needed to generate each training shape. These coefficient values

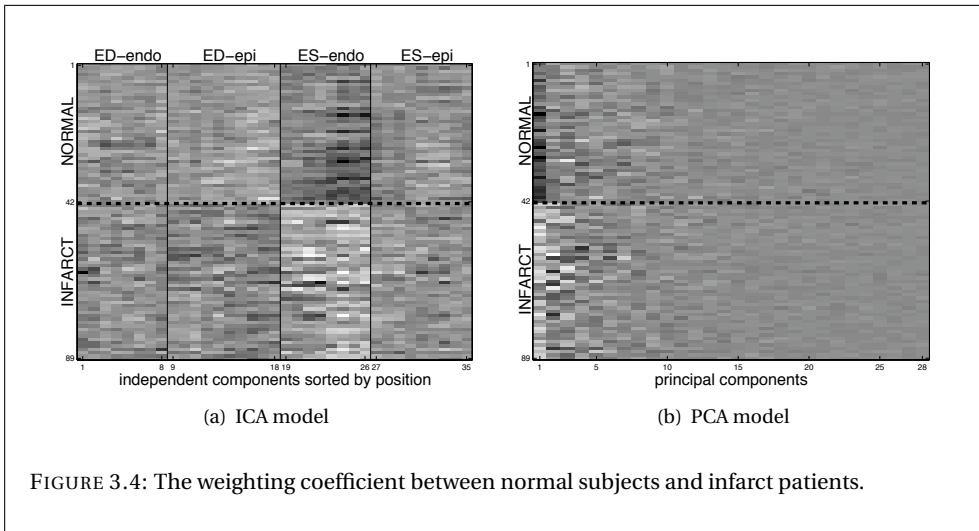
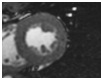


FIGURE 3.4: The weighting coefficient between normal subjects and infarct patients.

are different for each subject. Thus the weighting matrix  $\mathbf{b}$  is the most important value for classification purposes.

From Figure 3.4(a), the boundary between normal and patient subjects is clearly distinguishable in the endocardium at the ES phase. As a comparison, Figure 3.4(b) shows the PCA model from the same data. With PCA, the difference between the two groups is less pronounced. It is clearly visible only from the first component.

### 3.2.2 Mean cluster distance

To enable the comparison between PCA and ICA, the weighting coefficient matrices for both models are normalized, such that  $\|\mathbf{b}\| = 1$ . Hence weighting coefficient matrices for PCA and ICA are both in the same unit.

The distance between means of normal and patient subjects for each component is calculated using the *mean cluster distance* (MCD), as given by:

$$d_i = |m_{n,i} - m_{p,i}|, \tag{3.12}$$

where  $i$  is an index of a component,  $m_{n,i}$  and  $m_{p,i}$  are the mean of the weighting coefficient values at the  $i$ -th component for normal and patient subjects respectively. Figure 3.5 shows the bar plot of the MCD of PCA and ICA for each mode.

A t-test experiment was conducted on each of independent and principal component to see whether the two means from normal and patient coefficient values come from two different clusters. The result is illustrated in Figure 3.5. From 35 selected independent components, there are 27 components with each has statistically significant difference of two means, while PCA only gives 1 component (the first principal component). The t-tests were performed with 95% confidence interval.

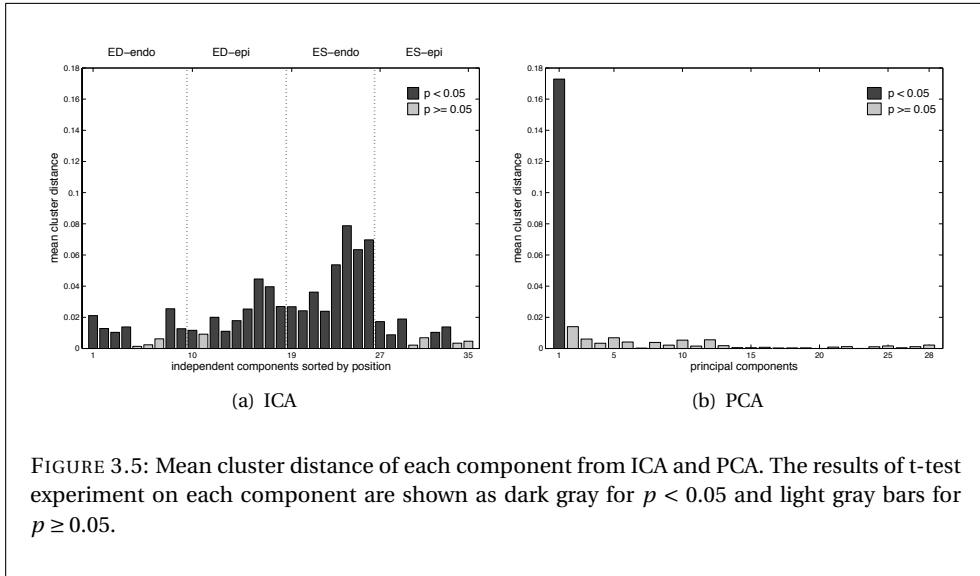


FIGURE 3.5: Mean cluster distance of each component from ICA and PCA. The results of t-test experiment on each component are shown as dark gray for  $p < 0.05$  and light gray bars for  $p \geq 0.05$ .

It is evident that independent components at ES-endo are among the highest MCD value. Mean cluster distance of the first PCA mode is the highest among others, even compared with ICA.

### 3.2.3 Cluster analysis

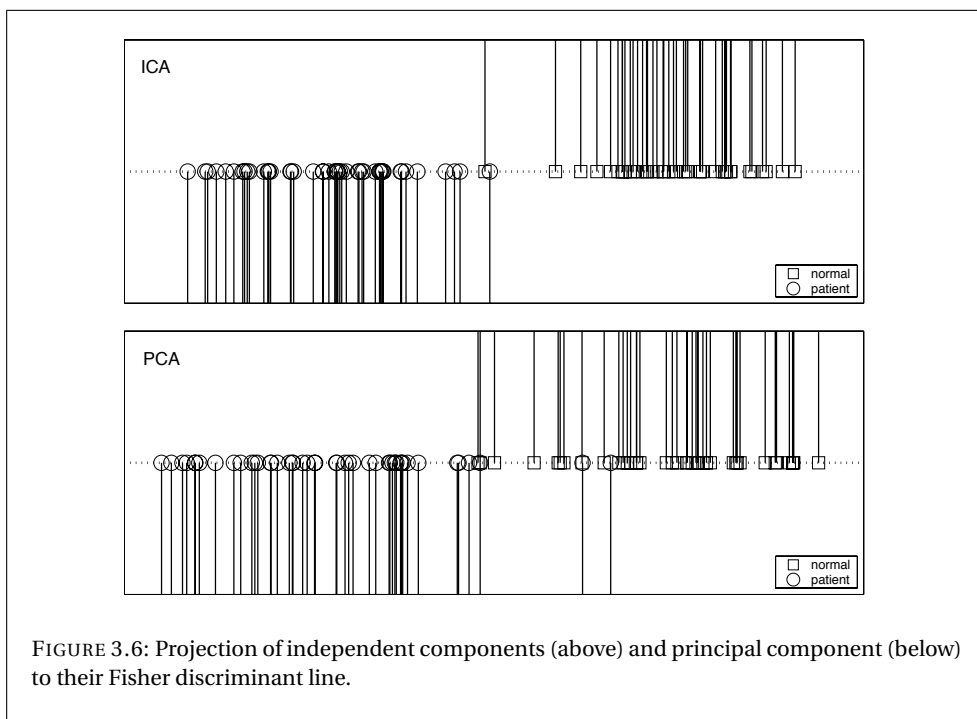
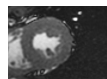
In this study, only an analysis of cluster properties are presented, but **not yet** a classification result. Clusters are defined by selecting all independent components from ICA and principal components that covers 95% of total variance from PCA. This gives 35 ICA components and 16 PCA components.

Table 3.1 shows the measurement results using (3.7) for the cluster compactness and (3.10) for the cluster separation. Figure 3.6 shows result of the projected coefficient values to their Fisher discriminant line.

PCA gives better compactness than ICA, but less separable (see Table 3.1). However the projection to the Fisher discriminant line favors ICA (see Figure 3.6). There is only one point of misclassification in ICA, if a threshold value is defined. However there are more overlaps in the projection of principal components to the Fisher discriminant line.

TABLE 3.1: Cluster validity measurement results.

	compactness ( $J_W$ )	separation ( $J_B$ )
ICA	1.84	0.66
PCA	0.65	0.12

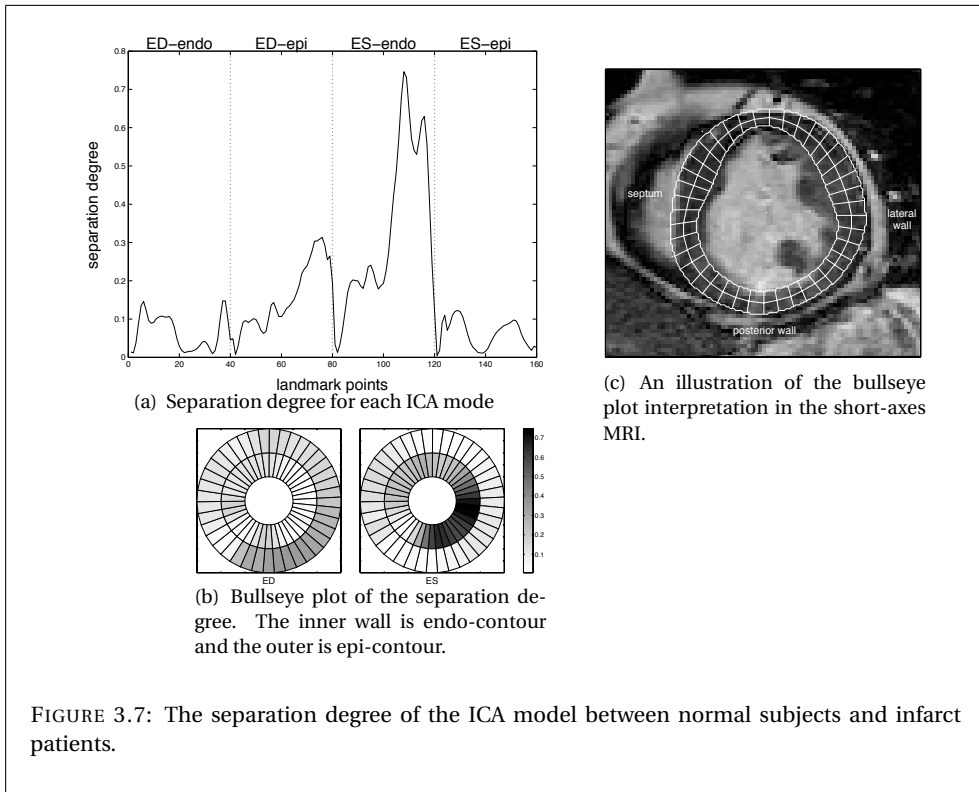


### 3.2.4 Separation degree

The MCD in (3.12) can be used to map the cluster separation for each component onto the same information for each landmark points. This enables a more intuitive regional interpretation of the differences between the two groups.

From the sorting of independent components, location and width of each component are retrieved. Thus the corresponding Gaussian function for each component can be generated and multiply it with its MCD, resulting a Gaussian mixture for each landmark point. The sum of the Gaussian mixture is called *separation degree*. Figure 3.7(a) shows the separation degree of the ICA model from normal and patient subjects. Figure 3.7(b) also shows the same visualization, but a more intuitive way using the bullseye plot, where the color denotes the separation degree.

Figure 3.7(b) corresponds with Figure 3.4(a), where the most important feature to distinguish between normal and patient is the endocardium at ES phase. The least important features lie on the epicardium contour at ES phase, where there is a small separation degree.



### 3.3 Discussion

The potential of ICA in the computer-aided diagnosis of myocardial diseases has been investigated. The first result indicates that the ICA method is a promising analysis tool to extract local shape deformations from observed data. The sorting method of independent components based on their position leads to an anatomically meaningful interpretation for classification purposes. The weighting coefficient matrix from the ICA model can clearly distinguish between the two different groups in the endo-contour at ES.

From the cluster analysis, projection of independent components to the Fisher discriminant line gives better cluster representation than principal components. Given the ability to classify globally and to extract local features, ICA is a powerful tool to detect and to localize shape abnormalities, comparing favorably to PCA.

The experimental results revealed that most of the infarction area affects the endocardium in the infero-lateral wall, because the data contains most patients who have infarction in the lateral and inferior regions. A few patients have infarction in the septum area. From this study, the endocardium at end-systole phase is the most distinguishable feature, because this is the part of myocardium having the most deformation process due to contraction.



The reason why classification was not performed in this experiment is that the problem of classifying a patient versus normal is a toy problem. In clinical routine, it is not interesting to determine a subject as a patient. It is more important to detect if there is an anomaly, to localize it and then to quantify the disease.

The number of computed independent components is a free parameter to choose. The smaller the number is, the more global the independent components are for a shape variation. On the other hand, the shape variation becomes more localized if this parameter is increased. Thus a method to find an optimal number of independent components is needed. An analysis of how sensitive this parameter is to the diagnostic performance in this case will be helpful to define the optimal value.

The next important clinical question for the diagnosis of myocardial infarction is at which particular region of myocardium a patient has an infarction. This basically to localize the local abnormality and to quantify the severity of the disease.

### 3.4 References

- [1] M. S. Bartlett, J. R. Movellan, and T. J. Sejnowski, "Face recognition by Independent Component Analysis," *IEEE Trans. on Neural Networks*, vol. 13, no. 6, pp. 1450–1464, Nov. 2002.
- [2] T.-W. Lee, M. S. Lewicki, and T. J. Sejnowski, "ICA mixture models for unsupervised classification of non-Gaussian classes and automatic context switching in blind signal separation," *IEEE Trans. Pattern Anal. Mach. Intell.*, vol. 22, no. 10, pp. 1078–1089, 2000.
- [3] R. O. Duda, P. E. Hart, and D. G. Stork, *Pattern Classification*, 2nd ed. John Wiley & Sons, Inc., 2001.
- [4] B. Moghaddam, "Principal manifolds and probabilistic subspaces for visual recognition," *IEEE Trans. Pattern Anal. Mach. Intell.*, vol. 24, no. 6, pp. 780–788, 2002.
- [5] B. A. Draper, K. Baek, M. S. Bartlett, and J. R. Beveridge, "Recognizing faces with PCA and ICA," *Computer Vision and Image Understanding*, vol. 91, no. 1-2, pp. 115–137, 2003.
- [6] M. Üzümcü, A. F. Frangi, J. H. Reiber, and B. P. Lelieveldt, "Independent Component Analysis in statistical shape models," in *Proc. of SPIE*, M. Sonka and J. M. Fitzpatrick, Eds., vol. 5032, May 2003, pp. 375–383.
- [7] A. Hyvärinen and E. Oja, "Independent component analysis: algorithms and applications," *Neural Networks*, vol. 13, no. 4-5, pp. 411–430, 2000.
- [8] A. Hyvärinen, "Survey on Independent Component Analysis," *Neural Computing Surveys*, vol. 2, pp. 94–128, 1999.
- [9] J. Cardoso and A. Souloumiac, "Blind beamforming for non Gaussian signals," *IEEE Proceedings-F*, vol. 140, pp. 362–370, 1993.





# 4

## **DETECTING REGIONAL ABNORMAL CARDIAC CONTRACTION IN SHORT-AXIS MR IMAGES USING INDEPENDENT COMPONENT ANALYSIS**

## Abstract

Regional wall motion analysis is used in clinical routine to assess myocardial diseases such as infarction or hypertrophy. Physicians/radiologists can recognize abnormal cardiac motion because they have knowledge about normal heart contraction. This chapter explores the potential of Independent Component Analysis (ICA) to extract local myocardial contractility patterns and to use them for the automatic detection of regional abnormalities. A qualitative evaluation was performed using 42 healthy volunteers to train the ICA model and 6 infarct patients to test the detection and localization. By visual comparison, the experimental results show that automated detection of regional abnormal contraction correlate very well to hyperenhanced areas from delayed-enhancement MR images.

This chapter was adapted from:

A. Suinesiaputra, M. Üzümcü, A. F. Frangi, J. H. C. Reiber, and B. P. F. Lelieveldt. Detecting regional abnormal cardiac contraction in short-axis MR images using independent component analysis. In C. Barillot, D. R. Haynor, and P. Hellier, editors, *Medical Image Computing and Computer-Assisted Intervention – MICCAI 2004*, volume 3216 of *Lecture Notes in Computer Science*, pages 737–744. Springer, Oct 2004.

You know, Donkey, sometimes things are more than they appear.

SHREK (2001)

**I**DENTIFICATION of reversible myocardial ischemic injury is a crucial assessment before coronary revascularization. Myocardial infarction is characterized by the presence of hypokinetic regions. Myocardial infarction can be assessed by using late contrast-enhanced MRI or known also as delayed-enhancement MRI [1].

In the previous chapter, the capability of Independent Component Analysis (ICA) to extract local shape abnormalities was investigated. In this chapter, ICA-based local shape feature detection is applied to automate the detection of abnormal cardiac motion from short-axis MR images. This is achieved by deriving a statistical model of normal heart contraction (*normokinetic model*) and its local contractility patterns. Hence, unlike the previous chapter, the ICA model is trained only from normokinetic heart images.

The objectives of this chapter is summarized as follows:

- A geometry-based sorting method of independent components is proposed, which provides an intuitive anatomical interpretation of the ICA modes.
- The potential of ICA in cardiac shape modeling to detect local contraction abnormalities in infarcted patients is investigated.
- A qualitative evaluation of the detection and localization of myocardial infarctions is presented. Results are visually compared with the corresponding delayed enhancement MRI images.

Section 4.1 describes shape modeling with ICA, the new sorting method for independent components and the method to detect local abnormalities. In Section 4.2, qualitative evaluation results are presented, followed by a discussion in Section 4.3.

## 4.1 Methodology

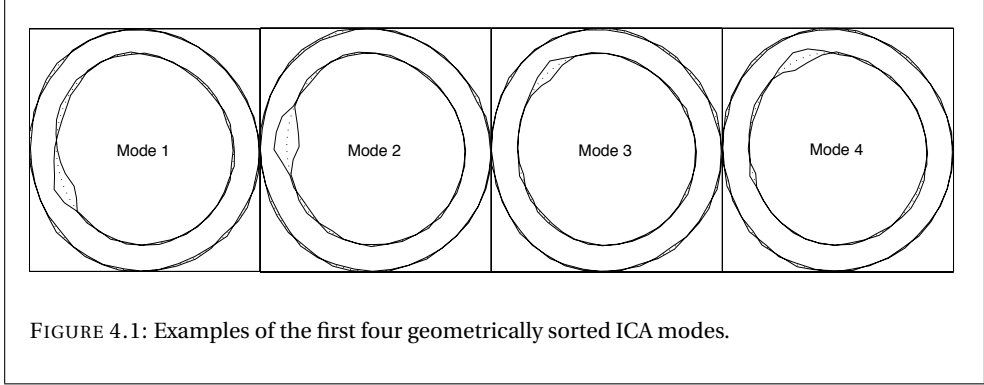
### 4.1.1 ICA modeling of the normal cardiac contraction

ICA is originally used for finding source signals from a mixture of unknown signals without prior knowledge other than the number of sources. In machine learning, ICA has been applied for feature extraction [2] and face recognition [3]. ICA can be applied to statistical shape modeling to extract independent components of the shape variation [4].

ICA is a linear generative model, where every training shape can be approximated by a linear combination of its components. Let  $\mathbf{x} = (x_1, y_1, \dots, x_m, y_m)^T$  be a shape vector, consisting of  $m$  pairs of  $(x, y)$  coordinates of landmark points. The linear generative model is formulated as follows:

$$\mathbf{x} \approx \bar{\mathbf{x}} + \Phi \mathbf{b} . \quad (4.1)$$





The matrix  $\Phi \in \mathbb{R}^{2m \times p}$  defines the independent components (ICs) and  $\mathbf{b} \in \mathbb{R}^p$  is the weight coefficient vector. The mean shape,  $\bar{\mathbf{x}}$ , is defined by

$$\bar{\mathbf{x}} = \frac{1}{n} \sum_{i=1}^n \mathbf{x}_i . \quad (4.2)$$

where  $n$  is the number of shapes and  $p$  is the number of retained components.

The goal of ICA is to find a matrix,  $\Psi$ , such that

$$\mathbf{b} = \Psi (\mathbf{x} - \bar{\mathbf{x}}) \quad (4.3)$$

with a constraint that columns of  $\Psi$  correspond to statistically independent directions. Thus the independent components are given by  $\Phi = \Psi^{-1}$ . The matrix  $\Psi$  is estimated by an optimisation algorithm (see [5] for survey of ICA).

Some pre-processing steps are necessarily performed before the ICA computation. The training shapes must be aligned, such that all shapes are invariant under Euclidean similarity transformations (rotation, translation and scaling). Procrustes analysis [6] is used for the shape alignment. Point correspondence between shapes is usually obtained by taking landmark points with the same anatomical interpretation. The resulting training shapes are zero mean, unit variance and all points are registered between shapes.

In this application, the observed data are left ventricular (LV) myocardial contours from short-axis cardiac MR images at end-diastole (ED) and end-systole (ES) phases. To model the contractility pattern, contours for each subject are combined serially into one shape vector in the following order: endocardium contour at ED, epicardium contour at ED, endocardium contour at ES and epicardium contour at ES.

Figure 4.1 shows examples of ICA derived modes of shape variation sorted geometrically. For comparison, the first mode of shape variation with PCA from the same data is shown in Figure 3.2(b). ICA modes have a general shape of a local "bump", whereas the remainder of the shape is unaffected. This is an important property of ICA, which can be used to detect local shape anomalies. In contrast, PCA modes give global shape variations, distributed over the entire contour. A comparison study of ICA and PCA in cardiac shape modeling is given in [4].



The same geometry-based sorting of independent components described in Chapter 3 is used. Figure 4.1 shows an example of the first four ICA modes after the sorting process. Note that the local shape variations are ordered clockwise.

### 4.1.2 Determining the number of independent components

One important parameter to determine is the number of independent components to estimate during the computation of ICA. Predicting this number with PCA may not always be a good idea, because PCA has a risk to eliminate "weak" ICs in the reduced data [7]. In shape modeling, this parameter affects appearance of the shape variations. As the number of computed ICs increases, the components represent more localized shape variations. If this parameter is too small, then the component gives global shape variation, much like PCA modes.

The determination of the optimal number of computed ICs is task-specific. In this application to detect local abnormalities, we need sufficient regional segments. Too few segments will give an inaccurate localization. More segments will improve the detection resolution, but this is constrained by the computation time and the number of available shapes to avoid overlearning [8]. Figure 4.2 shows the number of segments as a function of the number of computed ICs from 42 shapes of normal hearts.

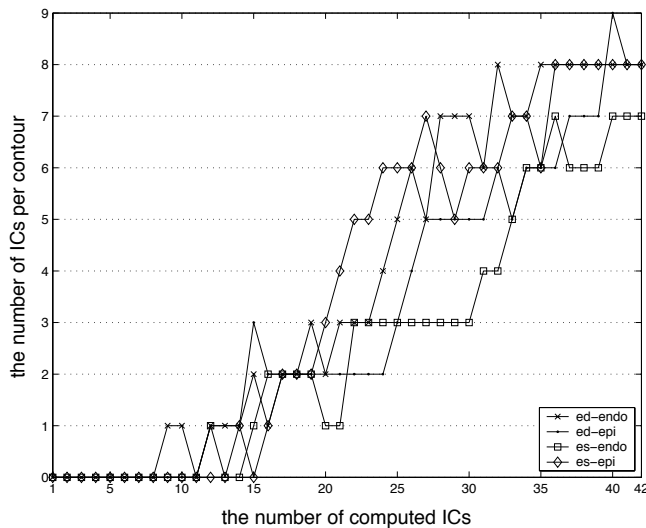


FIGURE 4.2: A plot of the number of ICs per contour as a function of the number of computed ICs. Note that small number of computed ICs produced zero number of ICs per contour because all ICs were detected as noise components, i.e., their shape variation width is larger than the largest Gaussian filter (see Chapter 3).

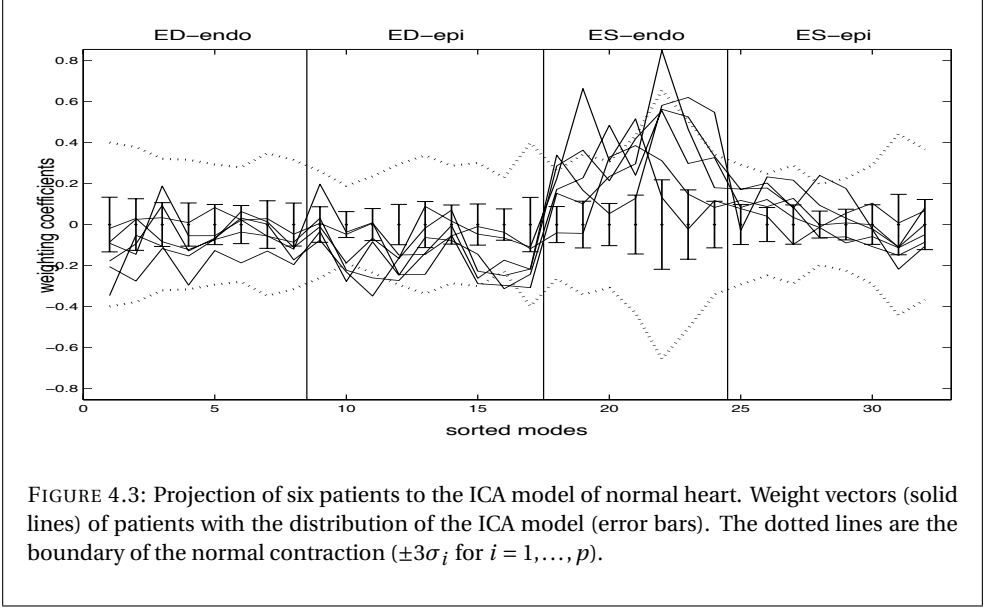


FIGURE 4.3: Projection of six patients to the ICA model of normal heart. Weight vectors (solid lines) of patients with the distribution of the ICA model (error bars). The dotted lines are the boundary of the normal contraction ( $\pm 3\sigma_i$  for  $i = 1, \dots, p$ ).

### 4.1.3 Detection of abnormal contractility patterns

Let  $\mathbf{y} \in \mathbb{R}^{2m}$  be a shape vector, fitted onto the mean shape of the model using the Procrustes fit [6]. The weight vector of the sample  $\mathbf{y}$  is given by

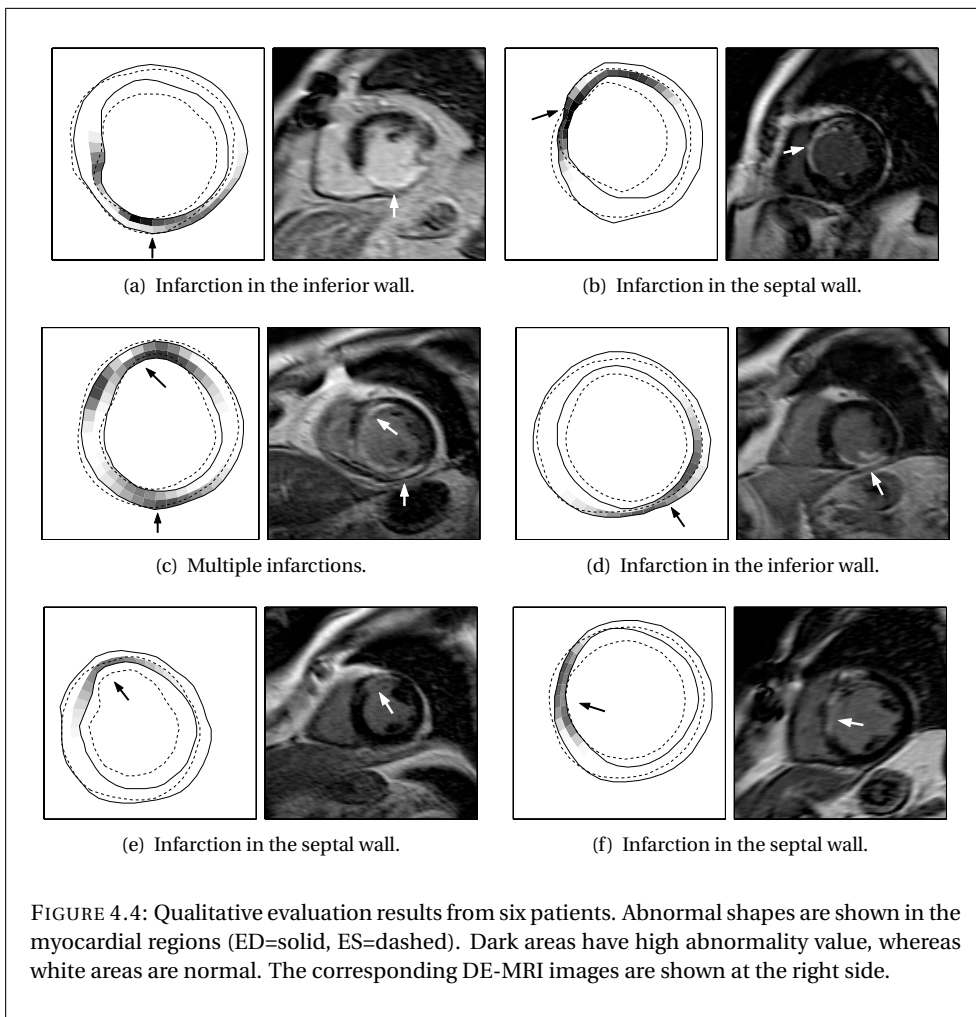
$$\mathbf{b}_y = \Phi^{-1}(\mathbf{y} - \bar{\mathbf{x}}) \quad (4.4)$$

which represents the parameters approximating the patient shape. Patient anomalies are estimated by elements in the weight vector that lie outside the distribution of parameters of the ICA model.

An *anomaly* at the  $i$ -th component  $q_y^{(i)}$  is defined as a value that falls beyond  $\pm 3\sigma_i$  (99.7%), to make sure that the anomaly is an outlier. Thus the *anomaly vector*  $q_y$  is defined by taking the outlier components, normalized by their standard deviation. Each element of  $q_y$  is defined by

$$q_y^{(i)} = \begin{cases} 0 & \text{if } -3\sigma_i \leq b_y^{(i)} \leq 3\sigma_i \\ \frac{b_y^{(i)}}{\sigma_i} & \text{otherwise} \end{cases} \quad \text{for } i = 1, \dots, p \quad (4.5)$$

The anomaly vector (4.5) is mapped to a shape vector to facilitate a more intuitive regional interpretation. From the sorted ICs, the corresponding Gaussian filters giving the maximum responses for each IC are known. These Gaussian filters are generated to model the local bumps, resulting in a mixture of Gaussian functions. The regional sum of the Gaussian mixture gives a shape vector that indicates regional abnormal heart contraction of a patient.



## 4.2 Experimental Results

An ICA model was constructed from 42 healthy volunteers. The mid-ventricular level from short-axis MRI was taken from each subject. Contours were drawn manually and resampled to 40 landmarks defined by equi-angular sampling, starting from the intersection between left and right ventricle. The calculation of ICA was performed using the JADE algorithm [9], implemented in Matlab. The optimal number of computed ICs with minimum of 7 segments per contour is 40 (see Figure 4.2).

To evaluate the infarct detection and localization of the method, MRI data of 6 patients with all necrotic infarcts were investigated. Mid-ventricular short-axis (SA) MRI

images and the corresponding delayed-enhancement (DE) MRI images with the same orientation and the distance only  $< 1$  mm were acquired. Regional abnormal contraction was compared visually with the corresponding DE-MRI. The myocardial infarct regions in the DE-MRI are demonstrated by signal hyperenhancement, corresponding to myocardial necrosis [1].

Six representative evaluation results are presented in Figure 4.4. The anomaly vectors of patients were projected to the corresponding myocardial regions. The contraction patterns are also shown in the plot of ED contours (solid line) and ES contours (dashed line). It is clearly seen from Figure 4.4, that the dark areas have a reduced contraction. The corresponding DE-MRI are given in the right side where the infarction regions are depicted by hyperintensity regions.

### 4.3 Discussion

This chapter shows the potential of ICA as an analysis tool for extracting local shape deformation. Using ICA to train a model of normal cardiac contraction, both global and regional motions are captured. To this end, the method can automatically distinguish between abnormal and healthy cardiac motion.

An intuitive anatomical interpretation of the normal contraction model is achieved by ordering the ICs of the model geometrically along the whole contour. From this, anatomical shape information can be inferred, providing a method to localize the motion abnormalities.

In the qualitative comparison for 6 patients, the hypokinetic regions show an excellent correspondence to the hyperintensity regions of the "gold standard" DE-MRI. This demonstrates that the ICA-based infarct detection and localization from short-axis MRI images is a promising technique for computer aided infarct localization.

### 4.4 References

- [1] R. J. Kim, E. Wu, A. Rafael, E. L. Chen, M. A. Parker, O. Simonetti, F. J. Klocke, R. O. Bonow, and R. M. Judd, "The use of contrast-enhanced magnetic resonance imaging to identify reversible myocardial dysfunction," *N Engl J Med*, vol. 343, no. 20, pp. 1445–53, Nov 2000.
- [2] P. O. Hoyer and A. Hyvärinen, "Independent component analysis applied to feature extraction from colour and stereo images," *Network: Computation in Neural System*, vol. 11, no. 3, pp. 191–210, 2000.
- [3] M. S. Bartlett, J. R. Movellan, and T. J. Sejnowski, "Face recognition by Independent Component Analysis," *IEEE Trans. on Neural Networks*, vol. 13, no. 6, pp. 1450–1464, Nov. 2002.
- [4] M. Üzümcü, A. F. Frangi, J. H. Reiber, and B. P. Lelieveldt, "Independent Component Analysis in statistical shape models," in *Proc. of SPIE*, M. Sonka and J. M. Fitzpatrick, Eds., vol. 5032, May 2003, pp. 375–383.
- [5] A. Hyvärinen, "Survey on independent component analysis," *Neural Computing Surveys*, vol. 2, pp. 94–128, 1999.

- [6] I. L. Dryden and K. V. Mardia, *Statistical Shape Analysis*. John Wiley & Sons, 2002.
- [7] J.-P. Nadal, E. Korutcheva, and F. Aires, "Blind source separation in the presence of weak sources," *Neural Networks*, vol. 13, no. 6, pp. 589–596, 2000.
- [8] A. Hyvärinen, J. Särelä, and R. Vígario, "Bumps and spikes: artifacts generated by independent component analysis with insufficient sample size," in *Proc. Int. Workshop on ICA and BSS*, 1999, pp. 425–249.
- [9] J. Cardoso and A. Souloumiac, "Blind beamforming for non Gaussian signals," *IEEE Proceedings-F*, vol. 140, pp. 362–370, 1993.





A blurred, grayscale MRI scan of a heart, showing the internal structure and the surrounding tissue. The image is out of focus, creating a soft, ethereal background for the text.

# 5

**AUTOMATIC PREDICTION OF MYOCARDIAL  
CONTRACTILITY IMPROVEMENT IN STRESS MRI  
USING SHAPE MORPHOMETRICS WITH  
INDEPENDENT COMPONENT ANALYSIS**

## Abstract

An important assessment in patients with ischaemic heart disease is whether myocardial contractility may improve after treatment. The prediction of myocardial contractility improvement is generally performed under physical or pharmacological stress conditions. In this chapter, a technique to build a statistical model of healthy myocardial contraction using independent component analysis is presented. The model is applied for detecting regions with abnormal contraction in patients both during rest and stress.

This chapter was adapted from:

A. Suinesiaputra, A. F. Frangi, H. J. Lamb, J. H. C. Reiber, and B. P. F. Lelieveldt. Automatic prediction of myocardial contractility improvement in stress MRI using shape morphometrics with independent component analysis. In G. E. Christensen and M. Sonka, editors, *Information Processing in Medical Imaging*, volume 3565 of *Lecture Notes in Computer Science*, pages 321–332. Springer, 2005.

He deals the cards to find the answer.  
The sacred geometry of chance.  
The hidden law of probable outcome.  
The numbers lead a dance.

---

Shape of My Heart  
STING

**I**SCHAEMIC heart disease is a major heart disease in the western world. Non-invasive diagnosis of ischaemia has been developed in recent years (see [1] for the survey of different imaging techniques). Among others, Magnetic Resonance Imaging (MRI) has attracted many clinicians due to its excellent spatial and temporal resolution, high-contrast of soft tissue, accurate and reproducible global and regional ventricular functions, flow and perfusion during rest and pharmacological stress, and the possibility of using paramagnetic contrast agent to enhance the intensity of myocardial infarction areas [2, 3].

One crucial assessment in ischaemic heart disease is to determine the presence of hibernating myocardium. This is a viable but dysfunctional myocardium, which may improve its function after treatment [1]. The prediction of improvement of myocardial contraction is only possible during physical or pharmacological stress [4]. Thus, the identification of dysfunctional myocardium that improves under stress is an important factor in the treatment of ischaemic heart disease.

Low-dose dobutamine stress MRI can be used to evaluate improvement of myocardial contraction in ischaemic patients [1, 5]. In this procedure, a low dose of dobutamine is administered prior to MR acquisition to produce stress images. Usually, visual comparison between the rest and stress cine images is performed for visual wall motion scoring. However, this visual assessment is very difficult and subjective, because differences between rest and stress motion may be very subtle.

The goal of this work is to develop a method to automatically detect subtle changes in cardiac contraction between rest and stress. In this chapter, further expansion of previously described work (see Chapter 4) on modeling the myocardial contraction of healthy hearts is presented [6]. A statistical contraction model is trained from myocardial contours in rest condition using Independent Component Analysis (ICA) to construct a set of locally selective basis functions. Analysis is performed by projecting patient shapes onto this basis, and in Chapter 4, this model is used to automatically detect and localize abnormal cardiac contraction in rest. The main improvements of this chapter are twofold:

- The ICA modeling framework is improved by adopting a principled way of selecting the optimal number of components, and introducing kernel density estimation to describe the model parameter distributions for normal contraction.
- The rest-stress comparison framework is introduced. By comparing the projection parameters in rest and stress conditions, one can assess which regions of myocardium show contractility improvement under stress, and therefore may be viable.



This chapter is organized as follows. Section 5.1 describes the statistical modeling of normal contraction by using ICA. In Section 5.2, we present the qualitative prediction results of myocardial viability in stress condition, followed by a discussion in Section 5.3.

## 5.1 Methodology

ICA is originally used for finding source signals from a mixture of unknown signals without prior knowledge other than the number of sources [7]. There have been some studies to use ICA in machine learning for feature extraction [8], face recognition [9] and classification [10]. Previously, a statistical model to detect regional abnormalities from infarct patients using ICA has been reported [6]. The advantage of using ICA over other decompositions is the fact that ICA yields locally independent detectors that can be used to determine regional shape abnormalities, whereas PCA yields global shape variations that influence the entire shape.

ICA is a linear generative model, where every training shape can be approximated by a linear combination of its components. Let  $\mathbf{x} = (x_1, y_1, \dots, x_m, y_m)^T$  be a shape vector, consisting of  $m$  pairs of  $(x, y)$  coordinates of landmark points. The linear generative model is formulated as follows:

$$\mathbf{x} \approx \bar{\mathbf{x}} + \Phi \mathbf{b} . \quad (5.1)$$

The matrix  $\Phi \in \mathbb{R}^{2m \times p}$  defines the independent components (ICs) and  $\mathbf{b} \in \mathbb{R}^p$  is the weight coefficient vector. The mean shape,  $\bar{\mathbf{x}}$ , is defined by

$$\bar{\mathbf{x}} = \frac{1}{n} \sum_{i=1}^n \mathbf{x}_i . \quad (5.2)$$

where  $n$  is the number of shapes and  $p$  is the number of retained components.

The goal of ICA is to find a matrix,  $\Psi$ , such that

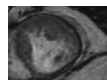
$$\mathbf{b} = \Psi (\mathbf{x} - \bar{\mathbf{x}}) \quad (5.3)$$

with a constraint that columns of  $\Psi$  correspond to statistically independent directions. Thus the independent components are given by  $\Phi = \Psi^{-1}$ . The matrix  $\Psi$  is estimated by a suitable optimisation algorithm (see [11] for survey of ICA).

### 5.1.1 Modeling contraction of healthy myocardium

The observed shapes are taken from LV epi- and endocardial contours from short-axis MR images. To model the contractility pattern, contours for each subject are combined serially into one shape vector in the following order: endocardial contour at *end-diastole* (ED), epicardial contour at ED, endocardial contour at *end-systole* (ES) and epicardial contour at ES.

Prior to shape modeling, Procrustes shape alignment on the four contours at once was performed as a pre-processing step to eliminate global shape differences in pose and scale between the samples [12]. Mean shape of the training shapes after the alignment is shown in Figure 5.1.



Since the improvement of motion contraction from rest to stress is the main issue, *centerline* points, i.e. points in the the middle between epi- and endocardial contours, were used in ICA. The centerline method has already been used in a rest and stress study to diagnose coronary artery disease [13]. Figure 5.1(c) shows the centerline points from the mean shape.

Four examples of independent components from the centerline model are shown in Figure 5.2. The independent components (ICs) show an interesting and important property where shape variations are local. In the diagnosis, these shape variations are used as detectors to determine local shape abnormalities, i.e. regions with abnormal contraction.

### 5.1.2 Optimal number of independent components

If the number of source signals in ICA is not known a priori, the number of components needs to be determined. Many methods have been proposed to estimate this parameter, for instance, by using mutual information [14], neural networks [15], a Bayesian approach [16], and clustering techniques [17]. Though these approaches are different, the basic idea is to determine which are "weak" and "strong" independent components. Strong ICs represents reliable components.

For this study, the clustering technique proposed by Himberg et. al. [17]<sup>1</sup> is adopted. This approach selects reliable ICs from a number of different realizations of ICs with different initializations. The selection is performed by clustering the resulting ICs. This approach was selected because of stochastic nature of computing ICs with the FastICA [7], the most popular and robust ICA algorithm that we used in this study.

After each trial, each IC is represented as a single point in a source space. The reliability of the estimated ICs can be analyzed by looking at the spread of the obtained ICs. The ICs form clusters in the source space, and the more compact and isolated the cluster of an IC, the more reliable is the IC (see Figure 5.3(b)). To measure the reliability of a cluster,

<sup>1</sup>The implementation is known as the *Icasso* package [17].

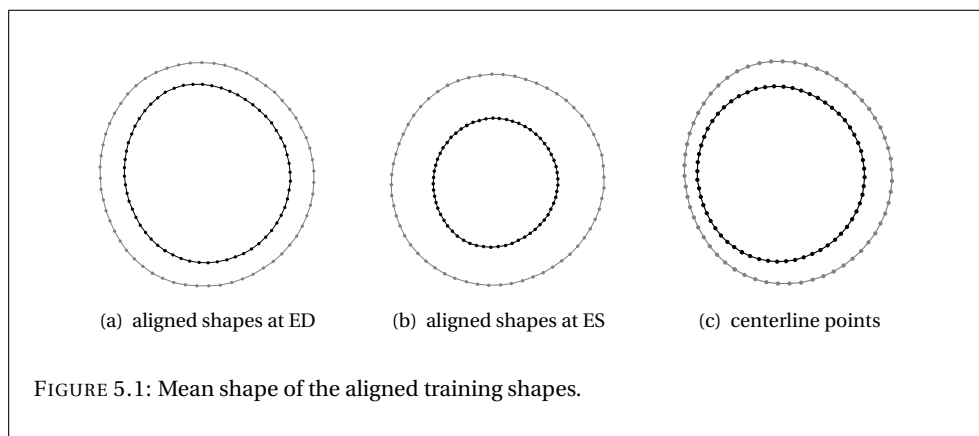
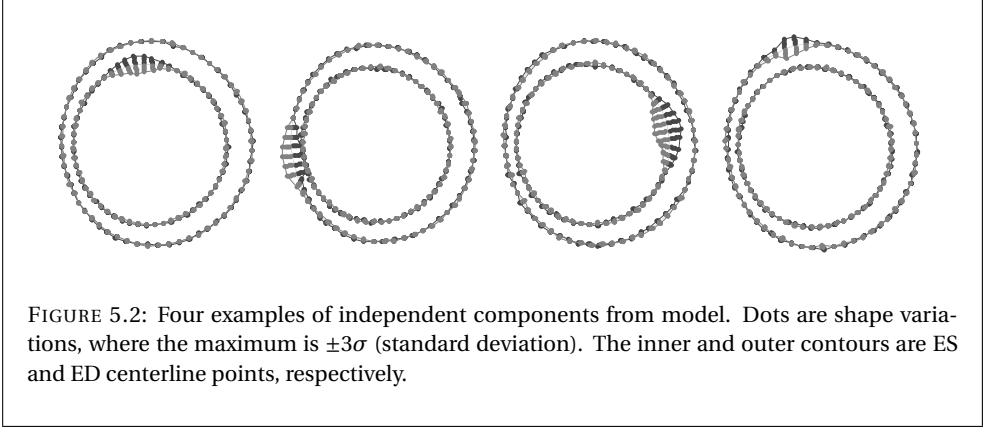


FIGURE 5.1: Mean shape of the aligned training shapes.



an agglomerative hierarchical clustering is performed. A quality index of an IC,  $I_q$ , that reflects the compactness and isolating of a cluster, is defined as

$$I_q(C_m) = \frac{1}{|C_m|^2} \sum_{i,j \in C_m} \sigma_{ij} - \frac{1}{|C_m||C_{-m}|} \sum_{i \in C_m} \sum_{j \in C_{-m}} \sigma_{ij} \quad (5.4)$$

where  $C_m$  and  $C_{-m}$  are the set of indices that belong and do not belong to the  $m$ -cluster, respectively. The  $\sigma_{ij}$  is a similarity measurement between  $i$ -th and  $j$ -th IC using their mutual correlation coefficient  $r_{ij}$ , i.e.

$$\sigma_{ij} = |r_{ij}|. \quad (5.5)$$

The value of  $I_q$  increases when  $C_m$  becomes more compact and isolated.

Another measurement to indicate reliable ICs in the clustering technique is the R-index,  $I_R$

$$I_R = \frac{1}{L} \sum_{m=1}^L \frac{S_m^{\text{in}}}{S_m^{\text{ex}}} \quad (5.6)$$

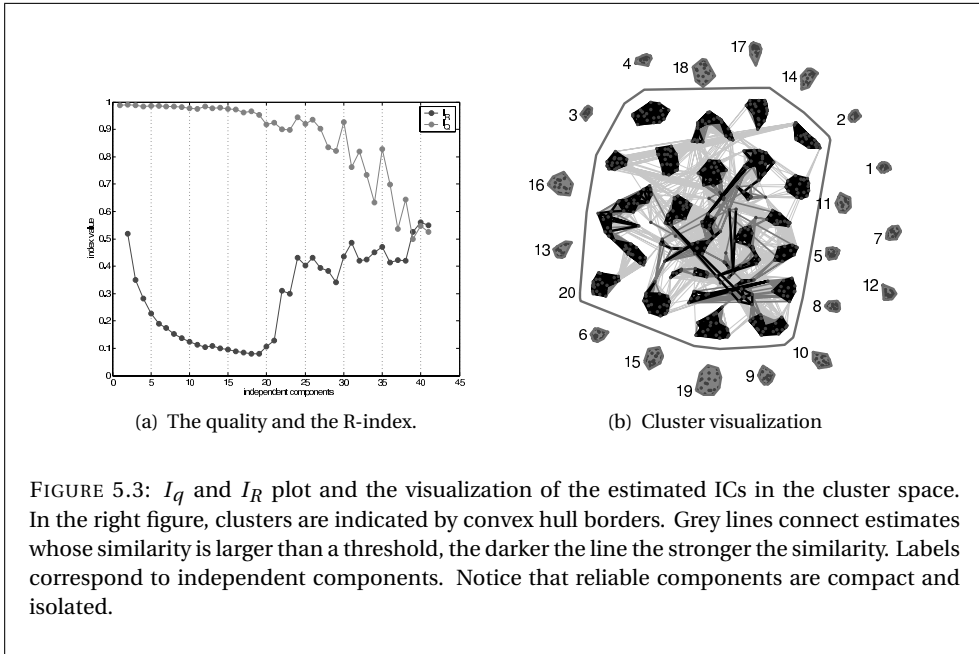
where

$$S_m^{\text{in}} = \frac{1}{|C_m|^2} \sum_{i,j \in C_m} d_{ij}$$

$$S_m^{\text{ex}} = \min_{m' \neq m} \frac{1}{|C_m||C_{m'}|} \sum_{i \in C_m} \sum_{j \in C_{m'}} d_{ij} .$$

$d_{ij}$  is a dissimilarity measurement, defined as  $d_{ij} = 1 - \sigma_{ij}$ . The R-index is basically a ratio between the *within-cluster* and *between-cluster* ratio.

The R-index and the quality index indicate improved clustering in opposite directions. The optimal value for the number of computed ICs is when  $I_q$  is large and  $I_R$  is small. The plot of  $I_q$  and  $I_R$  for our study is shown in Figure 5.3(a).



The visualization of IC clusters is shown in Figure 5.3(b). Each estimated IC is represented as a single point in the cluster space. Reliable ICs form compact and isolated clusters. In Figure 5.3(b), ICs number 1 until 19 are reliable, whereas the remaining ICs are not reliable (they are glued together as one cluster number 20). The gray lines in Figure 5.3(b) denote dependencies at some threshold values between clusters.

### 5.1.3 Density estimation of coefficient values from the ICA model

In (5.1), the  $\mathbf{b}$  vector represents the projection of a shape  $\mathbf{X}$  onto the IC basis  $\Phi$ . The  $\mathbf{b}$  vector contains coefficient values for the model that are needed to approximate the shape  $\mathbf{X}$  from the IC basis. If the shape of  $\mathbf{X}$  is similar to the shapes that construct the IC basis, then the coefficient values are within the distribution of the  $\mathbf{b}$  vector of the model. On the contrary, the coefficient values are outside of the distribution. Hence, the detection of abnormal shapes becomes a problem of estimating the probability density function of the model coefficient values.

Since the ICA model is built from  $n$  training shapes, (5.1) can be simply reformulated in matrix form as:

$$\mathbf{X} = \bar{\mathbf{x}} \cdot \mathbf{1}^T + \Phi \mathbf{B} . \quad (5.7)$$

The probability density function is estimated from of each column in matrix  $\mathbf{B}$ . Figure 5.4 shows the distribution of each coefficient value from the healthy heart contraction for each IC (column of  $\mathbf{B}$ ), with an example of a projected patient shape.

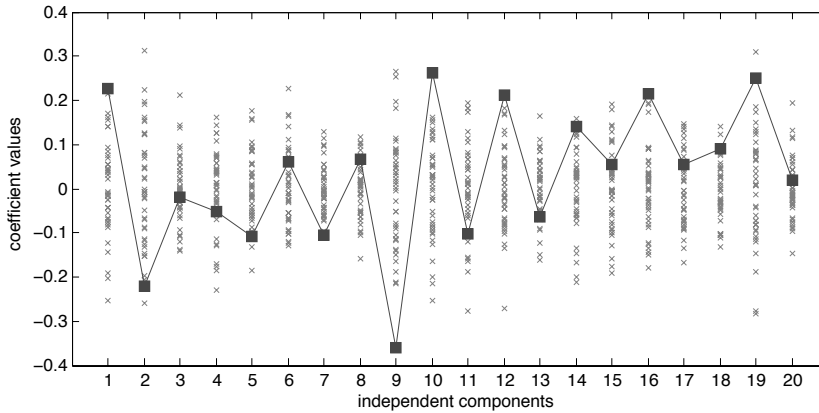


FIGURE 5.4: Distribution of coefficient values of healthy heart contraction (crosses) with an example of coefficient values from the projected shape of a patient (solid lines).

In ICA, components are sought to be statistically independent. This is achieved by finding the direction of components that maximizes the nongaussianity. The result is an independent basis which is non-orthogonal. The components have non-gaussian distribution, or at most only one with a gaussian distribution [7]. By statistical independency assumption, the multivariate density estimation of the matrix  $\mathbf{B}$  can be simplified into univariate density estimation. Therefore, the probability density function on each of IC can be estimated separately.

To estimate the density function, a non-parametric kernel density estimation is applied on each of the independent component [19]. The kernel density estimation for the  $j$ -th component is defined by

$$\hat{f}_j(x) = \frac{1}{nh} \sum_{i=1}^n K\left(\frac{x - \mathbf{B}_{i,j}}{h}\right) \quad (5.8)$$

where  $\mathbf{B}_{i,j}$  is the coefficient values in the matrix  $\mathbf{B}$  in (5.7) at  $j$ -th independent component. The bandwidth  $h$  and the kernel function  $K(u)$  are the two parameters of the kernel density estimation method.

Gaussian function is used for the kernel function, i.e.,

$$K(u) = \frac{1}{\sqrt{2\pi}} \exp\left(-\frac{u^2}{2}\right) \quad (5.9)$$

Note that the choice of kernel function is not really critical for the kernel density estimation, but rather for the choice of bandwidth [19].

The bandwidth  $h$  controls the amount of smoothing. A small difference in setting  $h$  can yield a big difference in the probability function. We applied the Sheather-Jones solve-

the-plugin method level 2 to estimate the optimal bandwidth [20]. This solve-the-plugin method solves an unknown functional parameter in the optimal bandwidth equation directly from the sample distribution.

After estimating the probability density function  $\hat{f}_j(x)$  for each IC, the quantification of abnormalities is straightforward. A probability map of being abnormal for each IC is defined as

$$\hat{p}_j(x) = 1 - \hat{f}_j(x) . \quad (5.10)$$

A threshold value  $\rho$  is defined to determine the abnormality. Coefficient values that fall below that threshold are considered to be normal.

## 5.2 Experimental Results

### 5.2.1 Model construction

An ICA model of healthy myocardial heart contraction was built by selecting epicardial and endocardial borders at ED and ES phases from 42 healthy volunteers. The mid ventricular level from short-axis MRI was taken from each subject. Contours were drawn manually by an expert and used 60 landmark points per contour, defined by equi-angular sampling from the center of the myocardium. To ensure point correspondence between shapes, a fixed reference point was defined at the intersection between left and right ventricle.

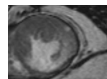
ICA was performed using FastICA algorithm [7], implemented in Matlab (Matlab v6.5, The Mathworks, Natick, MA, USA). FastICA uses an optimization algorithm to maximize the *non-Gaussianity* of each component's direction to ensure that components are statistically independent between each other. The nonlinearity objective function used in the optimization process is  $g(y) = 3y^2$  (or *pow*) and with symmetric orthogonalization. The number of independent components was determined following Himberg's approach [17], as has been described in Section 5.1.2. The number of trials was set to 20.

### 5.2.2 Qualitative prediction results of contractility improvement

To qualitatively evaluate the prediction of myocardial contractility improvement under stress, MR data of six representative patients with acute myocardial infarction were selected. The threshold value,  $\rho$ , separating abnormal from normal coefficient values, is empirically defined as 0.8. Figure 5.5 and Figure 5.6 show the visualization of abnormal regions in rest and stress for the six patients.

The left and middle figures are the quantification of abnormal contraction regions from the method in rest and stress, respectively. Regions with abnormal contraction are shown with dark colors inside of the myocardium. The darker the color, the more abnormal the regional motion. Thus regions with contractility improvement are visible by the decreasing amount of darkness from rest to stress in the corresponding regions.

Each of the abnormal regions has a corresponding abnormal independent component that is shown as bar plot at the right figure, given as the probability value of being



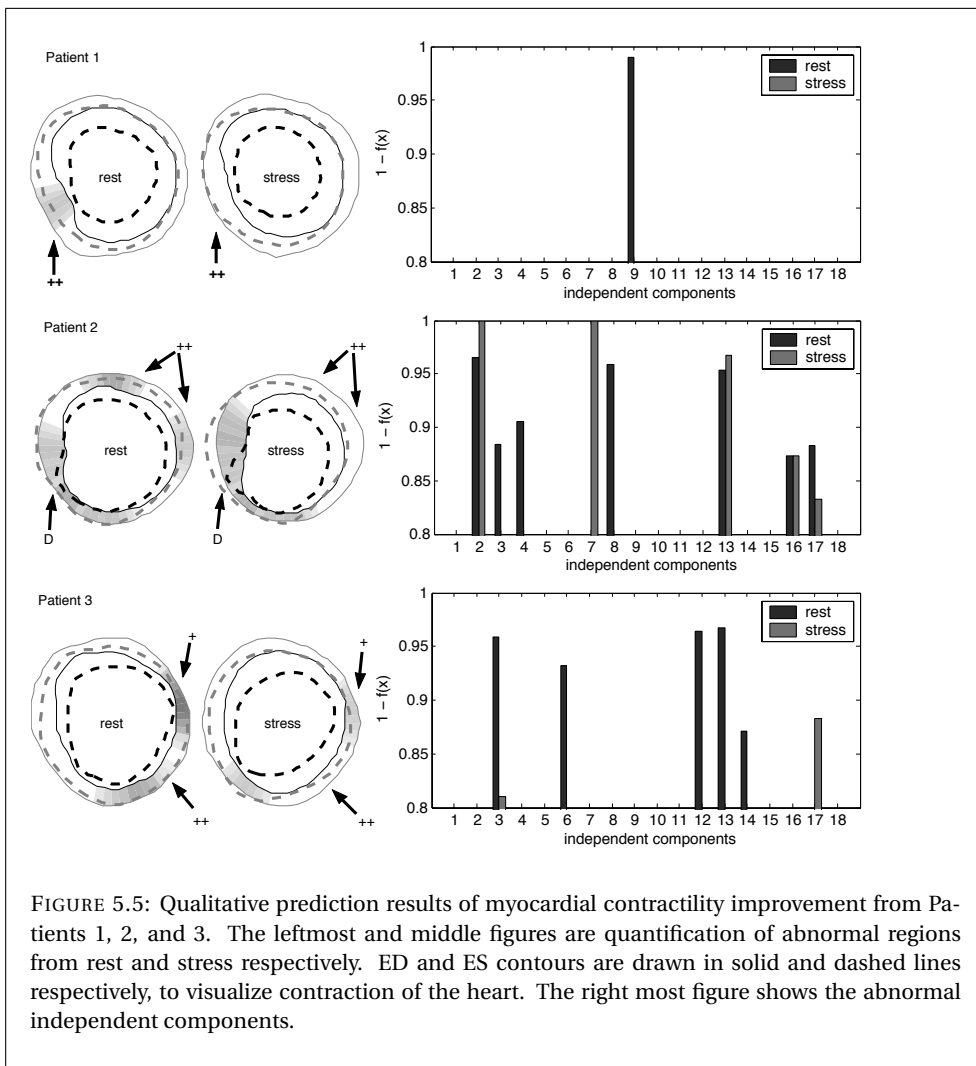


FIGURE 5.5: Qualitative prediction results of myocardial contractility improvement from Patients 1, 2, and 3. The leftmost and middle figures are quantification of abnormal regions from rest and stress respectively. ED and ES contours are drawn in solid and dashed lines respectively, to visualize contraction of the heart. The right most figure shows the abnormal independent components.

abnormal. Contractility improvement of an IC is shown as a decreasing amount of the probability value from rest to stress.

Contraction motion is visualized with the ED (solid lines) & ES (dashed lines) contours that are plotted together. It can be seen from Figure 5.5 and Figure 5.6 that regions with abnormal contraction motion correspond visually with the dark areas.

Arrows in Figure 5.5 and Figure 5.6 point to some interesting regions in each patient. If contraction in a region is improved, then the arrow is marked with '+' sign (Patient 3 and 5). Regions with a lot of contractility improvement, where they are detected as normal in stress, are marked with '++' sign. These are seen at Patient 1, 2, 3, 4 and 6.

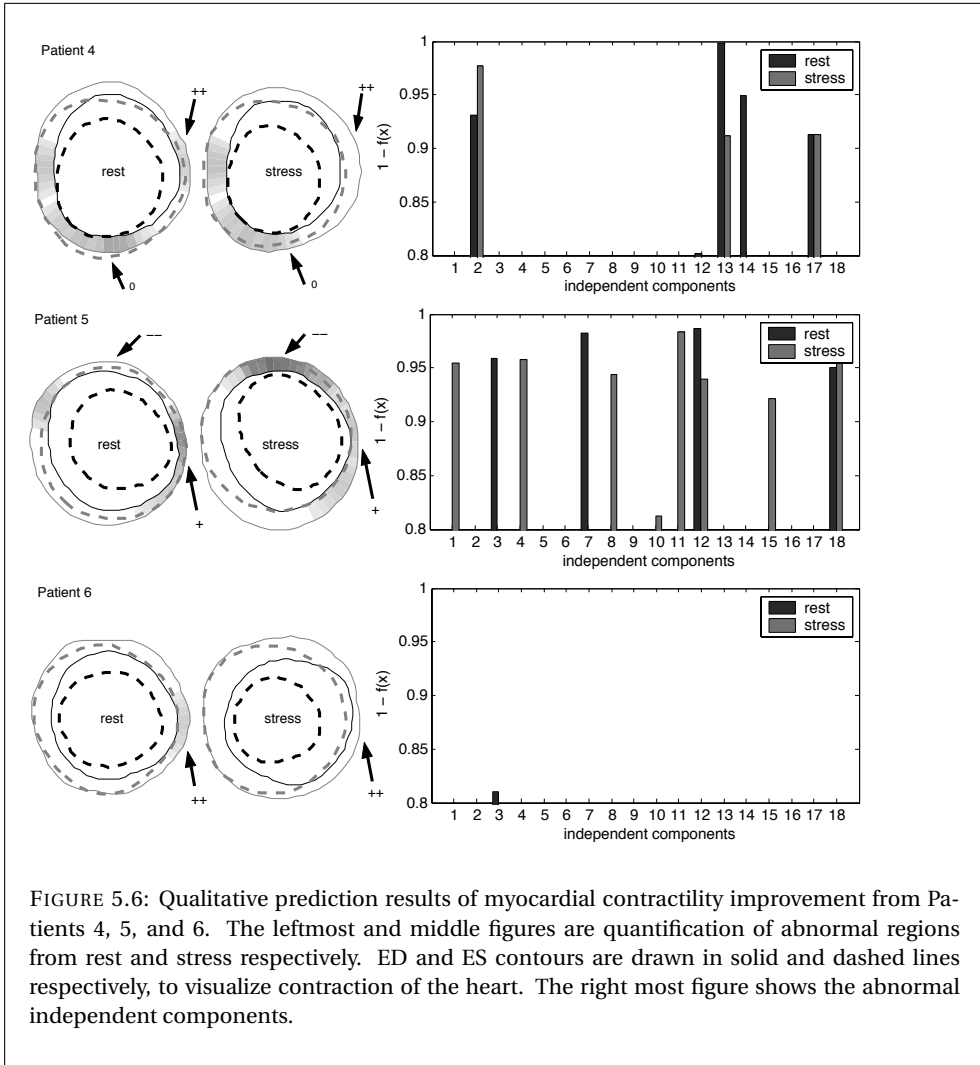
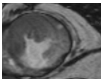


FIGURE 5.6: Qualitative prediction results of myocardial contractility improvement from Patients 4, 5, and 6. The leftmost and middle figures are quantification of abnormal regions from rest and stress respectively. ED and ES contours are drawn in solid and dashed lines respectively, to visualize contraction of the heart. The right most figure shows the abnormal independent components.

There is a case where an abnormal region does not improve its contractility in stress (Patient 4 with '0' sign) or even the contraction is getting worse in stress (Patient 5 with '-' sign). Another interesting case appears in Patient 2, where there is a region that has a small contraction in rest (see the arrow with 'D' sign), an improved contraction in stress, but abnormal motion in stress. This is detected by the model as an abnormal region.

### 5.3 Discussion

This chapter explores the potential of using ICA to model contraction of healthy hearts. The model is applied for detecting myocardial regions with abnormal contraction, both in rest and stress. Comparing the detection between rest and stress gives an indication of areas that may improve after treatment.

In Figure 5.5 and Figure 5.6, six examples of the prediction results using the ICA model are demonstrated. These examples show that the method is capable to perform comparative morphometrics between rest and stress. Abnormal myocardial regions in rest with decreasing probability value in stress are identified as viable but dysfunctional myocardium. These are regions that may gain improvement after treatment.

The detected abnormal regions both in rest and stress correspond visually with the lack of contractility on those regions (see Figure 5.5 and Figure 5.6). The method can also detect an abnormal motion in stress, even with increased contraction. This is possible, because the model is statistically trained from normal cardiac contraction, all deviations from normal contraction or motion are labeled as abnormal.

The current validation is still lack of gold standard data. The gold standard for the assessment of ischaemic heart disease is post-treatment data when it comes to the question whether myocardium improves or not after treatment. A proper validation for an automated contractility improvement assessment should utilize these data set.

To gain more accurate prediction of contractility improvement for the whole heart, extending the ICA model into a 3D model is necessary to detect abnormal myocardial segments [21]. This involves inclusion of three levels of short-axis MRI (apical, middle and basal) and one segment from vertical long axis.

### 5.4 References

- [1] S. R. Underwood, J. J. Bax, J. vom Dahl, M. Y. Henein, J. Knuuti, A. C. van Rossum, E. R. Schwarz, J.-L. Vanoverschelde, E. E. van der Wall, W. Wijns, and Study Group of the European Society of Cardiology, "Imaging techniques for the assessment of myocardial hibernation. Report of a Study Group of the European Society of Cardiology," *Eur Heart J*, vol. 25, no. 10, pp. 815–36, May 2004.
- [2] E. E. van der Wall, H. W. Vliegen, A. de Roos, and A. V. Bruschke, "Magnetic resonance imaging in coronary artery disease," *Circulation*, vol. 92, no. 9, pp. 2723–39, Nov 1995.
- [3] R. J. van der Geest and J. H. Reiber, "Quantification in cardiac mri," *J Magn Reson Imaging*, vol. 10, no. 5, pp. 602–8, Nov 1999.
- [4] E. Nagel and E. Fleck, "Functional MRI in ischemic heart disease based on detection of contraction abnormalities," *J Magn Reson Imaging*, vol. 10, no. 3, pp. 411–7, Sep 1999.
- [5] F. M. Baer, E. Voth, P. Theissen, H. Schicha, and U. Sechtem, "Gradient-echo magnetic resonance imaging during incremental dobutamine infusion for the localization of coronary artery stenoses," *Eur Heart J*, vol. 15, no. 2, pp. 218–25, Feb 1994.
- [6] A. Suinesiaputra, M. Üzümcü, A. F. Frangi, T. A. M. Kaandorp, J. H. C. Reiber, and B. P. F. Lelieveldt, "Detecting regional abnormal cardiac contraction in short-axis MR images using



- independent component analysis,” in *Medical Image Computing and Computer-Assisted Intervention – MICCAI 2004, Proceedings, Part I*, ser. Lecture Notes in Computer Science, C. Barillot, D. R. Haynor, and P. Hellier, Eds., vol. 3216. Springer, 2004, pp. 737–744.
- [7] A. Hyvärinen, J. Karhunen, and E. Oja, *Independent Component Analysis*. John Wiley & Sons, Inc., 2001.
- [8] S. Akaho, “Conditionally independent component analysis for supervised feature extraction,” *Neurocomputing*, vol. 49, no. 1-4, pp. 139–150, 2002.
- [9] M. S. Bartlett, J. R. Movellan, and T. J. Sejnowski, “Face recognition by independent component analysis,” *IEEE Trans. on Neural Network*, vol. 13, no. 6, pp. 1450–1464, November 2002.
- [10] T.-W. Lee and M. S. Lewicki, “Unsupervised image classification, segmentation, and enhancement using ICA mixture models,” *IEEE Transactions on Image Processing*, vol. 11, no. 3, pp. 270–279, 2002.
- [11] A. Hyvärinen, “Survey on independent component analysis,” *Neural Computing Surveys*, vol. 2, pp. 94–128, 1999.
- [12] I. L. Dryden and K. V. Mardia, *Statistical Shape Analysis*. John Wiley & Sons, 2002.
- [13] F. P. van Rugge, E. E. van der Wall, S. J. Spanjersberg, A. de Roos, N. A. Matheijssen, A. H. Zwinderman, P. R. van Dijkman, J. H. Reiber, and A. V. Brusckhe, “Magnetic resonance imaging during dobutamine stress for detection and localization of coronary artery disease. Quantitative wall motion analysis using a modification of the centerline method,” *Circulation*, vol. 90, no. 1, pp. 127–38, Jul 1994.
- [14] H. Stögbauer, R. G. Andrzejak, A. Kraskov, and P. Grassberger, “Reliability of ICA estimates with mutual information,” in *Independent Component Analysis and Blind Signal Separation Proceedings*, ser. Lecture Notes in Computer Science, C. G. Puntonet and A. Prieto, Eds., vol. 3195. Springer, 2004, pp. 209–216.
- [15] A. Cichocki, J. Karhunen, W. Kasprzak, and R. Vigário, “Neural networks for blind separation with unknown number of sources,” *Neurocomputing*, vol. 24, no. 1-3, pp. 55–93, 1999.
- [16] S. J. Roberts, “Independent component analysis: Source assessment & separation, a Bayesian approach,” *IEEE Proceedings - Vision, Image & Signal Processing*, vol. 3, no. 145, pp. 149–154, 1998.
- [17] J. Himberg, A. Hyvärinen, and F. Esposito, “Validating the independent components of neuroimaging time series via clustering and visualization,” *Neuroimage*, vol. 22, no. 3, pp. 1214–22, Jul 2004.
- [18] M. Bressan and J. Vitrià, “Independent modes of variation in point distribution models,” in *Visual Form 2001 Proceedings*, ser. Lecture Notes in Computer Science, C. Arcelli, L. P. Cordella, and G. S. di Baja, Eds., no. 2059. Springer, 2001, pp. 123–134.
- [19] B. Silverman, *Density Estimation for Statistics and Data Analysis*, ser. Monographs on Statistics and Applied Probability. London: Chapman and Hall, 1986.
- [20] M. Wand and M. C. Jones, *Kernel Smoothing*. Chapman and Hall, 1995.

- [21] M. D. Cerqueira, N. J. Weissman, V. Dilsizian, A. K. Jacobs, S. Kaul, W. K. Laskey, D. J. Pennell, J. A. Rumberger, T. Ryan, M. S. Verani, and American Heart Association Writing Group on Myocardial Segmentation and Registration for Cardiac Imaging, "Standardized myocardial segmentation and nomenclature for tomographic imaging of the heart: a statement for healthcare professionals from the Cardiac Imaging Committee of the Council on Clinical Cardiology of the American Heart Association," *Circulation*, vol. 105, no. 4, pp. 539–42, Jan 2002.

# 6

**AUTOMATED DETECTION OF REGIONAL WALL  
MOTION ABNORMALITIES BASED ON A STATISTICAL  
MODEL APPLIED TO MULTI-SLICE SHORT-AXIS  
CARDIAC MR IMAGES**

## Abstract

In this section, a statistical shape analysis method for myocardial contraction is presented that was built to detect and locate regional wall motion abnormalities (RWMA). For each slice level (base, middle and apex), 44 short-axis MR images were selected from healthy volunteers to train a statistical model of normal myocardial contraction using independent component analysis (ICA). A classification algorithm was constructed from the ICA components to automatically detect and localize abnormally contracting regions of the myocardium. The algorithm was validated on 45 patients suffering from ischemic heart disease. Two validations were performed; one with visual wall motion scores (VWMS) and the other with wall thickening (WT) used as references. Accuracy of the ICA-based method on each slice level was 69.93% (base), 89.63% (middle) and 72.78% (apex) when WT was used as reference, and 63.70% (base), 67.41% (middle) and 66.67% (apex) when VWMS was used as reference. From this observation, it is concluded that the proposed method is a promising diagnostic support tool to assist clinicians in reducing the subjectivity in VWMS.

This chapter was adapted from:

A. Suinesiaputra, A. F. Frangi, T. A. M. Kaandorp, H. J. Lamb, J. J. Bax, J. H. C. Reiber, and B. P. F. Lelieveldt. Automated detection of regional wall motion abnormalities based on a statistical model applied to multi-slice short-axis cardiac MR images. *IEEE Trans Med Imaging*, 4(28):595–607, Apr 2009.

All the knowledge I possess everyone else can  
acquire, but my heart is all my own.

---

*Die Leiden des jungen Werther*  
(The Sorrows of Young Werther)  
JOHANN WOLFGANG VON GOETHE

**A**SSESSMENT of wall motion is important to determine cardiac function in rest, in stress-induced ischemia (with high dose dobutamine echocardiographic protocols) and in the assessment of viability (with low dose dobutamine protocols). In practice, dobutamine stress echo is often applied, but there are some difficulties to image the heart properly in patients with a bad acoustic window. The analysis is also subjective, with moderate reproducibility, and quantification is not very accurate. Dobutamine MRI is an alternative method to assess regional wall motion abnormalities (RWMA). MRI has a higher resolution and does not depend on acoustic window and therefore enables more accurate quantification.

In clinical practice however, RWMA assessment mainly relies on visual analysis and interpretation of wall motion. Visual Wall Motion Scoring (VWMS) is commonly performed by following a standard issued by the American Heart Association (AHA) [1], where seventeen myocardial segments are graded by an expert from cine-MR images. Segments are graded on a five point scale: normo-kinetic, mild-hypokinetic, severe hypokinetic, akinetic and dyskkinetic.

The main problem with VWMS is the high interobserver variability. The subtle differences in cardiac motion abnormalities are difficult to score, which makes VWMS less reproducible and less objective. Also, the segment boundaries are often decided based on qualitative criteria, and may vary depending on the location of the diseased myocardium. In two studies, the interobserver agreement to assess RWMA has been investigated. Paetsch et al. [2], assessed interobserver agreement of RWMA from stress studies and their kappa coefficient ( $\kappa$ ) is 0.59. Hoffmann et al. [3] compared 3 different modalities: echocardiography ( $\kappa = 0.41$  without contrast agent and  $\kappa = 0.77$  with contrast agent), MRI ( $\kappa = 0.43$ ) and cineventriculography ( $\kappa = 0.56$ ). In conclusion, there was no modality that achieved a near perfect agreement and reader differences continue to exist even with high quality images [3]. Both studies underscore that VWMS is very subjective, not to mention that it requires an elaborate training of the observer.

The goal of the present study is to develop an automated tool to detect and localize myocardial regions that show an abnormal contractile behavior based on statistics trained from healthy wall motion. Such an automated tool would have the advantage that it would reduce the inter- and intra observer variability and subjectivity in the analysis, and as subsequently it may assist less experienced readers to arrive at a reliable assessment of regional wall motion abnormalities.



## 6.1 Introduction

### 6.1.1 Automated RWMA detection methods

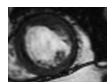
There have been prior studies aimed at developing an automatic detection of wall motion abnormalities. These studies are mainly based on shape statistics, that are described using a point distribution model (PDM) [4]. In a PDM, myocardial shapes are subsampled into a number of landmark points. A statistical model is then estimated from the set of landmark points, expressing the training population as a linear combination of an average shape and a set of characteristic eigenvariations. PDMs have been used extensively, particularly for segmentation purposes, because the model has been restricted to search such a statistically plausible shape in the image, e.g. [5, 6].

Shape parameterization using PDMs for the diagnosis of cardiac shape abnormalities was first explored by Mitchell et al. [7]. A mixed model of patients and healthy volunteers is created by taking myocardial contours only from end-diastole (ED) phase. Principal component analysis (PCA) is then used to parameterize the model. The classification between normal and abnormal shapes was evaluated by leave-one-out validation using three classification techniques: linear discriminant analysis (LDA), kernel LDA and nearest neighbor classifier. A comparable performance was found for all three classifiers. In spite of that, the model was based on static ED images, therefore solely based on shape, not incorporating any motion or contraction.

Remme et al. [8] developed a 3D left ventricle (LV) model using a fitted finite-element mesh onto the ED LV surface and selected nine clinically-termed deformation modes that were calculated by PCA. The LV deformation was estimated using tagged MR images. Two models from normal and patient subjects were investigated and the statistical inference on each nine PCA modes were estimated independently. Five out of nine PCA modes showed significant differences between normal and patient subjects. The method is useful to make a global classification between normal and patients, but not to locate the RWMA.

The first attempt to make a statistical model to quantify RWMA was proposed by Bosch et al. [9]. Only infarct patients from echocardiographic images were included to build the statistical model. The classification performance was tested by randomly splitting the data into training and test sets. PCA was used to parameterize the shape. To perform regional classification, multivariate linear regression was used to select principal components that have good correlation with the corresponding VWMS values. Bosch et al.'s study showed that VWMS correlated to the global PCA modes, although only weak correlations were found.

The drawbacks of the previous automatic wall motion abnormality studies lie on two main issues of their shape modeling. First, the typical PCA modes of shape variation affect global shape. Classifying different shape groups can only reveal global shape differences [10]. There is no information on the exact location of shape differences through PCA components. Second, the model generalization ability is limited because both patients and normal subjects are mixed in the training set (Mitchell study [7]), or only patients are included (Bosch et al. study [9]). These models are biased towards the trained pathology and they may not generalize well towards other pathologies.



### 6.1.2 Sparse decomposition in statistical shape analysis

Recently, an extension of PCA, which exploits sparseness by adding constraints of the number of nonzero loadings [11], has gained interest in shape analysis. Local variations of landmark position, as well as texture, can be achieved from Sparse PCA [12]. Applied to *corpus callosum* shapes, Sparse PCA reveals some position preferences of a local shape variation over a certain physiologically meaningful clinical outcome [13]. A preliminary report of Sparse PCA for characterizing myocardial wall motion abnormality from echocardiograms has also been reported [14].

Sparsity in Sparse PCA is induced deliberately with the additional constraint. Rather than imposing some regression techniques to enforce sparsity, an assumption of statistical independency can be applied to get a sparse decomposition. Here, Independent Component Analysis (ICA) is applied in the shape domain. ICA was originally developed in signal processing to separate mixing signals into sources without any knowledge, except the mixing signals themselves [15, 16]. The only assumption that can be made is that the source signals are independent. Typically, a mixture of signals is observed and the independent source signals can be estimated either by maximizing non-Gaussianity (the FastICA method [16]), maximizing entropy (the infomax principle [17]), or by using fourth-order cumulant matrix (the JADE algorithm [18]), among other ICA algorithms.

In shape analysis, the observed mixed signals are the training shapes. Since these signals are taken from the same group, all signals have similar characteristics and after ICA, the independent sources exhibit sparse regional spikes. Regional spike signals appear because these signals maximize statistical independency between each other for similar source signals. This phenomenon is what drives sparse decomposition for shape modeling with ICA. Unlike Sparse PCA, sparsity comes directly from ICA without additional constraints.

The statistical independency property gives an advantage of ICA over Sparse PCA for classification purposes. It allows a simple joint probability density function estimation from all components. Consequently, a probability density function can be defined for each landmark point, as will be explained in details in Section 6.2. One limitation of ICA compared to PCA (and Sparse PCA) is that the ICA components are not necessarily linked to any anatomical or physiological meaning of the training shapes. For some ICA algorithms, such as FastICA, the source signal results can even vary between different estimations due to its stochastic nature. In this study, however, anatomically meaningful sparse decomposition is not the main interest. ICA is used only for feature extraction rather than for anatomical description.

ICA has been previously used for statistical shape analysis [19, 20]. The sparseness characteristic of ICA has been exploited for an automated detection of tissue disorders in 3D aortic vessels [21] and for image segmentation [22]. In a comparison study of statistical shape analysis between different non-Euclidean metrics, it is reported that a method equivalent with ICA (Maximum Autocorrelation Factors) is one of the superior methods to decompose large shape variations [23].

### 6.1.3 Contribution of this chapter

In Chapter 3, it has been demonstrated that ICA has an advantage over PCA for local shape classification, because ICA decomposes shapes into local shape descriptors [10]. Therefore ICA is suitable to be used as a local feature classifier compared to PCA. In Chapter 4, ICA has been applied in cardiac shapes to locate abnormal regions in mid-ventricular slice level of myocardium [24]. By selecting ‘abnormal’ independent components, an ICA-based classifier gives good visual correspondence with infarcted regions indicated by delayed-enhancement MR images.

In this chapter, the ICA-based detection method is improved and quantitative validations are presented. The contribution of this chapter is twofold:

1. Proposing a statistical method to extract local myocardial contraction patterns from multi-slice short-axis MRI by ICA, and a method to detect and to localize regional wall motion abnormalities based on the ICA shape parameterization.
2. Quantitative validations of the proposed statistics-based method are presented with 45 patients suffering from ischemic heart disease.

This chapter is further organized as follows. Section 6.2 describes the methodology in-depth from building the statistical model of healthy cardiac contraction until the construction of RWMA detectors. In Section 6.3, the method is quantitatively validated, followed by a discussion in Section 6.4 and conclusions in Section 6.5.

## 6.2 Methodology

This section starts off by introducing the cardiac contraction modeling from a set of myocardial contours, such that all pose and shape variations, including shapes at the starting point of contraction (end-diastolic phase), are eliminated. In Section 6.2.2, the model is decomposed into local shape descriptors using ICA. The ICA algorithm requires the number of independent components as a parameter. A robust estimation method to estimate this parameter is given in Section 6.2.3. After the ICA model is constructed, distributions of model’s coefficient can be estimated, as described in Section 6.2.4. Finally, Section 6.2.5 explains the RWMA detection method by propagating probability density functions from ICA domain into shape domain.

### 6.2.1 Statistical Shape Modeling of Cardiac Contraction

Landmark-based statistical shape analysis was introduced in 1980s as a method to investigate the geometrical statistics of a set of shapes and their relative positions [25]. Landmarks are homologous points with point-to-point correspondences between shapes, that can be defined either mathematically, anatomically or manually. Let  $(x_i, y_i)$  be a 2D Cartesian coordinate of the  $i$ -th landmark point. A shape vector  $\mathbf{x} \in R^{2P}$  with  $P$  landmarks is defined by

$$\mathbf{x} = [x_1, y_1, x_2, y_2, \dots, x_P, y_P]^T. \quad (6.1)$$



Shapes are aligned by using Procrustes alignment [26] to eliminate variations in location, size and shape orientation. This is given by

$$\mathbf{x}^p = \frac{\mathbf{x}^T \hat{\boldsymbol{\mu}} \mathbf{x}}{\mathbf{x}^T \mathbf{x}}, \quad (6.2)$$

where  $\mathbf{x}^p$  is the shape  $\mathbf{x}$  aligned to the mean shape  $\hat{\boldsymbol{\mu}}$ . The aligned shapes are invariant under scale, translation and rotation transformations.

The mean shape  $\hat{\boldsymbol{\mu}}$  is estimated from a training set  $\{\mathbf{x}_i\}$ ,  $i = 1, \dots, N$ . Let  $\mathbf{S}$  be a matrix defined as

$$\mathbf{S} = \sum_{i=1}^N \frac{\mathbf{x}_i \mathbf{x}_i^T}{\mathbf{x}_i^T \mathbf{x}_i}. \quad (6.3)$$

The mean shape  $\hat{\boldsymbol{\mu}}$  can be found as the eigenvector corresponding to the largest eigenvalue of  $\mathbf{S}$ , provided that  $\{\mathbf{x}_i\}$  are centered to its origin, i.e.  $\mathbf{x}_i \cdot \mathbf{1} = 0$ . It has been proven that  $\hat{\boldsymbol{\mu}}$  is unique up to rotation [26]. All rotations of  $\hat{\boldsymbol{\mu}}$  are also solutions, which correspond to the same mean shape.

The aligned shape  $\mathbf{x}^p$  can be expressed in a linear generative model, given as

$$\mathbf{x}^p = \hat{\boldsymbol{\mu}} + \Phi \mathbf{c}, \quad (6.4)$$

where  $\Phi \in \mathbb{R}^{2P \times M}$  is the component matrix with  $M \leq 2P$  number of components and  $\mathbf{c} \in \mathbb{R}^M$  is a coefficient vector. The matrix  $\Phi$  decomposes the training set  $\{\mathbf{x}_i\}$  into  $M$  components.

In Chapter 4, four contours (endocardial and epicardial contours at end-diastole (ED) and end-systole (ES)) were combined serially to form a shape vector [24]. This sufficed to capture myocardial contraction. However, since the main focus is to statistically compare ‘contraction shapes’ between two individuals, geometrical variation of shapes at the beginning of contraction must be removed. Consequently, all training samples start the contraction from the same shape, providing a *unit contraction model*. This is similar to Bookstein’s coordinate system [27], where two landmark points are sent to a fixed position (known as *baseline landmarks*) allowing  $P - 2$  non-zero variation of landmark point distributions.

However, instead of using a rigid similarity transformation, thin-plate splines are applied [28] to allow deformation of the heart shape. This is necessary in particular for patients because their myocardial shapes are dissimilar from normal subjects. As an example, the effect of thin-plate spline warping on a patient shape is shown in Figure 6.1 (light gray arrows) and it is noticeable on the lower part of myocardium. On the contrary, only moving contraction vectors from the patient shape to the mean shape (dark gray arrows in Figure 6.1) does not compensate for deformation.

With the unit contraction model, the linear generative model (6.4) can be estimated only from the ES shape part. This gives an advantage of reducing half the dimension during ICA computation while preserving the contraction information. Figure 6.2 shows comparison of the point distribution model between serially combined vectors (Figure 6.2(a)) and the unit contraction model (Figure 6.2(b)).

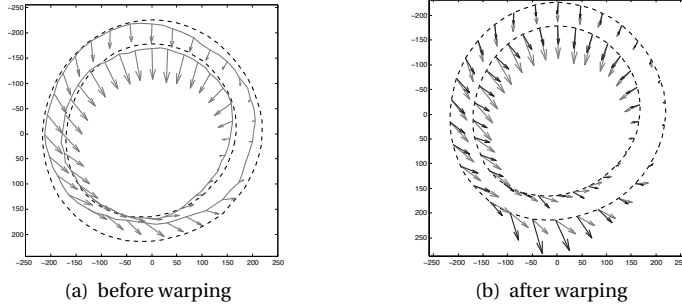


FIGURE 6.1: An example of the effect of thin-plate splines warping to the mean shape (dashed lines) during the unit contraction modeling. Light gray arrows show original contraction vector from ED to ES, while dark gray arrows show unit contraction vector from ED to ES.

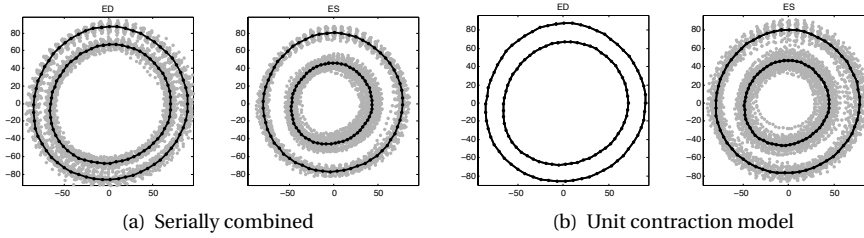


FIGURE 6.2: Shapes of endocardial and epicardial contours from 50 healthy volunteers after the Procrustes fit. The mean shapes are depicted as black thick solid lines.

## 6.2.2 Myocardial Shape Decomposition with ICA

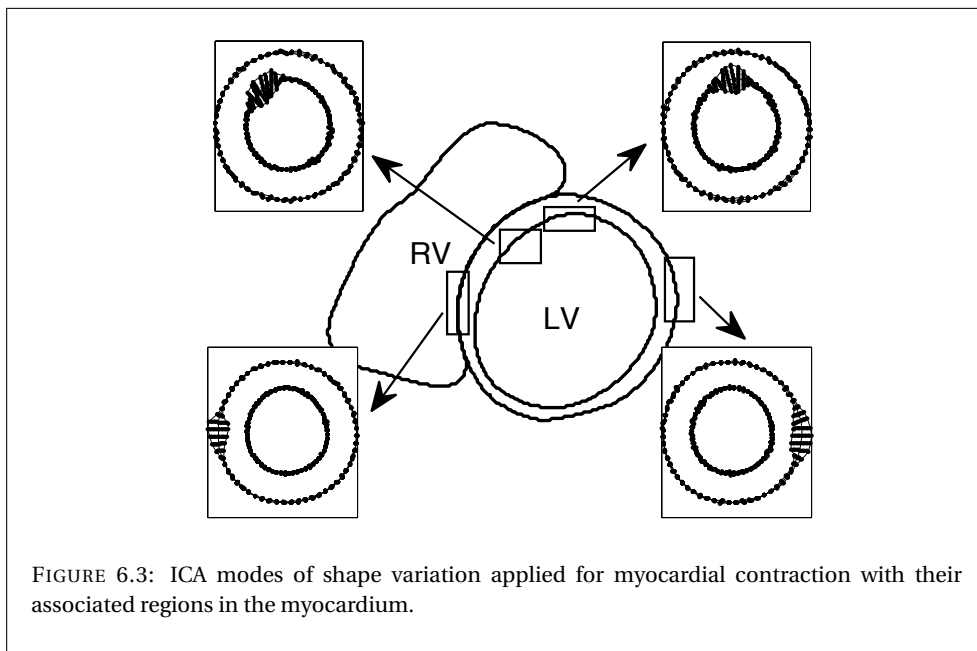
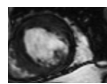
Independent component analysis (ICA) is then applied to estimate  $\Phi$  and  $\mathbf{c}$  in (6.4) by maximizing the statistical independency. In ICA terminology, the mixed signals are  $\{\mathbf{x}_i^p - \hat{\boldsymbol{\mu}}\}$  vectors, the source signals are  $\{\mathbf{c}_i\}$  vectors and the mixing matrix is  $\Phi$ .

The  $k$ -th mode of shape variation,  $\mathbf{z}_k \in \mathbb{R}^{2P}$ , is defined by

$$\mathbf{z}_k = \hat{\boldsymbol{\mu}} + \Phi \delta \mathbf{e}_k, \quad \mathbf{e}_k^{(i)} = \begin{cases} 1 & i = k, \\ 0 & i \neq k. \end{cases} \quad (6.5)$$

The modes of shape variation describe variation of the landmark point's location, triggered only by one component. The value of  $\delta$  determines the distance of the generated shape  $\mathbf{z}_k$  from the mean shape. It is usually determined from the variance of the  $k$ -th coefficient values  $\sigma_k^2$  from the model, e.g.  $-3\sigma_k \leq \delta \leq 3\sigma_k$ .

Four examples of ICA modes of variation from the myocardial contraction shape are shown in Figure 6.3, which clearly show local shape variations associated with a certain



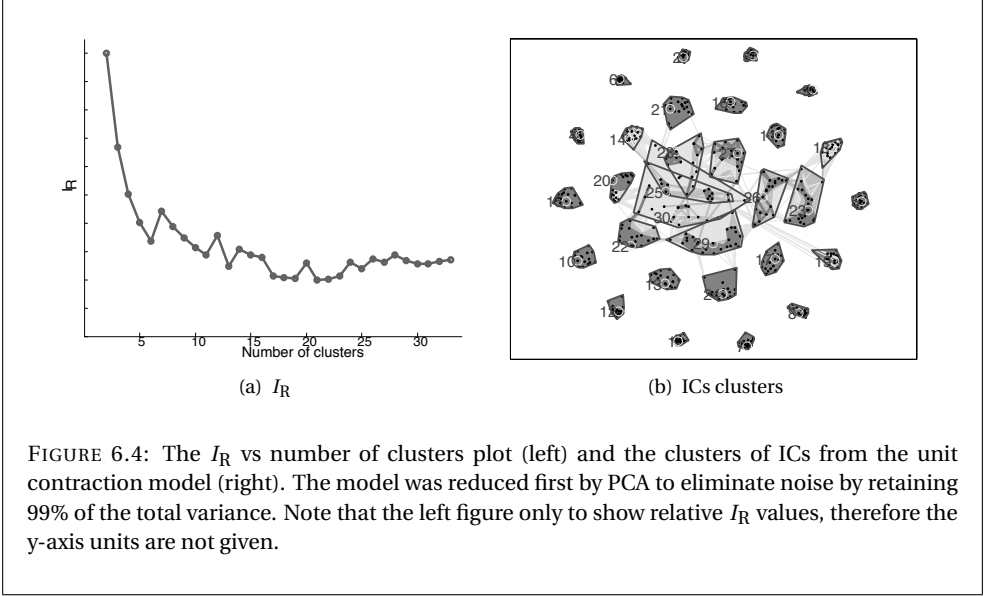
region in the myocardium. The modes of shape variation are useful to inspect a statistical shape model or to generate a new shape. In this study, the component matrix  $\Phi$  is going to be exploited for classification purposes.

### 6.2.3 Robust Estimation of Independent Components

The main difficulty in ICA is to determine the number of independent components (ICs) into which the source signals should be decomposed. Any number can be given between 1 and  $N$ . It is straightforward for a case where the number of source signals is a priori known, however, in many cases, the number of real ICs that constitute the dataset is unknown.

The number of ICs can be estimated by selecting ICs that are reliable. An IC is said to be reliable if the source signal passes a test based on specific criteria. There have been several approaches to such a reliability test, i.e. by using mutual information [29], neural networks [30], a Bayesian approach [31] or clustering techniques [32].

The clustering technique, proposed by Himberg et al. [32], is chosen in this work, because this approach is suitable for the FastICA algorithm [16]. Reliable ICs are calculated from a certain number of different ICA estimations. At each realization, ICs are collected and mapped onto a cluster space. Strong ICs are shown by their clusters that are compact and well separated from the other clusters. One disadvantage of this technique is that it needs to perform the ICA algorithm several times to estimate the number of reliable components. However, in model construction, computation time is not a critical issue, because building the ICA model is only performed once.



To indicate strong ICs, the ratio between the within-cluster and between-cluster scatter matrices is used. It is defined as

$$I_R = \frac{1}{M} \sum_{k=1}^M \frac{S_k^{\text{in}}}{S_k^{\text{ex}}}. \quad (6.6)$$

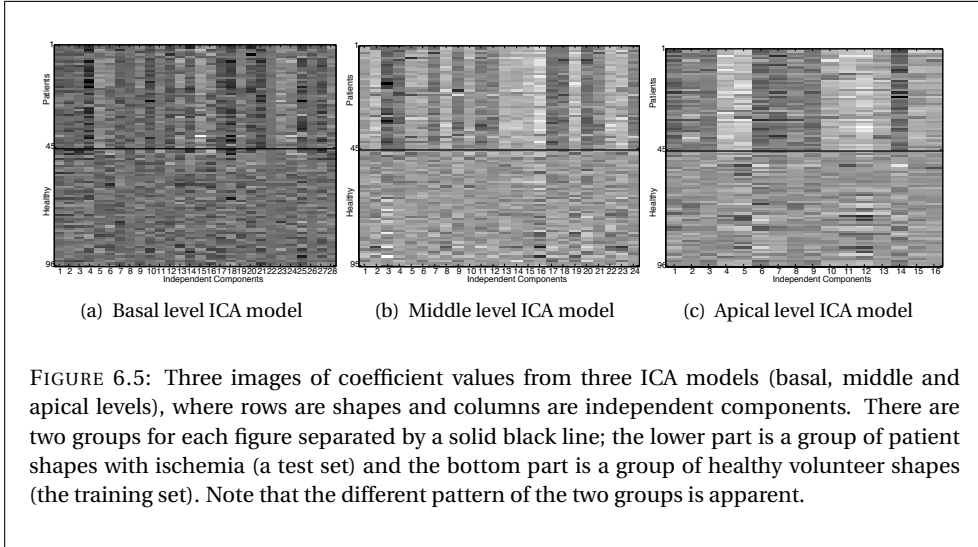
where  $S_k^{\text{in}}$  and  $S_k^{\text{ex}}$  are the within-cluster and between-cluster scatter matrices respectively, defined by

$$S_k^{\text{in}} = \frac{1}{|C_k|^2} \sum_{i,j \in C_k} (1 - \alpha_{ij}),$$

$$S_k^{\text{ex}} = \min_{k' \neq k} \frac{1}{|C_k| |C_{k'}|} \sum_{i \in C_k} \sum_{j \in C_{k'}} (1 - \alpha_{ij}),$$

with  $C_k$  and  $C_{k'}$ ,  $k = 1, \dots, M$  are two sets of indices that belong and do not belong to the  $k$ -th cluster, respectively. The  $\alpha_{ij}$  is a similarity measurement between the  $i$ -th and  $j$ -th clusters, using the absolute value of their mutual correlation coefficient. A compact cluster has a high  $S_k^{\text{ex}}$  value and an isolated cluster shows a low  $S_k^{\text{in}}$  value. A minimal  $I_R$  value is preferred. An example of an  $I_R$  plot over the number of ICs is shown in Figure 6.4(a). The corresponding cluster space is shown in Figure 6.4(b).

This clustering method is applied to determine two FastICA parameters: the number of computed ICs and the initial guess position. The number of computed ICs is selected from clusters that give a low  $I_R$  from (6.6). The initial guess parameter value is defined from the *centroid* of the IC clusters.



The modes of shape variation in ICA are not ordered, because all independent components are equally important. This is not a problem in this study, because all independent components are used as local shape detectors for abnormal shape components.

### 6.2.4 Estimating Density Functions of Independent Components

Let  $\mathbf{y} \in \mathbb{R}^{2P}$  be a new shape that is not in the training shapes  $\{\mathbf{x}_i\}$ , and it is aligned by (6.2). Using the Moore-Penrose pseudo-inverse, the projection of  $\mathbf{y}$  onto  $\Phi$  can be calculated by

$$\mathbf{c}_y = (\Phi^T \Phi)^{-1} \Phi^T (\mathbf{y} - \hat{\mu}). \quad (6.7)$$

If shape  $\mathbf{y}$  is similar to the training shapes  $\{\mathbf{x}_i\}$ , then  $\mathbf{c}_y$  resembles any one of  $\{\mathbf{c}_i\}$  in (6.4). On the contrary, if  $\mathbf{y}$  comes from a different group, for example  $\mathbf{y}$  is a pathological shape and  $\{\mathbf{x}_i\}$  is normal (healthy) shapes, then the coefficient values of  $\mathbf{c}_y$  lie outside the distribution of  $\{\mathbf{c}_i\}$ . This is shown in Figure 6.5, which displays the coefficient values from the control group (healthy volunteers) and ischemic patient group from basal, middle and apical ICA models.

Classification is then performed by specifying which elements of  $\mathbf{c}_y$  lie outside the distribution of the model. Since an IC is related to a certain segment in a shape (an ICA mode of variation exhibits local shape variation as seen in Figure 6.6(d)), detecting the  $i$ -th element of  $\mathbf{c}_y$  as an outlier yields a segment in the shape that deviates from the model.

Let  $W_k, k = 1, \dots, M$ , be random variables, each corresponds to the  $k$ -th component. By the independency, the joint probability density function of the ICA model coefficient values is defined by

$$f_{W_1, W_2, \dots, W_M}(w_1, w_2, \dots, w_M) = \prod_{k=1}^M f_{W_k}(w_k). \quad (6.8)$$

Hence, the distribution of the ICA model coefficient values can be simplified by estimating the density function of each component separately.

ICs have non Gaussian distributions, or at most only one component with a normal distribution [16]. Consequently, the normal density assumption cannot be used to estimate the density functions. Non-parametric kernel density estimation [33] is more suitable, because it does not assume a particular distribution. The density function for the  $k$ -th component can be estimated by

$$\hat{f}_{W_k}(w) = \frac{1}{Nh} \sum_{i=1}^N K\left(\frac{w - \mathbf{c}_{i,k}}{h}\right), \quad (6.9)$$

where  $w$  is a real value,  $h$  is the bandwidth of a kernel function  $K(u)$  and  $\mathbf{c}_{i,k}$  is the  $k$ -th element of the model coefficient vector  $\mathbf{c}_i$ .

Kernel density estimation method uses a mixture of  $N$  kernel functions, where  $N$  is the number of samples. Notice that in (6.9), each kernel is centered on each sample. The specific choice of kernel function is not critical [33], so the unit Gaussian kernel function is chosen, as defined below

$$K(u) = \frac{1}{\sqrt{2\pi}} \exp\left(-\frac{u^2}{2}\right). \quad (6.10)$$

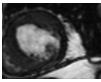
However, the selection of bandwidth  $h$  is the important factor [33]. The bandwidth controls the amount of smoothing. A small difference in  $h$  can yield a big difference in the density function. The Sheather-Jones solve-the-plugin method [34] is applied to estimate the optimal bandwidth, which solves unknown functional parameters directly from the sample distribution.

### 6.2.5 Detecting Abnormal Regions

Based on the combination of the localized ICA model of myocardial contraction and the estimated density functions, a classification boundary separating normal and abnormal subjects can be developed. 'Abnormal components' can be defined from parameters that yield low probability values from the corresponding density functions. By selecting only these abnormal components, and due to the local nature of the ICA modes, the spatial location of the wall motion abnormality can be located, and thus RWMA assessment can be automatically carried out.

Classifying a component as abnormal does not directly identify abnormal regions. The abnormal components need to be mapped to the shape domain to identify abnormal regions. Therefore, propagation of the estimated  $M$  density functions  $\{\hat{f}_{W_k}(w)\}$  to the shape domain is needed, resulting in a density function for each element in the shape vector.

The propagation of density functions can be calculated by using the inverse relation of (6.7), which transforms values in the component domain to the shape domain with the same form as in (6.4). Let  $\hat{\mu}$  in (6.7) be defined as  $\mathbf{0}$ . For notational simplicity, let us focus only on a single element in a shape vector and define  $Y$  as a random variable for the



element. From the inverse of (6.7), the random variable  $Y$  is defined as

$$Y = \phi_1 W_1 + \phi_2 W_2 + \dots + \phi_M W_M = \sum_{k=1}^M \phi_k W_k, \quad (6.11)$$

where  $\phi_1, \dots, \phi_M$  are elements of the corresponding row of  $\Phi$  for the shape vector element.

Let  $U_1, \dots, U_M$  be  $M$  new random variables, each defined as

$$U_k = \phi_k W_k. \quad (6.12)$$

It is obvious that  $U_k$  is independent from  $U_l$  for ( $k \neq l$ ), and its density function can be defined as

$$f_{U_k}(u_k) = \frac{1}{|\phi_k|} f_{W_k}\left(\frac{u_k}{\phi_k}\right). \quad (6.13)$$

Substitute (6.9) with (6.13) yields

$$f_{U_k}(u_k) = \frac{1}{|\phi_k|Nh} \sum_{i=1}^N \mathcal{K}\left(\frac{u_k - \mathbf{c}_{i,k}\phi_k}{\phi_k h}\right). \quad (6.14)$$

The density function of the sum of two independent random variables  $U_k$  and  $U_l$  is given by the convolution of  $f_{U_k}(u_k)$  and  $f_{U_l}(u_l)$  [35]. By introducing another  $M$  auxiliary random variables

$$\begin{aligned} Y_1 &= U_1 \\ Y_2 &= Y_1 + U_2 \\ &\vdots \\ Y_{M-1} &= Y_{M-2} + U_{M-1} \\ Y_M &= Y_{M-1} + U_M, \end{aligned} \quad (6.15)$$

the joint density function of  $Y$  in (6.11) can be recursively solved as follows

$$\begin{aligned} f_Y(y) &= f_{Y_M}(y_M) \\ &= \int f_{U_M}(y_M - y_{M-1}) f_{Y_{M-1}}(y_{M-1}) dy_{M-1} \\ &= \iint f_{U_M}(y_M - y_{M-1}) f_{U_{M-1}}(y_{M-1} - y_{M-2}) \\ &\quad f_{Y_{M-2}}(y_{M-2}) dy_{M-2} dy_{M-1} \\ &= \int \dots \int f_{U_M}(y_M - y_{M-1}) f_{U_{M-1}}(y_{M-1} - y_{M-2}) \\ &\quad \dots f_{U_1}(y_1) dy_1 \dots dy_{M-2} dy_{M-1} \\ &= f_{U_M} * f_{U_{M-1}} * \dots * f_{U_1}. \end{aligned} \quad (6.16)$$

Equation (6.16) defines the density function of an element of a shape vector. It is given as the series of convolutions of  $M$  density functions  $\{f_{U_i}(u_i)\}$  in (6.14), which are defined for each element IC.

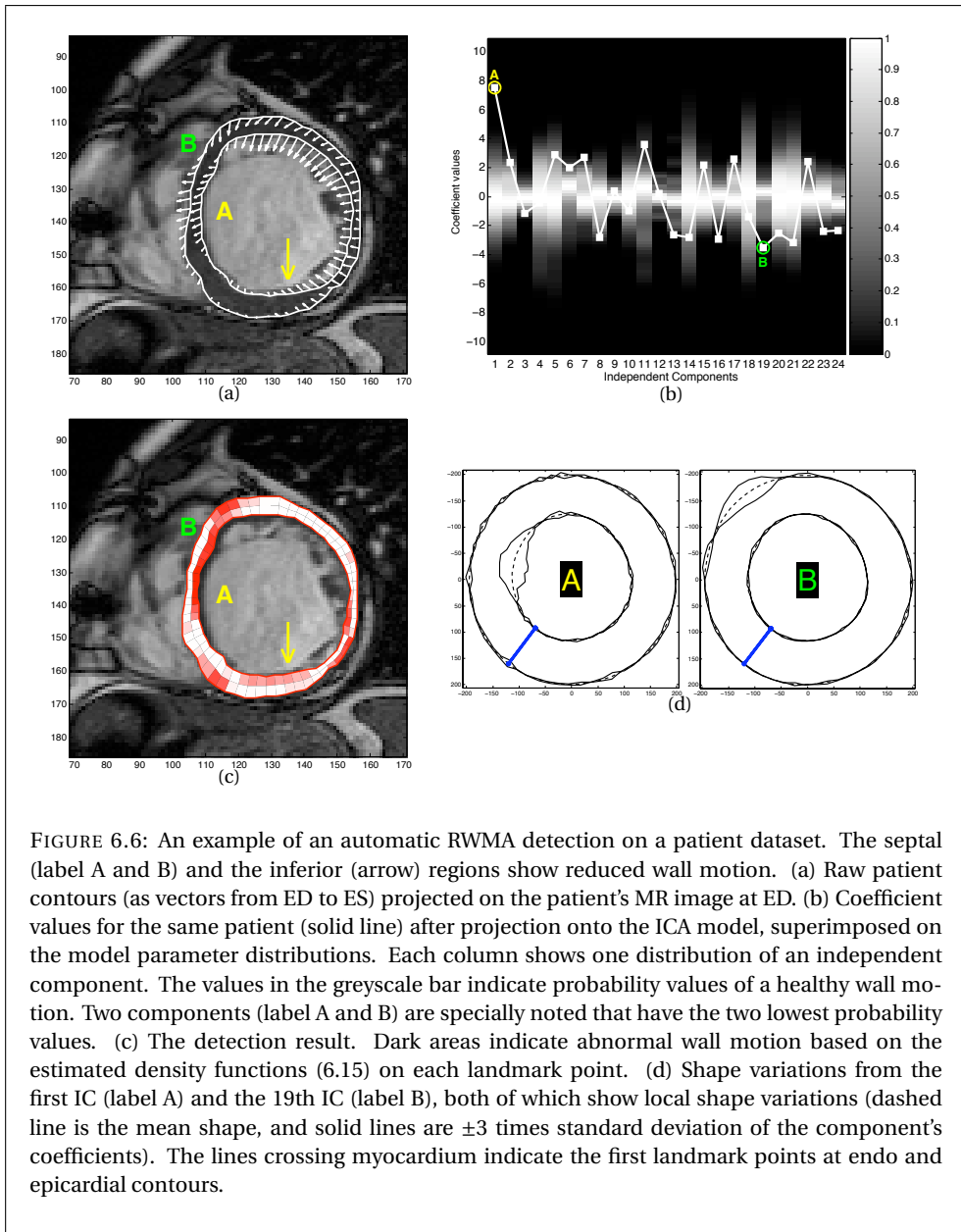
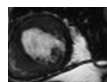


FIGURE 6.6: An example of an automatic RWMA detection on a patient dataset. The septal (label A and B) and the inferior (arrow) regions show reduced wall motion. (a) Raw patient contours (as vectors from ED to ES) projected on the patient's MR image at ED. (b) Coefficient values for the same patient (solid line) after projection onto the ICA model, superimposed on the model parameter distributions. Each column shows one distribution of an independent component. The values in the greyscale bar indicate probability values of a healthy wall motion. Two components (label A and B) are specially noted that have the two lowest probability values. (c) The detection result. Dark areas indicate abnormal wall motion based on the estimated density functions (6.15) on each landmark point. (d) Shape variations from the first IC (label A) and the 19th IC (label B), both of which show local shape variations (dashed line is the mean shape, and solid lines are  $\pm 3$  times standard deviation of the component's coefficients). The lines crossing myocardium indicate the first landmark points at endo and epicardial contours.



An example of how the density function propagation works is shown in Figure 6.6, which uses the mid-ventricular ICA model. The input contours are shown in Figure 6.6(a) as vectors from ED to ES contours that represent the myocardial contraction. The detection result is given in Figure 6.6(c), which is shown as probability values of having an abnormal shape at each landmark point. Note also how hypokinetic motion in the inferior region (the small arrow in Figure 6.6(a)) points to regions with high probability values of being abnormal (the small arrow in Figure 6.6(c)).

In Figure 6.6(b), two independent components (the 1st and the 19th ICs), which have the largest deviations of coefficient values from the model coefficient values, were labeled as A and B, respectively. When the ICA modes of variations from these two ICs are inspected (see Figure 6.6(d)), the local shape variations correlate with regions with abnormal motion. The first IC (label A) detects a reverse contraction motion in the septal region, while the 19th IC (label B) detects small wall thickening in the upper part of the septum.

## 6.3 Experimental Results

### 6.3.1 Data description and preprocessing

TABLE 6.1: Patient and Control Groups Statistics.

	Patients	Controls
Samples	45	44
Males/females	42/3	33/11
Ejection fraction (%)	$36.30 \pm 10.7$	$61.99 \pm 6.4$
Stroke volume (ml)	$75.57 \pm 19.6$	$94.94 \pm 21.5$

Myocardial contours of short-axis MR images were collected from two groups: a control group for model training and a patient group for classification testing. The control group consists of healthy volunteers, whereas the patient group consists of patients suffering from chronic coronary artery disease, with a depressed LV function. Baseline statistics of both groups are shown in Table 6.1, which also shows that ejection fraction and stroke volume is significantly different between the two groups.

MR images were acquired by 1.5T Gyroscan ACS-NT MRI scanner (Philips Medical Systems, Best, The Netherlands) and only short-axis view datasets were used that cover the LV from apex to base. End-diastole (ED) and end-systole (ES) phases from basal, mid-ventricular and apical levels were selected. Epi- and endocardial contours were manually drawn by an expert.

Visual wall motion scores (VWMS) for the patient group were performed for each segment by an experienced cardiologist on a 5-point scale: normokinetic, mild-hypokinetic, severe-hypokinetic, akinetic and dyskinetic. During the scoring process, cine-MRI viewing of the short-axis views was used and the observer was blinded to the result of the proposed method. VWMS was performed on 6 segments at the basal level, 6 segments at the mid-ventricular level, and 4 segments at the apical level. To determine the segment

TABLE 6.2: RWMA validations using WT (top) and VWMS (bottom) as reference

Validation using WT as a reference (WT benchmarking)						
	ICA-based Method			VWMS		
	acc. (%)	sens. (%)	spec. (%)	acc. (%)	sens. (%)	spec. (%)
base	69.63	76.92	66.67	66.67	69.23	65.62
middle	89.63	85.48	90.87	76.30	56.45	82.21
apex	72.78	72.97	72.73	63.33	54.05	65.73

Validation using VWMS as a reference (VWMS benchmarking)						
	ICA-based Method			WT		
	acc. (%)	sens. (%)	spec. (%)	acc. (%)	sens. (%)	spec. (%)
base	63.70	60.83	66.00	70.00	65.83	73.33
middle	67.41	65.12	69.50	68.52	60.47	75.89
apex	66.67	59.42	71.17	62.22	60.87	63.06

Each percentage value was computed with all segments included after determining the optimal cut-off boundary value.

locations, the American Heart Association (AHA) standard for myocardial segmentation was adopted [1]. Wall thickening (WT) was calculated by using dedicated quantitative MR measurement software MR Analytical Software System (MASS v5.0, Medis, Leiden, the Netherlands) [36]). WT is defined in term of percentage systolic thickening, calculated per landmark point as defined by

$$WT = \frac{w_{es} - w_{ed}}{w_{ed}} \times 100\%, \quad (6.17)$$

where  $w_{es}$  and  $w_{ed}$  are myocardial wall thickness (the distance from endocardial and epicardial contours) at end systolic and end diastolic respectively.

For ICA modeling, landmarks were defined by equi-angular sampling of epi- and endocardial contours from the center of myocardium. The number of landmarks per segment was set to 10, producing 60 landmarks per contour for basal and middle slices and 40 for apical slices. To ensure point-to-point correspondence between subjects, a fixed anatomical reference point was defined at the intersection between the left and right ventricle at the inferior region. The ICA model was calculated with FastICA algorithm [16], implemented in Matlab (Matlab v6.5, The Mathworks, Natick, MA, USA). The non-linear objective function parameter in FastICA was  $g(y) = 3y^2$  and the symmetric orthogonalization parameter was used.

### 6.3.2 Validation Method

As described before, VWMS is sensitive to high subjectivity and variability [2, 3]. Therefore, to enable an objective performance assesment of the proposed method, two validations were performed by establishing two types of benchmarking. The first one is by selecting

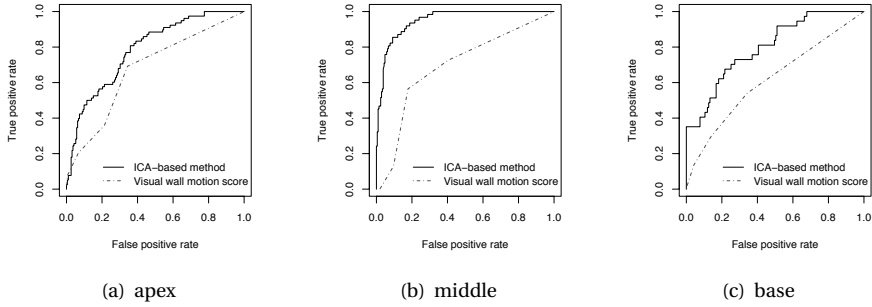


FIGURE 6.7: The performance of the ICA-based method compared with VWMS from the WT benchmarking.

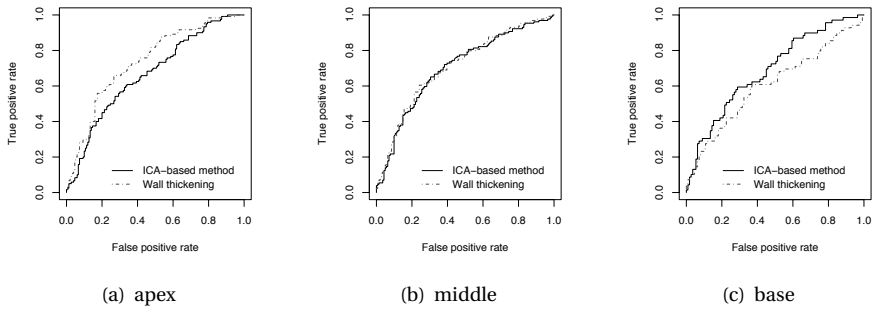


FIGURE 6.8: The performance of the ICA-based method compared with WT from the VWMS benchmarking.

WT as a point of reference to compare the ICA-based method with VWMS (WT benchmarking) and the second one is by selecting VWMS as another point of reference to compare the ICA-based method with WT (VWMS benchmarking). In the WT benchmarking, a threshold value of 10% was determined as the boundary between normal and reduced WT [37]. In the VWMS benchmarking, the classification boundary is converted into binary values: 0 for normokinetic region and 1 for other dyskinetic regions.

To evaluate the performance of the diagnostic methods in both benchmarking tests, receiver operating characteristics (ROC) curves were used. ROC graph is a standard graphical tool to visually compare different classification methods [38]. The optimal cut-off value to define classification boundary can also be estimated by using ROC curve, which is defined by minimizing  $(1 - \text{sensitivity})^2 + (1 - \text{specificity})^2$ . The optimal cut-off value was

then used to calculate the performance of a method in terms of accuracy, sensitivity and specificity, as given by

$$\text{acc} = \frac{T_P + T_N}{P + N}, \quad \text{spec} = \frac{T_N}{N}, \quad \text{sens} = \frac{T_P}{P}, \quad (6.18)$$

where  $T_P$  and  $T_N$  are true positive (the number of segments that are correctly identified as abnormal) and true negative (the number of segments that are correctly identified as normal) values, respectively. The total number of abnormal (positive) and normal (negative) segments are  $P$  and  $N$ . The ROC package developed by [39] was used to generate ROC graphs.

### 6.3.3 Classification performance

Five examples of the automated detection result are presented in Figure 6.9, side-by-side with the corresponding MR image sequences. Corresponding RWMA areas (white arrows) are found in the same place with the estimated abnormal wall motion from the automated method. Table 6.2 shows the classification performance using the WT and the VWMS benchmarking tests. Compared to VWMS in the WT benchmarking, accuracy of the ICA-based method is significantly higher. This is also the case for sensitivity and specificity measurements. The highest performance was achieved in the mid-ventricular slice model with the average of almost 89.6% for accuracy, 85.5% of sensitivity and 90.9% of specificity. During the VWMS benchmarking, the ICA-based method performance is comparable with WT.

ROC curves from each ventricular slice level are given in Figure 6.7 and Figure 6.8. In all cases, the area under ROC curves of the proposed method are larger than VWMS, indicating that the ICA-based method gives a higher performance. The area under ROC curve of the ICA-based method for the basal slice is slightly smaller than WT, while it is slightly larger for the apical slice. Interestingly, the area under the ROC curve of the proposed method for the mid-ventricular slice is almost the equal with WT, but this does not imply that the results of both methods are equal (see Section 6.3.5).

### 6.3.4 Disagreement with visual wall motion score

A common disagreement between the ICA-based method with VWMS lies in the extend of abnormal landmark points that cross segment boundaries. Observers score on segments, instead of points. Boundaries between segments can be visually repositioned according to the observer's interpretation while looking at the cine images. Therefore it is often the case that the automated method detected abnormal points only in a partial myocardial segment as pointed by arrows in Figure 6.10(a). The false positive result in Figure 6.10(a) belongs to the same abnormal motion of the inferior segment marked by VWMS. The visual score assigned the abnormal motion only to one segment, while the automated method detected all the abnormal points preserving the wall motion continuity.

Another problem of the proposed method in the current study is the lack of full cardiac cycle information in the shapes that are defined only by ED and ES phases. In a few cases, as one given in Figure 6.10(b), the observer detected a wall motion peculiarity from the

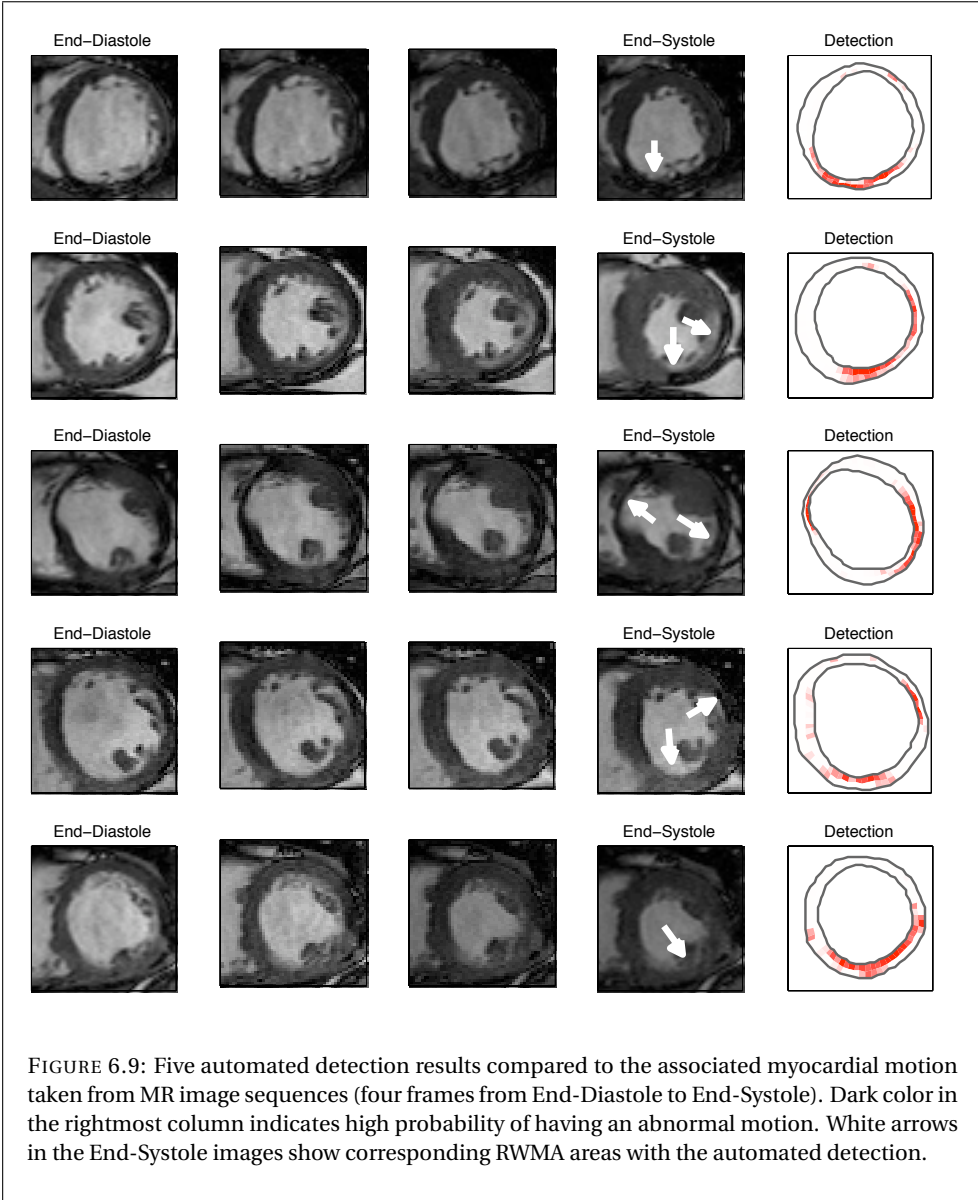
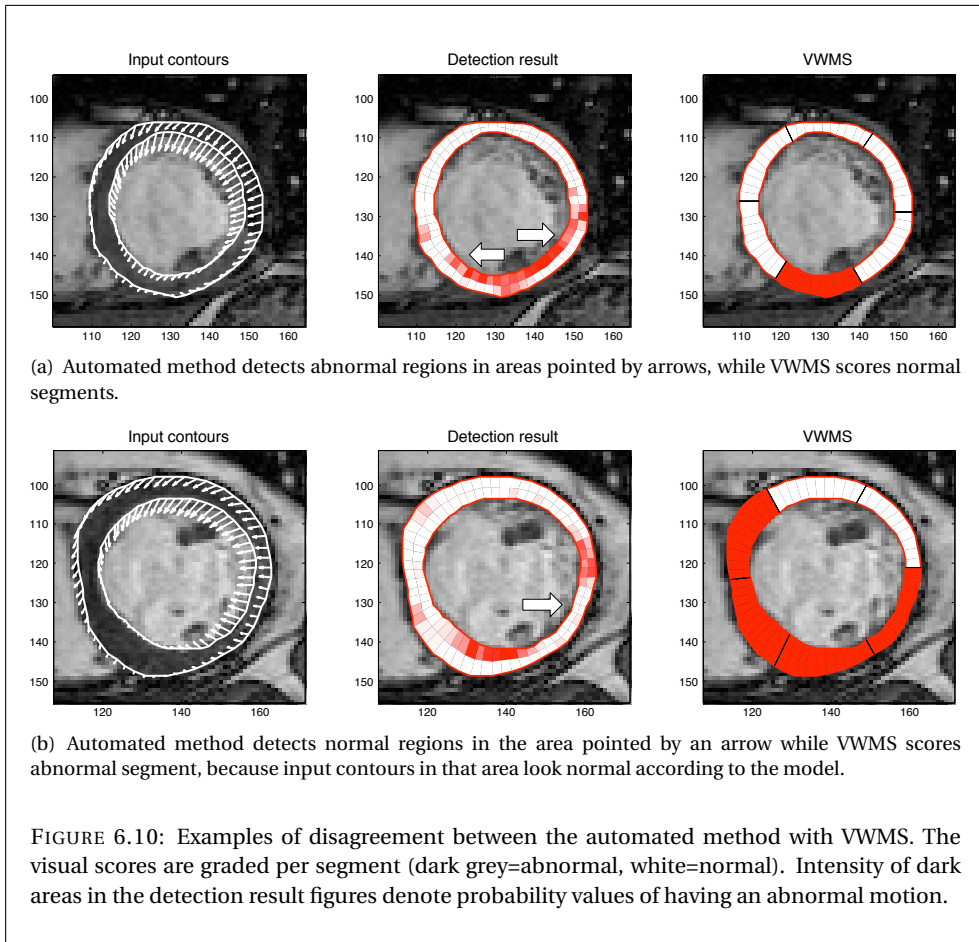


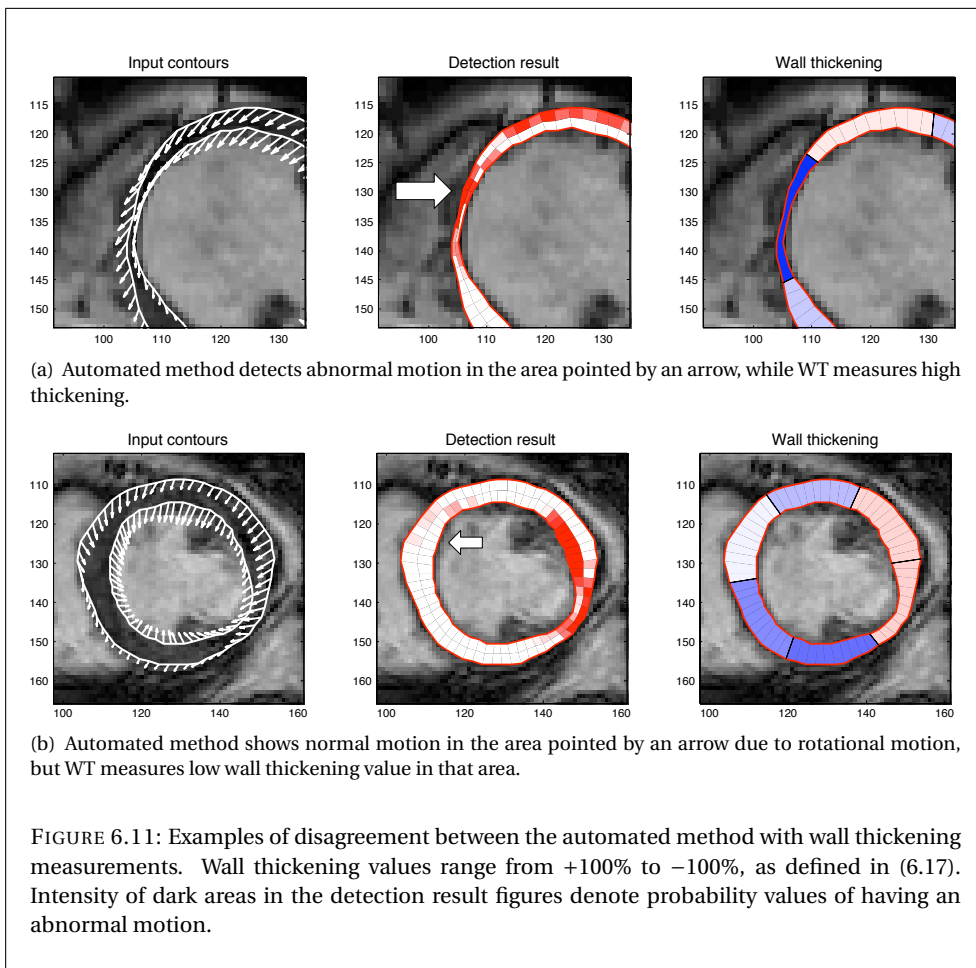
FIGURE 6.9: Five automated detection results compared to the associated myocardial motion taken from MR image sequences (four frames from End-Diastole to End-Systole). Dark color in the rightmost column indicates high probability of having an abnormal motion. White arrows in the End-Systole images show corresponding RWMA areas with the automated detection.



cine images, while the automated method detected normal contraction because shapes at ES looks normal according to the statistics of the model. The arrow in Figure 6.10(b) shows a good ED to ES contraction. In this case, the automated method missed the abnormal wall motion because it did not include the information of the contour positions between ED and ES phases.

### 6.3.5 Disagreement with wall thickening

ROC curves of the ICA-based method and wall thickening during the VWMS benchmarking in Figure 6.8 show high degree of similar performances. The main reason is that statistical shapes in the ICA-based method was constructed from ED and ES contours, which are the same phases to define the wall thickening value (see (6.17)). However there are substantial differences between the ICA-based method and wall thickening results.



WT measurement does not consider geometry of the contours. It only subtracts myocardial thickness from ES to ED, regardless whether the contraction movement performs in an unusual way. An example of this case is shown in Figure 6.11(a), where the myocardium at the anteroseptal region (pointed by an arrow) is moving towards the right ventricle. It means that the myocardium at that region is dilating instead of contracting. The ICA-based method however is still capable to detect this kind of movement as abnormal. This shows that the statistical model does not merely imitate wall thickening, but it also includes wall motion information implicitly.

As the statistical model contains wall motion, the automated method sometimes detects regions with low thickening as normal, because the contraction shape is still normal according to the model. Figure 6.11(b) shows this case of disagreement. The myocardial region pointed by an arrow in Figure 6.11(b) shows rotational movement while contracting

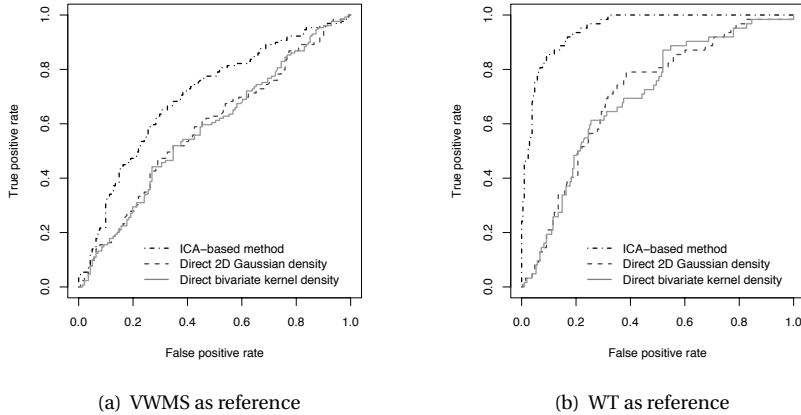


FIGURE 6.12: Comparisons between the ICA-based detection method with the direct landmark density estimation using a bivariate normal (2D Gaussian) density model. Both ROC curves were calculated from mid-ventricular slice level.

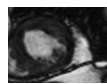
with low wall thickening.

### 6.3.6 Comparison with direct landmark density estimation

The proposed method starts off by modeling statistics of training shapes with ICA. The estimated density functions in the IC domain are then propagated into the shape domain (6.16), resulting a density function for each landmark point. Having density functions at the level of landmark points may raise some issues over the benefit of using ICA modeling instead of directly estimating probability density functions at each landmark point, e.g. by using a bivariate normal distribution model, which would reduce the complexity.

In this study, ICA is particularly used as a feature extraction to model the shape of myocardial contraction. The contraction shape at one landmark is not only determined by the distribution of that particular landmark, but is also affected by its neighbors. The closer the neighbor landmark, the higher its contribution. Density functions for each landmark point have been calculated based on all independent components, which means that all other point distributions contribute to estimating it. This is different from direct landmark point density estimation which only estimates a distribution model of a particular landmark point without considering its spatial context.

To perform a comparison between ICA and direct landmark density estimation, two bivariate density functions were estimated directly at each landmark point [40]: one with a gaussian function and the other with a non-parametric kernel density function. Only the



mid-ventricular slice level was used because the contraction motion is most pronounced in this level. All the three methods received the same input points, which are the landmark points from End-Systole contours after unit contraction (see Figure 6.2(b)). Hence, they only differ in how the probability density functions are estimated.

Figure 6.12(a) and Figure 6.12(b) show the ROC curves of the three methods during the WT and VWMS benchmarking tests, respectively. The ROC curves show that the ICA-based method gives much better performance compared to the direct landmark density estimations, especially in Figure 6.12(b). This proves that direct landmark density estimation is not enough to capture motion contraction, and that modeling landmarks in their shape context is thus necessary. ICA was chosen because it gives local shape variation and it allows the propagation of the density functions to the shape domain.

## 6.4 Discussion

### 6.4.1 Method performance

From both benchmarking tests, the mid-ventricular slice level gives the highest performance (almost 90% in WT benchmarking and 67% in VWMS benchmarking). This is due to fact that wall motion in the mid-ventricular level is well defined and more stable compared with basal and apical levels; thus regional wall motion abnormalities can be well separated from the control group.

In the basal level, there are large shape variations in the septal region due to the close proximity of the valve opening which gives a lower accuracy for abnormal motion in that region. This conforms with the lowest accuracy outcome in the basal level compared with the other levels in both benchmarking tests. In the apical level, the ICA-based method is still capable to detect abnormal motion (73% and 67%). However, the method's sensitivity reduced significantly (59% in VWMS benchmarking).

### 6.4.2 Study limitations

Both the ICA model and the RWMA detection method are sensitive to the quality of the myocardial contours. To construct a good ICA model, high quality myocardial contours are required. This requires a low inter- and intraobserver variation in the contours (if they are manually drawn), or a low segmentation error (if the contours are segmented automatically). This issue is not specific to the proposed method, but it is inherent to any quantitative regional LV function measurement.

In the present study, a binary classification between normal and abnormal motion is proposed. Classification of a specific type of abnormal motion, i.e. hypokinetic, akinetic and dyskinetic, are not presented yet. As yet, the method therefore only serves as a computer-aided tool to draw the clinician's attention to the suspected abnormal motion areas in the myocardium; staging of the wall motion abnormality may still be performed visually.

The current automated method works by modeling contractility patterns for each ventricular slice level. Therefore the method does not capture the three dimensional heart

motion. It is natural to extend the ICA model into 3D but we decided to model 2D cardiac contraction based on two reasons. During visual scoring, observers assess RWMA by looking at planar motion on multi-slice cine-MR sequences. Therefore by modeling multi-slice 2D ICA model, VWMS is emulated. Another reason is the dimensionality problem. Increasing the shape dimensionality also increases the necessary amount of training shapes required to generate a representative model.

The main benefit of the proposed method over previously described work on automatic wall motion classification (Bosch et al. [9], Mitchell et al. [7] and Remme et al. [41] studies) is that the method does not only distinguish between normals and patients, but also localizes the anomalies. Furthermore, the model is trained on normal subjects, therefore it is not biased towards a specific pathology, and can be deployed to other disease processes that manifest themselves in regional contraction anomalies.

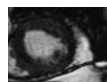
### **6.4.3 Clinical utility**

The accuracy of the automated method in comparison with visual observers' scores ranges from 63.70%–67.41%. This disagreement still hinders the application of the proposed method in clinical routines. Even VWMS is often difficult to be applied in clinical settings due to high intra- and interobserver variations [2, 3]. Hoffmann et al. study [3] found that the accuracy of RWMA assessment from cine MRI from three independent observers is 62%, 55% and 86%. In the current validation, only one observer performed the scoring. To make a better quantitative validation, it may therefore be needed to set a consensus reading from more than one independent observer.

Nonetheless, there is still room for improving the proposed method to reach the agreement with visual observers. The most prominent difference between visual observers with the automated method is the temporal resolution. This problem has been addressed in Section 6.3.4. There are two possibilities to enhance the statistical model with respect to this problem. First is to include more shapes taken from in between ED and ES frames. Interpolation might be needed in this case, because the number of images per one cardiac cycle is different between subjects. Second is to enhance point correspondences between time frames. In the current implementation, there is no particular verification of point correspondences between ED and ES. This solution can improve the statistical model particularly in basal slice where valve opening causes a lot of shape variations in the septum.

## **6.5 Conclusion**

A statistical model-based method to automatically detect RWMA in cardiac MR short-axis views of the myocardium has been presented. The model can capture the myocardial contractility pattern in a framework where all shapes contract from the same shape. This leads to a direct statistical analysis of the contraction by eliminating the shape variations at the ED phase. Furthermore, the automated process does not depend on a specific segmentation algorithm to produce the diagnostic results. The idea behind this approach is to construct a full pipeline of automated cardiac MRI analysis from segmentation to diagnosis, aimed to help clinicians in their daily routines.



Modeling by ICA proved very suitable in this study, because ICA produces local shape variations that are needed by the detection method to locate RWMA segments. The statistical independence property of ICA gives a benefit of an easy derivation of local probability density functions from the component domain to the shape domain.

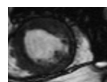
The validation showed an almost similar performance compared to WT during the VWMS benchmarking, and a higher accuracy performance than VWMS during the WT benchmarking. Two advantages of this method over VWMS are (1) given myocardial contours, the detection method is automatic, and (2) the method does not require a specialized rater, as VWMS does, to arrive to a clinically meaningful interpretation.

Having a reference of normal cardiac contraction has another advantage. The same model can be used for follow-up studies, for instance the stress MR study or post-operative MRI, to investigate whether the same patient exhibits improvement in the cardiac function towards the normal behavior reference. This opens the path towards an automated viability assessment, an important diagnosis in the clinical routines. With the same concept of detecting RWMA regions, viability can be analyzed from stress MR studies by comparing RWMA regions in the corresponding rest MR studies. The functional improvement can be detected by measuring the direction of the patient's coefficient value from rest to stress. A pilot study to assess functional improvement has been presented in [42], as well as linking this method with an automated segmentation of cardiac MR images [43, 44], enabling a full pipeline of automated cardiac MR image analysis.

## 6.6 References

- [1] M. D. Cerqueira, N. J. Weissman, V. Dilsizian, A. K. Jacobs, S. Kaul, W. K. Laskey, D. J. Pennell, J. A. Rumberger, T. Ryan, and M. S. Verani, "Standardized myocardial segmentation and nomenclature for tomographic imaging of the heart: A statement for healthcare professionals from the cardiac imaging committee of the council on clinical cardiology of the American Heart Association." *Circulation*, vol. 105, no. 4, pp. 539–542, 2002.
- [2] I. Paetsch, C. Jahnke, V. A. Ferrari, F. E. Rademakers, P. A. Pellikka, W. G. Hundley, D. Poldermans, J. J. Bax, K. Wegscheider, E. Fleck, and E. Nagel, "Determination of interobserver variability for identifying inducible left ventricular wall motion abnormalities during dobutamine stress magnetic resonance imaging," *European Heart Journal*, vol. 27, no. 12, pp. 1459–1464, 2006.
- [3] R. Hoffmann, S. von Bardeleben, J. D. Kasprzak, A. C. Borges, F. ten Cate, C. Firschke, S. Lafitte, N. Al-Saadi, S. Kuntz-Hehner, G. Horstick, C. Greis, M. Engelhardt, J.-L. Vanoverschelde, and H. Becher, "Analysis of regional left ventricular function by cineventriculography, cardiac magnetic resonance imaging, and unenhanced and contrast-enhanced echocardiography," *Journal of the American College of Cardiology*, vol. 47, no. 1, pp. 121–128, Jan 2006.
- [4] T. F. Cootes, D. Cooper, C. J. Taylor, and J. Graham, "Active shape models - their training and application," *Computer Vision and Image Understanding*, vol. 61, no. 1, pp. 38–59, Jan 1995.
- [5] R. Beichel, H. Bischof, F. Leberl, and M. Sonka, "Robust active appearance models and their application to medical image analysis," *IEEE Trans. on Medical Imaging*, vol. 24, no. 9, pp. 1151–1169, Sep 2005.

- [6] B. van Ginneken, A. F. Frangi, J. Staal, B. ter Haar Romeny, and M. A. Viergever, "Active shape model segmentation with optimal features," *IEEE Trans. on Medical Imaging*, vol. 21, no. 8, pp. 924–933, Aug 2002.
- [7] S. C. Mitchell, B. P. F. Lelieveldt, H. G. Bosch, J. H. C. Reiber, and M. Sonka, "Disease characterization of active appearance model coefficients," in *Proc. SPIE Medical Imaging 2003, Vol. 5032*, M. Sonka and J. M. Fitzpatrick, Eds., San Diego, USA, May 2003, pp. 38–49.
- [8] E. W. Remme, A. A. Young, K. F. Augenstein, B. Cowan, and P. J. Hunter, "Extraction and quantification of left ventricular deformation modes," *IEEE Trans. on Biomedical Engineering*, vol. 51, no. 11, pp. 1923–1930, Nov 2004.
- [9] J. G. Bosch, F. Nijland, S. C. Mitchell, B. P. F. Lelieveldt, O. Kamp, J. H. C. Reiber, and M. Sonka, "Computer-aided diagnosis via model-based shape analysis: Automated classification of wall motion abnormalities in echocardiograms," *Academic Radiology*, vol. 12, no. 3, pp. 358–367, Mar 2005.
- [10] A. Suinesiaputra, A. F. Frangi, M. Üzümcü, J. H. C. R. Reiber, and B. P. F. Lelieveldt, "Extraction of myocardial contractility patterns from short-axis MR images using independent component analysis," in *Computer Vision and Mathematical Methods in Medical and Biomedical Image Analysis, LNCS 3117*, M. Sonka, I. A. Kakadiaris, and J. Kybic, Eds. Springer-Verlag, 2004, pp. 75–86.
- [11] H. Zou, T. Hastie, and R. Tibshirani, "Sparse principal component analysis," *Journal of Computational and Graphical Statistics*, vol. 15, pp. 265 – 286, June 2006.
- [12] M. B. Stegmann, K. Stöjstrand, and R. Larsen, "Sparse modeling of landmark and texture variability using the orthomax criterion," in *Int. Symposium on Medical Imaging 2006*, vol. 6144. SPIE, Feb. 2006.
- [13] K. Sjostrand, E. Rostrup, C. Ryberg, R. Larsen, C. Studholme, H. Baezner, J. Ferro, F. Fazekas, L. Pantoni, D. Inzitari, and G. Waldemar, "Sparse decomposition and modeling of anatomical shape variation," *IEEE Trans. on Medical Imaging*, vol. 26, no. 12, pp. 1625–1635, 2007.
- [14] K. Y. E. Leung and J. G. Bosch, "Localized shape variations for classifying wall motion in echocardiograms," in *Proc. Medical Image Computing and Computer-Assisted Intervention - MICCAI 2007, LNCS 4791*. Springer-Verlag, 2007, pp. 52–59.
- [15] C. Jutten and A. Taleb, "Source separation: From dusk till dawn," in *Independent Component Analysis and Blind Signal Separation*, Helsinki, Finland, 2000.
- [16] A. Hyvärinen, J. Karhunen, and E. Oja, *Independent Component Analysis*. John Wiley & Sons, Inc., 2001.
- [17] A. J. Bell and T. J. Sejnowski, "An information-maximization approach to blind separation and blind deconvolution." *Neural Computation*, vol. 7, no. 6, pp. 1129–1159, 1995.
- [18] J.-F. Cardoso, "High-order contrasts for independent component analysis," *Neural Computation*, vol. 11, pp. 157–192, 1999.
- [19] M. Uzümcü, A. F. Frangi, M. Sonka, J. H. C. Reiber, and B. P. F. Lelieveldt, "Independent component analysis in statistical shape models," in *Proc. of SPIE Vol. 5032*, M. Sonka and J. Fitzpatrick, Eds., 2003, pp. 375–383.



- [20] J. Lotjonen, S. Kivisto, J. Koikkalainen, D. Smutek, and K. Lauerma, “Statistical shape model of atria, ventricles and epicardium from short- and long-axis MR images,” *Medical Image Analysis*, vol. 8, no. 3, pp. 371–386, 2004.
- [21] M. Hansen, F. Zhao, H. Zhang, N. Walker, A. Wahle, T. Scholz, and M. Sonka, “Detection of connective tissue disorders from 3d aortic mr images using independent component analysis,” *Computer Vision Approaches to Medical Image Analysis*, pp. 13–24, 2006.
- [22] J. Koikkalainen and J. Lotjonen, “Image segmentation with the combination of the PCA- and ICA-based modes of shape variation,” in *IEEE Intl. Symposium on Biomedical Imaging: Nano to Macro, 2004*, 2004, pp. 149–152 Vol. 1.
- [23] R. Larsen and K. B. Hilger, “Statistical shape analysis using non-Euclidean metrics,” *Medical Image Analysis*, vol. 7, no. 4, pp. 417–423, 2003.
- [24] A. Suinesiaputra, M. Üzümcü, A. F. Frangi, J. H. C. Reiber, and B. P. F. Lelieveldt, “Detecting regional abnormal cardiac contraction in short-axis MR images using independent component analysis,” in *Proc. Medical Image Computing and Computer-Assisted Intervention - MICCAI 2004, LNCS 3216*, C. Barillot, D. R. Haynor, and P. Hellier, Eds. Springer-Verlag, Oct 2004, pp. 737–744.
- [25] D. C. Adams, F. J. Rohlf, and D. E. Slice, “Geometric morphometrics: ten years of progress following the ‘revolution’,” *Italian Journal of Zoology*, vol. 71, pp. 5–16, 2004.
- [26] I. L. Dryden and K. V. Mardia, *Statistical Shape Analysis*. John Wiley & Sons, Inc., 1998.
- [27] F. L. Bookstein, “A statistical method for biological shape comparisons,” *Journal of Theoretical Biology*, vol. 107, pp. 475–520, 1984.
- [28] —, “Principal warps: Thin-plate splines and the decomposition of deformations,” *IEEE Trans. on Pattern Analysis and Machine Intelligence*, vol. 11, no. 6, pp. 567–585, 1989.
- [29] H. Stögbauer, R. G. Andrzejak, A. Kraskov, and P. Grassberger, “Reliability of ICA estimates with mutual information,” in *Independent Component Analysis and Blind Signal Separation, LNCS 3195*, C. Puntonet and A. Prieto, Eds. Granada, Spain: Springer-Verlag, 2004, pp. 209–216.
- [30] A. Cichocki, J. Karhunen, W. Kasprzak, and R. Vigário, “Neural networks for blind separation with unknown number of sources,” *Neurocomputing*, vol. 24, pp. 55–93, 1999.
- [31] S. J. Roberts, “Independent component analysis: Source assessment & separation, a bayesian approach,” *IEEE Proceedings - Vision, Image & Signal Processing*, vol. 3, no. 145, pp. 149–154, 1998.
- [32] J. Himberg, A. Hyvärinen, and F. Esposito, “Validating the independent components of neuroimaging time-series via clustering and visualization,” *NeuroImage*, vol. 22, no. 3, pp. 1214–1222, 2004.
- [33] B. Silverman, *Density Estimation for Statistics and Data Analysis*. London: Chapman and Hall, 1986.
- [34] M. P. Wand and M. C. Jones, *Kernel Smoothing*. Chapman and Hall, 1995.
- [35] A. Papoulis and S. U. Pillai, *Probability, random variables, and stochastic processes*, 4th ed. Boston: McGraw-Hill, 2002.

- [36] R. J. van der Geest, V. G. M. Buller, E. Janssen, H. J. Lamb, L. H. Baur, E. E. van der Wall, A. de Roos, and J. H. C. Reiber, "Comparison between manual and semiautomated analysis of left ventricular volume parameters from short-axis MR images," *Journal of Computer Assisted Tomography*, vol. 21, no. 5, pp. 756–765, 1997.
- [37] F. M. Baer, E. Voth, C. A. Schneider, P. Theissen, H. Schicha, and U. Sechtem, "Comparison of low-dose dobutamine gradient echo magnetic resonance imaging and positron emission tomography with [18F]fluorodeoxyglucose in patients with chronic coronary artery disease. A functional and morphological approach to the detection of residual myocardial viability." *Circulation*, vol. 91, no. 4, pp. 1006–1015, 1995.
- [38] M. H. Zweig and G. Campbell, "Receiver-operating characteristic (ROC) plots: a fundamental evaluation tool in clinical medicine." *Clinical Chemistry*, vol. 39, no. 4, pp. 561–577, 1993.
- [39] T. Sing, O. Sander, N. Beerenwinkel, and T. Lengauer, "ROCR: visualizing classifier performance in R," *Bioinformatics*, vol. 21, no. 20, pp. 3940–3941, 2005.
- [40] R. O. Duda, P. E. Hart, and D. G. Stork, *Pattern Classification*, 2nd ed. John Wiley & Sons, Inc., 2001.
- [41] E. W. Remme, K. F. Augenstein, A. A. Young, and P. J. Hunter, "Parameter distribution models for estimation of population based left ventricular deformation using sparse fiducial markers," *IEEE Trans. on Medical Imaging*, vol. 24, no. 3, pp. 381–388, Mar 2005.
- [42] A. Suinesiaputra, A. F. Frangi, H. J. Lamb, J. H. C. Reiber, and B. P. F. Lelieveldt, "Automatic prediction of myocardial contractility improvement in stress MRI using shape morphometrics with independent component analysis," in *Proc. of 19th Information Processing in Medical Imaging, LNCS 3565*, G. E. Christensen and M. Sonka, Eds. Springer-Verlag, 2005, pp. 321–332.
- [43] M. Uzümcü, R. J. van der Geest, S. Cory, J. H. C. Reiber, and B. P. F. Lelieveldt, "Time continuous tracking and segmentation of cardiovascular magnetic resonance images using multidimensional dynamic programming," *Investigative Radiology*, vol. 41, no. 1, pp. 52–62, Jan 2006.
- [44] H. C. van Assen, M. G. Danilouchkine, M. S. Dirksen, J. H. C. Reiber, and B. P. F. Lelieveldt, "A 3-D active shape model driven by fuzzy inference application to cardiac CT and MR," *IEEE Trans. on Information Technology in Biomedicine*, vol. 12, no. 5, pp. 595–605, 2008.

# 7

**AN AUTOMATED REGIONAL WALL MOTION  
ABNORMALITY DETECTION BY COMBINING REST AND  
STRESS CARDIAC MRI: CORRELATION WITH  
INFARCT TRANSMURALITY FROM  
CONTRAST-ENHANCED MRI**

## Abstract

**Objective:** To evaluate the performance of an automated regional wall motion abnormality (RWMA) detection method given the combination of rest and dobutamine-induced stress cardiac MR data and to correlate the automated RWMA results with infarct transmural assessments from contrast-enhanced MRI.

**Materials and Methods:** The automated RWMA method is built upon a statistical model of normokinetic myocardial contours. Forty-one rest cine-MRI of healthy volunteers were collected to build the model. Independent Component Analysis (ICA) was used to generate the probability distributions of normokinetic myocardium after several registration steps. Three normokinetic ICA models were built independently: base, mid-ventricular and apex. Twelve patients with the presence of myocardial infarction were included in the experiment. Their rest, dobutamine-induced stress and contrast-enhanced MR images in short-axis view were semi-automatically analyzed.

**Results:** A total of 192 myocardial segments were analyzed; 116 scar and 76 non-scar (normal) segments. For scar tissue detection, adding stress data significantly improved the performance compared to rest data only. Mean RWMA probability value differences between scar and non-scar regions with rest-stress data were wider and significant differences ( $p < 0.001$ , CI = 99.9%) were present in all ICA models. Combined sensitivity was 79% (base: 90%, mid: 79%, apex: 67%) and specificity was 80% (base: 83%, mid: 85%, apex: 70%). Correlated with CE-MRI, RWMA probability values decrease progressively as infarct transmural increases.

**Conclusion:** Combining rest and stress MR data using automated RWMA assessment method detects scar regions more accurately than using resting MRI alone. The presented automated abnormality detector correlates well with infarct transmural.

To know is to remember what you have seen.  
To see is to know without remembering.

*Benim Adım Kırmızı (My Name Is Red)*

ORHAN PAMUK

**C**ORONARY artery disease (CAD) has been a leading cause of death in Europe and North America and is responsible for 70% of congestive heart failure cases [1]. Although overall survival has improved, its treatment is a partial success [2, 3]. In patients with contractile reserve, where reversible myocardial dysfunction is present, treatment by coronary revascularization may lead to significant functional improvements.

In clinical practice, the assessment of dysfunctional but viable myocardium is indicated by the increase of systolic wall thickening from rest to stress. Reversible myocardial dysfunction can also be identified by contrast-enhanced MRI (CE-MRI) [4, 5]. CE-MRI allows imaging of myocardial infarction, in which scar tissues appear hyperenhanced, and the extent of infarction is the main predictor for functional outcome after revascularization. Head-to-head comparisons between rest-stress MR with infarct transmuralities from CE-MRI for predicting functional improvement have been performed and they have been proven to be correlated [6–8].

During the assessment of LV functional improvement, rest and dobutamine-induced stress cine-MR images are usually compared visually. Visual wall motion scoring is prone to observer variability. Observer experience clearly affects the quality of the assessment [9]. A computer-assisted diagnosis method for the assessment of myocardial contractile reserve can be helpful to reduce the variability.

A model-based automated RWMA method has been developed in [10] and it shows good correlation with systolic wall thickening and visual wall motion score from rest MRI. This paper focuses on the improvement of the automated RWMA detection through the integration of rest and stress MR data. Evaluation is performed against scar regions (infarct transmuralities) from CE-MRI.

## 7.1 Materials and Methods

### 7.1.1 Study design

Two study protocols were designed to collect control and patient groups. For the control group, forty-one healthy subjects were voluntarily enrolled in a cardiac MRI acquisition session. These subjects were part of a larger study to collect normal cardiac cine MR images from healthy population which was conducted between 2000–2004. Only short-axis view MR images were included in this study.

The patient group consisted of twelve patients suffering from chronic coronary artery disease. Each patient gave written informed consent to the study protocol that was approved by the local ethics committee. Mild to severe myocardial infarctions were present in these patients. The baseline characteristics of the patient and control groups are given

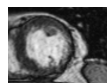


TABLE 7.1: Patient and Control Groups Statistics.<sup>a</sup>

	Patients	Controls
Subjects	12	41
Males/females	12/0	30/11
Ejection fraction (%)	44.85 (21.30) <sup>b</sup> 41.40 (17.23) <sup>c</sup>	67.91 (11.13)
Stroke volume (ml)	117.62 (73.87) <sup>b</sup> 82.44 (32.73) <sup>c</sup>	105.04 (32.16)

<sup>a</sup> All statistics are in average (standard deviation) form.

<sup>b</sup> Values from rest MR.

<sup>c</sup> Values from stress MR.

in Table 7.1. The mean ejection fraction in Table 7.1 indicates separation between the two groups.

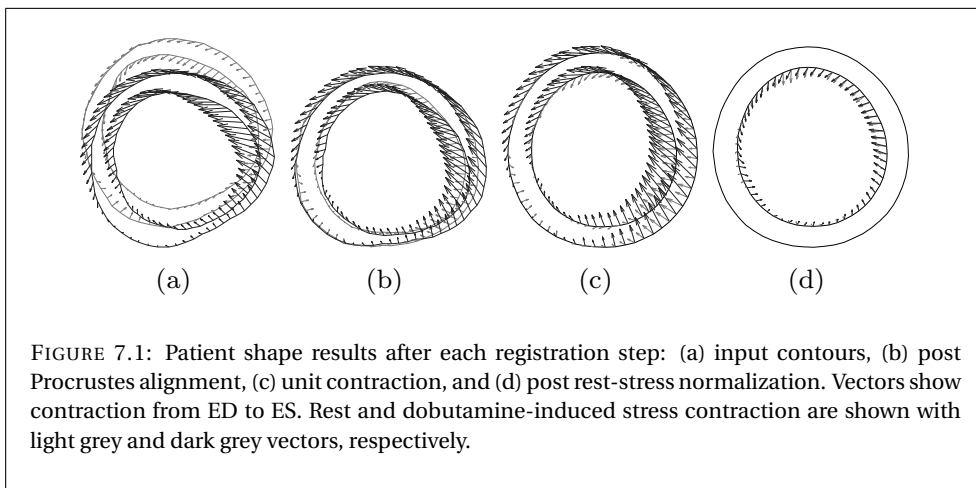
### 7.1.2 Data acquisition

Acquisition of baseline MR images was performed on 1.5T Gyroscan ACS-NT MRI Scanner (Philips Medical System, Best, the Netherlands) using a 5-element synergy coil during breath-holds and were gated to the electrocardiogram. The heart was imaged from apex to base with 10 to 12 imaging levels in the short-axis orientation. Typical imaging parameters are  $400 \times 400 \text{ mm}^2$  field-of-view, 10 mm slice thickness,  $256 \times 256$  image resolution and 1.5 mm pixel size.

Geometry settings in baseline scans were stored and repeated for low-dose dobutamine and contrast-enhanced acquisitions. The dobutamine-induced stress (DSMR) and CE-MRI acquisitions were only applied to the patient group. CE-MR images were acquired 15 minutes after a bolus injection of gadolinium diethylenetriamine pentaacetic acid (0.15 mmol/kg, Magnevist; Schering/Berlex, Berlin, Germany). Typical imaging parameters for dobutamine MRI were similar with the rest condition and also for the CE-MRI, except that the slice thickness for CE-MRI is smaller (5 mm), which gives CE-MRI more slice levels than rest MRI.

### 7.1.3 Slice selection

Three short-axis slice levels were visually determined in rest MRI by using particular anatomical landmarks. The basal level was defined at the short-axis slice level before the septal opening is visible. The apical level was set to the short-axis slice level where LV blood cavity is still visible in all cardiac phases. The mid-ventricular level was defined at the middle level between the basal and the apical slices. Their corresponding slice levels in DSMR and CE-MRI were automatically calculated based on 3D geometrical information obtained by using MR Analytical Software System (MASS, v5.0, Medis, Leiden, the Netherlands) [11]. Due to the smaller slice thickness of CE-MRI compared to cine-MRI, one or two CE-MR images can be associated to a slice level in cine-MRI. In case of two



CE-MR images were selected, the analysis of infarct transmuralty from these images were averaged.

#### 7.1.4 Myocardial contour delineation and segmental definition

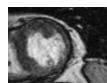
An expert delineated endo- and epicardial contours by using the MASS software [11]. Papillary muscles were considered as part of LV cavity and epicardial fat was excluded. Only contours at end-diastole (ED) and end-systole (ES) were taken for the automated analysis. The same software was used to delineate infarct regions on CE-MRI.

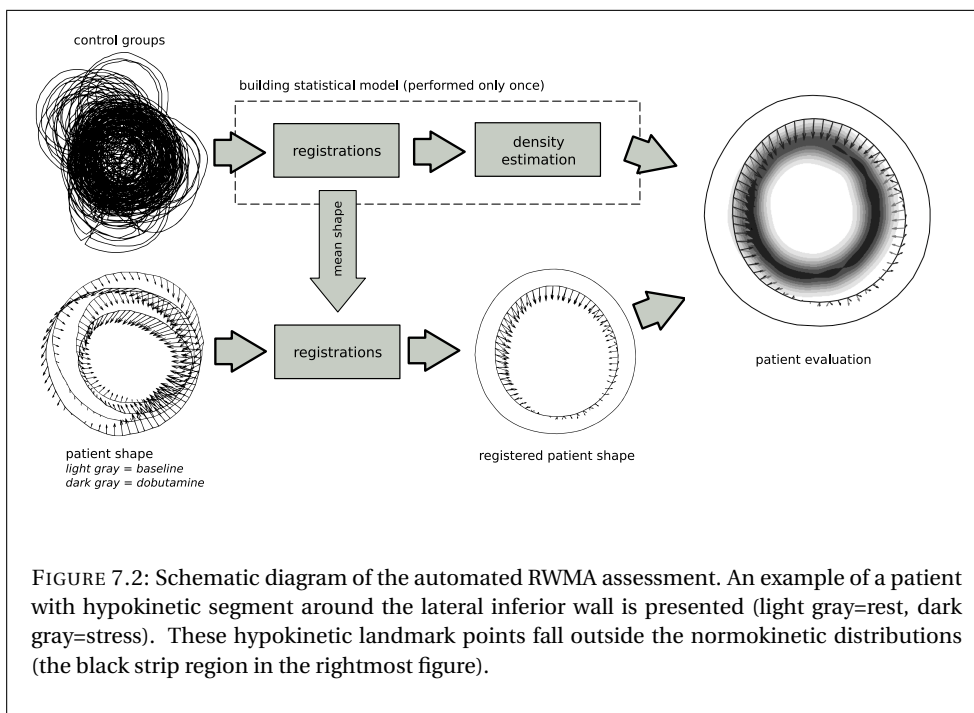
Between endo- and epicardial contours, the myocardium was divided into several segments during the validation. The 17-segment model conforming to American Heart Association [12] was applied. Only the 17th segment (the apical tip in long-axis view) was excluded in this study.

#### 7.1.5 Normokinetic myocardial shape models

A myocardial shape was defined as a sequential concatenation of endo- and epicardial landmark points, which were taken from both end-diastole (ED) and end-systole (ES) cardiac phases. Landmark points were determined by equi-angular homologous sampling starting from the inferior intersection between right and left ventricles clockwise. A normokinetic myocardial shape is a myocardial shape from the control group. To eliminate shape variations induced by cardiac position, orientation, size and movement between individual subjects, Procrustes alignment and thin-plate spline warping methods were applied [10].

The registration method in Chapter 6 was modified to allow a proper comparison between rest and stress myocardial shapes. Additional thin-plate spline warping was performed at the last registration step to remove epicardial shape variations at ES. Without





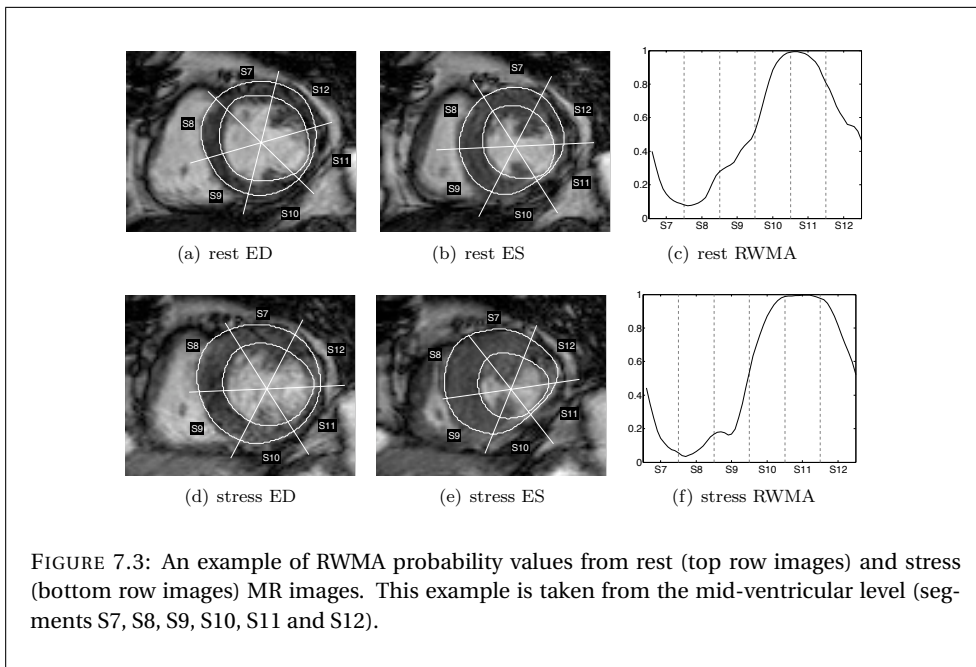
this step, shapes induced by dobutamine stress may produce false abnormal region from epicardial contour. Epicardial landmark points at ES might fall outside the distribution of control points. An example of step-by-step registration results are shown in Figure 7.1. After the last registration step, shape variations are only present in the es-endo contour.

### 7.1.6 Building RWMA probability density functions

The processes of building the statistical shape model and estimating RWMA density functions were equivalent to the methods reported earlier in Chapter 6. Independent Component Analysis (ICA) was applied to decompose local shape variations. Probability density functions of control group coefficient values were constructed for each independent component. Based on the statistical independency assumption of ICA, the density functions were propagated from the independent component domain to the shape domain. This allows direct landmark point evaluation of a patient shape without projecting it first into the ICA model. The schematic diagram of the RWMA assessment is shown in Figure 7.2.

### 7.1.7 RWMA evaluation

RWMA evaluation was performed by aligning a patient myocardial shape with the ICA model of the control group and calculating the probability values from the aligned shape



with respect to the RWMA density functions. When the RWMA probability values of two myocardial shapes from the same patient were evaluated, they will produce similar profile lines. This behavior was observed in the rest and stress shapes of the same patient (see Figure 7.3(c) and Figure 7.3(f) for an example). Hypokinetic regions that do not increase its function at stress will be visible due to the last registration step that normalizes myocardial shape at stress. In the example in Figure 7.3, non-improved hypokinetic regions are present in segment S10 and S11. These segments show small increase of RWMA probability values from rest to stress.

The combination of rest and stress data can therefore be used to detect improved and non-improved segments in terms of RWMA probability value changes. Since the ICA model was built from baseline control groups, the myocardial shape at rest can be used as the baseline to quantify the changes.

Let  $N$  be the total number of landmark points from concatenating epicardial and endocardial contours after the equi-angular sampling. Each landmark point will have its own RWMA density function,  $i = 1, \dots, N$ . Let  $\rho_r^{(i)}$  and  $\rho_s^{(i)}$  be the RWMA probability values of the  $i$ th landmark point for rest and stress, respectively. The magnitude of RWMA probability value changes from rest to stress can be formulated as follows

$$\Delta P^{(i)} = \frac{\rho_r^{(i)} - \rho_s^{(i)}}{1 + \max\{\rho_r^{(i)}, \rho_s^{(i)}\}} \quad (7.1)$$

A negative value of  $\Delta P^{(i)}$  indicates no wall motion improvement and a positive  $\Delta P^{(i)}$

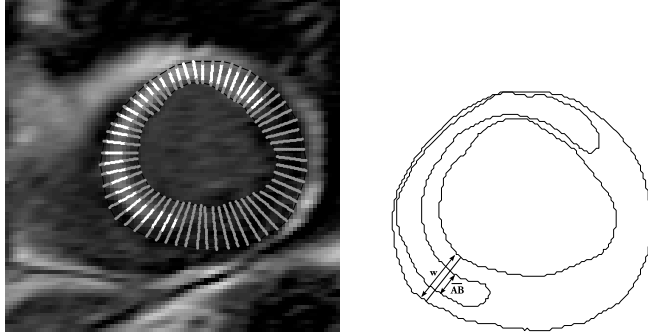


FIGURE 7.4: Transmurality chord lines. In the left figure, the white segments are the transmural extent of the chord lines (gray lines).

value shows a possible improvement of the myocardium towards normokinetic motion. The RWMA probability value changes from rest to stress is given by

$$P^{(i)} = (1 - \rho_r^{(i)}) + \Delta P^{(i)} \quad (7.2)$$

### 7.1.8 Transmural extent

Infarct transmural extent was calculated by creating a series of chord lines (see Figure 7.4). The percentage of transmural extent is defined as

$$TE = \frac{\overline{AB}}{w} \times 100\% \quad (7.3)$$

where  $\overline{AB}$  is the transmural length over the chord line and  $w$  is the wall thickness.

During the experiment, TE values were averaged on each myocardial segment and graded into the following groups: absence of hyperenhancement, transmural extent of less than 25%, transmural extent of between 25%–50%, between 50%–75%, and transmural extent more than 75%.

### 7.1.9 Statistical analysis

Statistical shape modeling, registrations, and patient evaluation were implemented in Matlab (Matlab v7.0, The Mathworks, Natick, MA, USA). The Matlab implementation of FastICA method to generate ICA components was applied [13]. Receiver operating characteristics (ROC) graph was produced by ROCR library package (ROCR v1.0.2) [14]. The optimal cut-off value from the ROC curve is defined by minimizing  $(1 - \text{sensitivity})^2 + (1 - \text{specificity})^2$ . Standard sensitivity and specificity measurements were used to show the

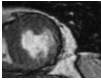


TABLE 7.2: Segmental RWMA probability values.

segments	samples		rest only		rest-stress	
	$\mathfrak{S}'$	$\mathfrak{S}$	$\hat{P}_r \in \mathfrak{S}'$	$\hat{P}_r \in \mathfrak{S}$	$\hat{P}_s \in \mathfrak{S}'$	$\hat{P}_s \in \mathfrak{S}$
basal anterior	9	3	0.25 (0.14)	0.43 (0.15)	0.29 (0.10)	0.5 (0.23)
basal anteroseptal	11	1	0.33 (0.15)	*	0.32 (0.15)	*
basal inferoseptal	7	5	0.15 (0.12)	0.39 (0.13)	0.41 (0.16)	0.46 (0.26)
basal inferior	4	8	0.34 (0.13)	0.38 (0.13)	0.27 (0.07)	0.74 (0.20)
basal inferolateral	3	9	0.36 (0.21)	0.57 (0.18)	0.24 (0.10)	0.81 (0.15)
basal anterolateral	4	8	0.39 (0.20)	0.44 (0.12)	0.27 (0.20)	0.57 (0.26)
<b>base</b>	<b>38</b>	<b>34</b>	<b>0.30 (0.16)</b>	<b>0.46 (0.14)</b>	<b>0.30 (0.13)</b>	<b>0.62 (0.22)</b>
mid anterior	6	6	0.39 (0.29)	0.48 (0.07)	0.31 (0.10)	0.62 (0.20)
mid anteroseptal	5	7	0.39 (0.39)	0.53 (0.11)	0.27 (0.20)	0.71 (0.18)
mid inferoseptal	4	8	0.33 (0.16)	0.44 (0.14)	0.42 (0.22)	0.54 (0.15)
mid inferior	5	7	0.55 (0.16)	0.43 (0.19)	0.32 (0.20)	0.82 (0.12)
mid inferolateral	3	9	0.48 (0.13)	0.62 (0.18)	0.27 (0.15)	0.81 (0.17)
mid anterolateral	3	9	0.74 (0.13)	0.44 (0.17)	0.39 (0.26)	0.63 (0.16)
<b>middle</b>	<b>26</b>	<b>46</b>	<b>0.48 (0.21)</b>	<b>0.49 (0.14)</b>	<b>0.33 (0.19)</b>	<b>0.69 (0.16)</b>
apical anterior	5	7	0.68 (0.22)	0.66 (0.17)	0.47 (0.25)	0.82 (0.16)
apical septal	2	10	0.68 (0.09)	0.72 (0.17)	0.44 (0.24)	0.61 (0.20)
apical inferior	2	10	0.81 (0.17)	0.75 (0.15)	0.68 (0.01)	0.80 (0.13)
apical lateral	3	9	0.77 (0.05)	0.67 (0.21)	0.66 (0.10)	0.88 (0.10)
<b>apex</b>	<b>12</b>	<b>36</b>	<b>0.74 (0.13)</b>	<b>0.70 (0.17)</b>	<b>0.56 (0.15)</b>	<b>0.78 (0.15)</b>

$\mathfrak{S}'$  is non-scar segments and  $\mathfrak{S}$  is scar segments.  $\hat{P}_r \in \mathfrak{S}'$  and  $\hat{P}_r \in \mathfrak{S}$  are the mean RWMA probability values at rest for non-scar and scar segments, respectively.  $\hat{P}_s \in \mathfrak{S}'$  and  $\hat{P}_s \in \mathfrak{S}$  are the mean RWMA probability values at stress for non-scar and scar segments, respectively. All values are in mean (standard deviation) format. The symbol \* indicates non-available statistical data because the number of samples for that particular case is not enough. Segments are labeled as defined by American Heart Association standardization for myocardial segments [12].

method's performance [15]. The significant differences of RWMA probability values between scar and non-scar segments were tested by unpaired two-tailed  $t$ -tests with 99.9% confidence interval.  $P$ -values  $< 0.001$  were considered significant.

## 7.2 Results

### 7.2.1 Rest versus rest-stress data

Two evaluations for scar tissue detection were compared: RWMA probability values from rest MRI only and RWMA probability values from the combination of rest and stress MRI. A scar tissue is a region where transmural extent exceeds 1%. The results are shown in Table 7.2.

The mean differences between scar and non-scar segments for rest-stress data in Table 7.2 are significantly larger than for rest data only. This indicates a better separation of scar tissues by the combination of rest and stress data. The unpaired  $t$ -tests resulted in significant differences of mean RWMA probability values between scar and non-scar

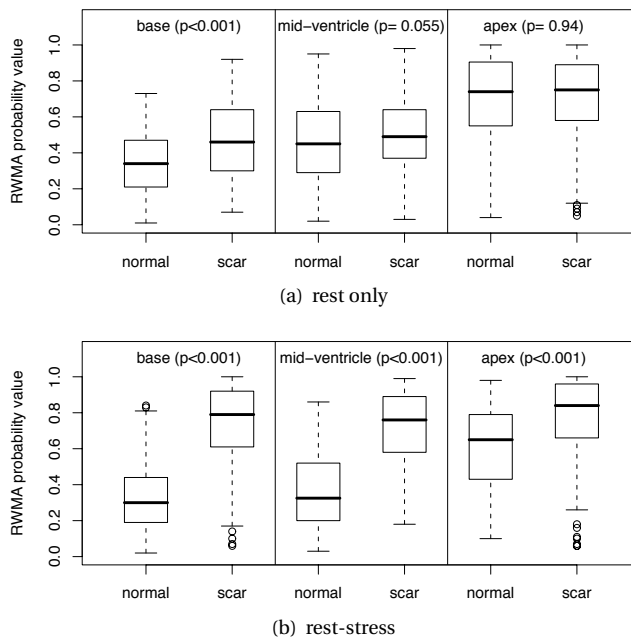


FIGURE 7.5: Distributions of RWMA probability values from scar and non-scar (normal) segments for each slice model, presented by box-and-whisker plots. Unpaired t-tests were performed with 99% confidence level to get the  $p$ -values.

segments in all three slice levels ( $p < 0.001$  for base, mid-ventricular and apex) when rest and stress data were combined. If only rest data were used, then only the basal model showed significant difference ( $p < 0.001$ ); the mid-ventricular model resulted  $p = 0.06$  and apical model was  $p = 0.94$ . These findings are graphically presented by box plots in Figure 7.5. Based on this observation, the remaining experimental studies in this paper used only the combination of rest and stress data.

## 7.2.2 Scar tissue detection

Receiver operating characteristics (ROC) curve to detect scar tissue by using rest and stress data is given in Figure 7.6. The area under the ROC curve was 0.88. Sensitivity and specificity of the method were 79% and 80%, respectively. These were combined from basal, mid-ventricular and apical models. The sensitivity values for each model were 90% (base), 79% (mid-ventricular) and 67% (apex), while for specificity values were 83% (base), 85% (mid-ventricular) and 70% (apex).

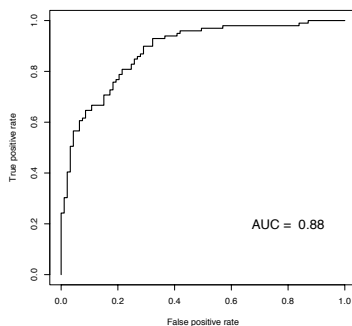


FIGURE 7.6: ROC curve of the method performance to detect hyperenhanced segments.

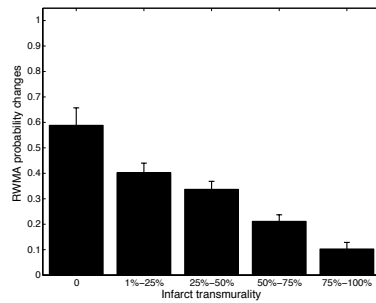


FIGURE 7.7: Distributions of RWMA probability values grouped by infarct transmuralities. Error bars indicate standard error values.

### 7.2.3 Correlation with infarct transmuralities

From the total of 192 segments, 116 (60.4%) segments showed hyperenhancement. Out of these scar segments, 32 (16.7%) segments had less than 25% transmuralities, 40 (20.8%) segments with 25%–50% transmuralities and 32 (16.7%) segments with 50%–75% transmuralities. Severe infarct transmuralities of over 75% was observed in 12 (6.2%) segments.

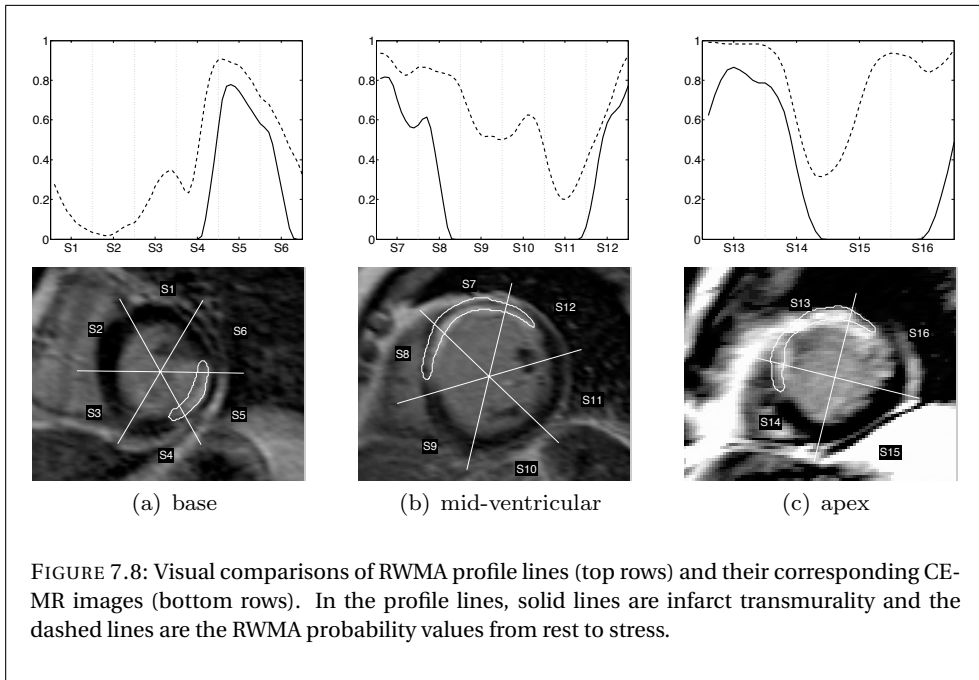
Distributions of RWMA probability values over each of the scarring score groups are shown in Figure 7.7. It shows that the RWMA probability values decrease progressively as infarct transmuralities increase. There is a clear separation between transmural and non-transmural regions. This shows that the automated rest-stress RWMA assessment method correlates well with the infarct transmuralities from CE-MRI. A visual example of this finding is illustrated in Figure 7.8.

## 7.3 Discussion

Two main objectives were addressed in this chapter: (1) to evaluate the performance of the automated RWMA detection method when stress and rest data are combined, and (2) to correlate the RWMA probability changes estimated from the automated method with infarct transmuralities from CE-MR images. From the result section, the RWMA probability values from the combined rest and stress data has proven to produce a significant improvement in distinguishing scar regions compared to the use of rest data only. The separation between scar and non-scar regions widened considerably when stress data was included.

On the detection of scar regions, the performance of the automated method with the combination of rest and stress data was relatively high. The area under RWMA probability



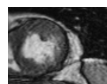


value curve was 0.88 (see Figure 7.6), which proves the method's capability to detect scar regions. Significant differences of mean RWMA probability values between scar and non-scar regions were demonstrated in all models.

Correlated with the infarct transmurality, the automated detection method produced decreasing RWMA probability values as the transmural extent increases. In Kim et. al. [4] the likelihood of improvement in dysfunctional segments after revascularization increases when the transmural extent decreases. This means that the estimated RWMA probability values may explain the same likelihood of contractile reserve.

Currently, myocardial contours for both control and patient groups, including the hyperenhanced boundaries, were drawn manually by an expert. This experimental study was conducted to demonstrate the proof of concept of the automated RWMA assessment for the rest and stress data. However, providing manual contours is prone to subjectivity and a tedious task. Especially for the apical regions, drawing endocardial borders is problematic because of the low contrast at the later systolic phases. Endocardial borders were sometimes almost invisible at end-systole. As a result, the apical model yielded the lowest score in detecting scar regions (67% sensitivity and 70% specificity) compared to basal and mid-ventricular models. This raises the necessity to apply an objective segmentation method for myocardium. Statistical-based segmentation methods that incorporate temporal information, e.g. [16–18], can be applied in this case to solve this problem.

The main limitation of this study is the lack of follow up data after revascularization to assess functional recovery completely. The current validation used infarct transmu-



rality as the ground truth, but CE-MRI also possesses significant problems for viability assessment [19]. Therefore this study does not evaluate the method's capability to assess myocardial viability, but the proposed method shows good correlation with infarct transmural. Additional pre- and post-treatment patient data is needed to further explore the capability of the proposed method to quantify regional LV functional improvement.

The current statistical model is trained from ED and ES phases only. The results show that building the statistical model from these two phases is enough to capture the kinetics of heart motion. However, a higher temporal resolution may improve the performance of the method, but at the expense of more contour drawing.

In conclusion, we have presented an automatic quantification method of RWMA analysis that combines information from resting and stress MR. Validated against CE-MRI, the automated method behaves as expected, i.e., it decreases when transmural extent increases. Hence, the proposed method correlates well with CE-MRI and therefore is a promising diagnostic tool to automatically assess RWMA from cardiac MR images.

## 7.4 References

- [1] H. Mahrholdt, I. Klem, and U. Sechtem, "Cardiovascular MRI for detection of myocardial viability and ischaemia," *Heart*, vol. 93, no. 1, pp. 122–129, 2007.
- [2] T. E. Owan, D. O. Hodge, R. M. Herges, S. J. Jacobsen, V. L. Roger, and M. M. Redfield, "Trends in prevalence and outcome of heart failure with preserved ejection fraction," *N Engl J Med*, vol. 355, no. 3, pp. 251–259, Jul 2006.
- [3] P. G. Camici, S. K. Prasad, and O. E. Rimoldi, "Stunning, hibernation, and assessment of myocardial viability," *Circulation*, vol. 117, no. 1, pp. 103–114, Jan 2008.
- [4] R. J. Kim, E. Wu, A. Rafael, E. L. Chen, M. A. Parker, O. Simonetti, F. J. Klocke, R. O. Bonow, and R. M. Judd, "The use of contrast-enhanced magnetic resonance imaging to identify reversible myocardial dysfunction," *N Engl J Med*, vol. 343, no. 20, pp. 1445–1453, Nov 2000.
- [5] A. Saraste, S. Nekolla, and M. Schwaiger, "Contrast-enhanced magnetic resonance imaging in the assessment of myocardial infarction and viability," *J Nucl Cardiol*, vol. 15, no. 1, pp. 105–117, Jan-Feb 2008.
- [6] M. Gutberlet, M. Frohlich, S. Mehl, H. Amthauer, H. Hausmann, R. Meyer, H. Siniawski, J. Ruf, M. Plotkin, T. Denecke, B. Schnackenburg, R. Hetzer, and R. Felix, "Myocardial viability assessment in patients with highly impaired left ventricular function: Comparison of delayed enhancement, dobutamine stress MRI, end-diastolic wall thickness, and TI201-SPECT with functional recovery after revascularization," *Eur Radiol*, vol. 15, no. 5, pp. 872–880, May 2005.
- [7] T. A. M. Kaandorp, J. J. Bax, J. D. Schuijf, E. P. Viergever, E. E. van Der Wall, A. de Roos, and H. J. Lamb, "Head-to-head comparison between contrast-enhanced magnetic resonance imaging and dobutamine magnetic resonance imaging in men with ischemic cardiomyopathy," *Am J Cardiol*, vol. 93, no. 12, pp. 1461–4, Jun 2004.
- [8] E. Wellnhofer, A. Olariu, C. Klein, M. Grafe, A. Wahl, E. Fleck, and E. Nagel, "Magnetic resonance low-dose dobutamine test is superior to SCAR quantification for the prediction of functional recovery," *Circulation*, vol. 109, no. 18, pp. 2172–2174, May 2004.

- [9] I. Paetsch, C. Jahnke, V. A. Ferrari, F. E. Rademakers, P. A. Pellikka, W. G. Hundley, D. Poldermans, J. J. Bax, K. Wegscheider, E. Fleck, and E. Nagel, "Determination of interobserver variability for identifying inducible left ventricular wall motion abnormalities during dobutamine stress magnetic resonance imaging," *Eur Heart J*, vol. 27, no. 12, pp. 1459–1464, Jun 2006.
- [10] A. Suinesiaputra, A. F. Frangi, T. A. M. Kaandorp, H. J. Lamb, J. J. Bax, J. H. C. Reiber, and B. P. F. Lelieveldt, "Automated detection of regional wall motion abnormalities based on a statistical model applied to multislice short-axis cardiac MR images," *IEEE Trans Med Imaging*, vol. 28, no. 4, pp. 595–607, Apr 2009.
- [11] R. J. van der Geest, V. G. Buller, E. Jansen, H. J. Lamb, L. H. Baur, E. E. van der Wall, A. de Roos, and J. H. Reiber, "Comparison between manual and semiautomated analysis of left ventricular volume parameters from short-axis MR images," *J Comput Assist Tomogr*, vol. 21, no. 5, pp. 756–765, Sep-Oct 1997.
- [12] M. D. Cerqueira, N. J. Weissman, V. Dilsizian, A. K. Jacobs, S. Kaul, W. K. Laskey, D. J. Pennell, J. A. Rumberger, T. Ryan, and M. S. Verani, "Standardized myocardial segmentation and nomenclature for tomographic imaging of the heart: a statement for healthcare professionals from the Cardiac Imaging Committee of the Council on Clinical Cardiology of the American Heart Association," *Circulation*, vol. 105, no. 4, pp. 539–542, 2002.
- [13] A. Hyvärinen and E. Oja, "Independent component analysis: algorithms and applications," *Neural Networks*, vol. 13, pp. 411–430, June 2000.
- [14] T. Sing, O. Sander, N. Beerenwinkel, and T. Lengauer, "ROCR: visualizing classifier performance in R," *Bioinformatics*, vol. 21, no. 20, pp. 3940–3941, 2005.
- [15] T. A. Lasko, J. G. Bhagwat, K. H. Zou, and L. Ohno-Machado, "The use of receiver operating characteristic curves in biomedical informatics," *J Biomed Inform*, vol. 38, no. 5, pp. 404–415, 2005.
- [16] A. Andreopoulos and J. K. Tsotsos, "Efficient and generalizable statistical models of shape and appearance for analysis of cardiac MRI," *Medical Image Analysis*, vol. 12, no. 3, pp. 335–357, JUN 2008.
- [17] R. Lapp, M. Lorenzo-Valdes, and D. Rueckert, "3D/4D cardiac segmentation using active appearance models, non-rigid registration, and the insight toolkit," in *Medical Image Computing and Computer-Assisted Intervention - MICCAI 2004, Part 1, Proceedings*, ser. Lecture Notes in Computer Science, C. Barillot, D. Haynor, and P. Hellier, Eds., vol. 3216. Springer, 2004, pp. 419–426.
- [18] S. C. Mitchell, J. G. Bosch, B. P. F. Lelieveldt, R. J. van der Geest, J. H. C. Reiber, and M. Sonka, "3-D active appearance models: segmentation of cardiac MR and ultrasound images," *IEEE Trans Med Imaging*, vol. 21, no. 9, pp. 1167–1178, Sep 2002.
- [19] S. D. Roes, T. A. M. Kaandorp, N. A. Marsan, J. J. M. Westenberg, P. Dibbets-Schneider, M. P. Stokkel, H. J. Lamb, E. E. van der Wall, A. de Roos, and J. J. Bax, "Agreement and disagreement between contrast-enhanced magnetic resonance imaging and nuclear imaging for assessment of myocardial viability," *Eur J Nucl Med Mol Imaging*, vol. 36, no. 4, pp. 594–601, Apr 2009.

# 8

## SUMMARY



Columbus is not the only person who has discovered a new continent. So too have I.

---

*Anak Semua Bangsa (Child of All Nations)*  
PRAMOEDYA ANANTA TOER

## 8.1 Myocardial wall motion modeling

**T**HE first objective of this thesis was to explore possible shape parameterizations to model normal myocardial contraction. Two different approaches to extract wall motion patterns were presented in this thesis. Chapter 2 presented a study towards direct velocity vector field quantification from tagged MRI, while in Chapter 3, myocardial contractility patterns were extracted from landmark-based endocardial and epicardial contours.

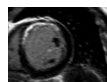
MR tagging allows full inspection of wall motion, not only for myocardial borders, but for all pixels inside the myocardium. The spatially induced tag patterns in MR tagging follow the deformation of the heart, allowing quantification of myocardial deformation fields. Dense velocity vector fields of myocardium can be extracted automatically by using the first order density multiscale optic flow method. This dense optic flow framework does not assume constant pixel intensity, but a constant integral of pixel intensities over a region (local “intensity mass” preservation). It is therefore relatively robust with respect to the problem of decaying intensity of the tag patterns over the cardiac cycle.

In Chapter 2, the proposed dense optic flow method was compared to velocity-encoded (VEC) MRI. Experimental results show strong correlation in the radial direction, but not in the circumferential direction. The correlation is also stronger for velocity vectors in the systolic phase compared to the diastolic phase. Further improvements are still required for this method to overcome this problem, for instance by estimating the optic flow field in the frequency domain instead of in the spatial domain [1, 2].

MR tagging is useful for analyzing local myocardial contraction. In clinical practice however, MR tagging is not included in many routine diagnostic imaging protocols for ischemic heart disease. For this reason, we shifted the research focus to the extraction of myocardial contractility patterns from cine MRI.

Myocardial contours from cine MRI, which include epicardial and endocardial borders, are the main prerequisites for analyzing regional and global LV function. Ejection fraction, wall thickening, wall thinning and stroke volume, to name a few, use both contours from the end-diastolic (ED) and end-systolic (ES) phase. To parameterize these contractility patterns in the remainder of this thesis, endo- and epicardial contours were combined serially to form a *myocardial contraction shape*. Equi-angular landmark points were sampled to establish anatomical point-to-point correspondence of shapes between subjects.

In Chapter 3, we investigated the potential of this myocardial contraction shape definition to distinguish between 42 normal and 47 pathological (ischemic) subjects. Two linear generative models were used to decompose the shapes, i.e., Principal Component



Analysis (PCA) and Independent Component Analysis (ICA). In terms of modes of shape variation, PCA produced global shape variations while ICA generated more local shape variations. In terms of discriminating between normal and pathological subjects, only the first component of the PCA model was sufficient to separate the two groups. For the ICA model, 27 out of 35 (77%) components were required to achieve the same discrimination performance.

From this, we concluded that PCA is suitable for shape decomposition because it can produce a compact model. For classification purposes, the PCA decomposition can only discriminate two groups globally. There is no geometrical interpretation of the classification result that can be deduced from the discriminating principal components. ICA may not be suitable to produce a compact representation of a shape model, because all independent components contribute evenly to the model. However, independent components cannot only discriminate shapes between two groups, but also they can locate the position of the shape differences. This locality property makes ICA more suitable than PCA for the detection and localization of regional wall motion abnormalities. Based on this observation, ICA was used in the remaining chapters as the statistical tool of choice to extract local shape features from myocardial shapes.

## **8.2 Automated evaluation of regional wall motion abnormalities**

The second objective of this thesis was to define a good classifier to detect, to locate and to quantify regional wall motion abnormalities (RWMA). Since an independent component intrinsically contains local geometry of where the component lies in the shape domain, each localized shape component is centered around a “central” landmark point and detection of abnormal regions can be performed by selecting the “abnormal components”. This study was given in Chapter 4. First, a patient shape was projected onto the ICA model to reveal its independent component coefficients. Probability density functions of the healthy subject coefficient values were estimated by assuming normal distributions. An abnormal component was defined as a component with a coefficient value which lies outside the normal distribution (beyond  $\pm 3$  times standard deviation) of coefficient values of a healthy population.

In Chapter 4, a qualitative validation of the automated RWMA evaluation with abnormal independent components was performed on six infarct patients. These abnormal components were mapped onto myocardial regions by using a mixture of Gaussian functions to color-code RWMA values on cine MRI. A comparison was made with the corresponding CE-MRI. All of the six patients showed good visual correlation between the position of segments with high RWMA values and the hyperenhanced (scarred) segments.

The study in Chapter 4 demonstrated that ICA-based RWMA classifiers are capable of detecting and locating RWMA. In Chapter 6, quantification of RWMA was formulated based on probability values and the process of mapping the abnormal components to the shape domain was refined. The probability density functions of healthy coefficient values were propagated into probability density functions of landmark points. Such propagation is allowed because of the statistical independence property of ICA. This propagation re-



sults in a probability density function for each landmark point that is estimated based on all components, integrating contextual information from neighboring landmarks.

Quantitative validations in Chapter 6 were performed with cross referencing experiments. A comparison with visual wall motion scoring (VWMS) was made by using wall thickening as the reference; in that case the automated RWMA method performed significantly better. If VWMS was used as the reference standard, then the automated RWMA method performance was slightly better than wall thickening. This study demonstrated the capability of the ICA model for detecting segments with abnormal regional wall motion.

### 8.3 Automated prediction of functional improvement

The last objective of this thesis was to correlate the automated RWMA evaluation method with indicators that may predict functional improvement. Hence, contours from dobutamine stress MR (DSMR) images were used and their RWMA values were compared with RWMA from resting (baseline) MRI. Research hypothesis was that when two myocardial contraction shapes from rest and stress MR from the same patient are evaluated with the ICA-based RWMA method, then the differences in RWMA values could be indicative for myocardial viability.

The pilot study described in Chapter 5 compared the probability values derived from rest and stress contours of independent components that were classified as abnormal. A qualitative comparison in six patients suffering from myocardial ischemia revealed that when contraction from rest to stress improved, the automatically estimated RWMA probability values of abnormal components decreased from rest to stress. An interesting observation was that the automated method detected an improved wall thickening from rest to stress as abnormal for a dyskinetic segment. This fact shows that the automated RWMA method not only incorporates information on wall thickening, but also on wall motion.

In Chapter 7, the methodology was further improved to allow proper comparison of myocardial contraction shapes at stress with baseline (rest) shapes. After rigid (Procrustes) and non-rigid (thin-plate splines) registrations, another non-rigid registration (also with thin-plate splines) was applied to eliminate shape variations at epicardial contours. Hence, only relative motion from endocardial contours with respect to epicardium was modeled. Without this additional registration, false positive samples could occur because strong myocardial contractions at stress could be classified as abnormal.

To quantitatively validate the method for predicting myocardial viability, longitudinal pre- and post-revascularization data is required. However, such data was not available. In Chapter 7, the combination of rest and stress RWMA values was therefore correlated against infarct transmuralities from CE-MRI, because CE-MRI is also used to predict functional recovery after revascularization [3]. The automated RWMA probability values achieved strong positive correlation with infarct transmuralities in all slice levels. RWMA probability values from the combined rest-stress data progressively decrease as infarct transmuralities increase. The method shows high accuracy in the detection of myocardial segments with scar tissue, as confirmed in a validation against CE-MRI.

## 8.4 Future directions

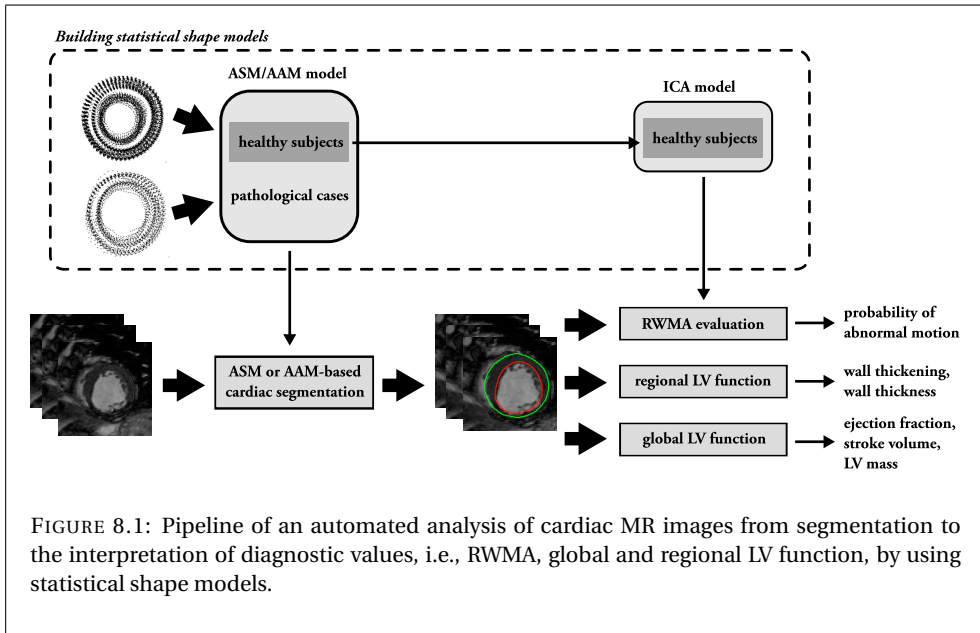


FIGURE 8.1: Pipeline of an automated analysis of cardiac MR images from segmentation to the interpretation of diagnostic values, i.e., RWMA, global and regional LV function, by using statistical shape models.

This thesis presented a number of steps towards the development of automated wall motion analysis to assist in the diagnosis of ischemic heart disease. Further improvements and extensions can be made in several ways. These include the extension of the shape model into a three-dimensional surface of the left ventricle, the inclusion of more temporal samples, and a validation against pre and post revascularization data to properly assess the method's performance for classifying viable tissues.

The presented automated method would fit perfectly at the end of a cardiac MR image processing pipeline for cardiac MRI decision support. Currently, the studies reported in this thesis used manually drawn contours as input. In the future, these myocardial contours could be detected from an automated segmentation method, regardless of the underlying segmentation algorithm. It would be more appropriate to connect components in the pipeline with statistical shape models. For instance, morphometrics based segmentation methods, such as Active Shape Models [4–6] and Active Appearance Models [7, 8], could be used in this pipeline. The ASM/AAM parameters of the segmentation can be used for building a normokinetic model. Figure 8.1 displays how a fully automatic pipeline of cardiac MR analysis with statistical shape models could be realized in this way.

The CAD methods described in this thesis are based on contours from cardiac MRI, but the underlying algorithm does not depend on the imaging modality. The presented method could therefore be used for the diagnosis of RWMA in e.g. echocardiography, but this will require further experimental studies.

Diagnostic results from the automated RWMA evaluation method could also be combined with other diagnostic imaging modalities, for example in a combination of cine MRI

and MR perfusion imaging, FDG-PET imaging, gated SPECT imaging and/or contrast-based images (CE-MRI or MCE). Also information on myocardial deformation could be derived from MR tagging, strain-encoded MR, velocity-encoded MRI or color Doppler echocardiograms. The integration of information on contraction, deformation and perfusion may be a next step towards a more comprehensive CAD method for ischemic heart disease.

## 8.5 References

- [1] L. Florack, H. van Assen, and A. Suinesiaputra, "Dense multiscale motion extraction from cardiac cine MR tagging using HARP technology," in *IEEE 11th International Conference on Computer Vision, ICCV*, 2007, pp. 1–8.
- [2] H. C. van Assen, L. M. Florack, A. Suinesiaputra, J. J. Westenberg, and B. M. ter Haar Romeny, "Purely evidence based multiscale cardiac tracking using optic flow," in *Proc. Computational Biomechanics for Medicine II. A MICCAI 2007 Workshop*, 2007.
- [3] T. A. M. Kaandorp, J. J. Bax, J. D. Schuijf, E. P. Viergever, E. E. van Der Wall, A. de Roos, and H. J. Lamb, "Head-to-head comparison between contrast-enhanced magnetic resonance imaging and dobutamine magnetic resonance imaging in men with ischemic cardiomyopathy," *Am J Cardiol*, vol. 93, no. 12, pp. 1461–4, Jun 2004.
- [4] H. van Assen, M. Danilouchkine, A. Frangi, S. Ordas, J. Westenberg, J. Reiber, and B. Lelieveldt, "SPASM: A 3D-ASM for segmentation of sparse and arbitrarily oriented cardiac MRI data," *Medical Image Analysis*, vol. 10, no. 2, pp. 286–303, APR 2006.
- [5] H. C. van Assen, M. G. Danilouchkine, M. S. Dirksen, J. H. C. Reiber, and B. P. F. Lelieveldt, "A 3-D active shape model driven by fuzzy inference: application to cardiac CT and MR," *IEEE Trans Inf Technol Biomed*, vol. 12, no. 5, pp. 595–605, Sep 2008.
- [6] M. Uzumcu, R. J. van der Geest, M. Sonka, H. J. Lamb, J. H. C. Reiber, and B. P. F. Lelieveldt, "Multiview active appearance models for simultaneous segmentation of cardiac 2- and 4-chamber long-axis magnetic resonance images," *Invest Radiol*, vol. 40, no. 4, pp. 195–203, Apr 2005.
- [7] S. C. Mitchell, J. G. Bosch, B. P. F. Lelieveldt, R. J. van der Geest, J. H. C. Reiber, and M. Sonka, "3-D active appearance models: segmentation of cardiac MR and ultrasound images," *IEEE Trans Med Imaging*, vol. 21, no. 9, pp. 1167–1178, Sep 2002.
- [8] E. Oost, G. Koning, M. Sonka, P. V. Oemrawsingh, J. H. C. Reiber, and B. P. F. Lelieveldt, "Automated contour detection in X-ray left ventricular angiograms using multiview active appearance models and dynamic programming," *IEEE Trans Med Imaging*, vol. 25, no. 9, pp. 1158–1171, Sep 2006.





# 9

**SAMENVATTING**



## 9.1 Statistische modellering van de wandbeweging van het linkerventrikel

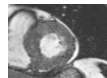
**D**IT proefschrift verkent als eerste twee mogelijke parametrisaties om normale wandbeweging van het contraherende myocard wiskundig te beschrijven. Hoofdstuk 2 beschrijft een pilotstudie naar directe kwantificatie van wandbeweging op basis van MR tagging technieken, terwijl in Hoofdstuk 3, vormkenmerken over myocardcontractie worden afgeleid uit endo- en epicardiale contouren in cine MRI-beelden.

MR tagging maakt een volledige beschrijving van wandbeweging mogelijk, niet alleen van de myocardcontouren, maar voor een continuüm aan posities in het myocard. De met MR tagging aangebrachte spatiële patronen volgen de contractie van het hart, hetgeen een kwantitatieve bepaling van de myocardvervorming mogelijk maakt. Hieruit kan automatisch een snelheidsveld worden afgeleid door gebruik te maken van een multi-schaal optic flow methode. Deze techniek doet geen aannames over een constante pixelintensiteit in de tijd, maar gaat uit van een constante integraal van pixelintensiteiten binnen een regio (behoud van “intensiteitsmassa”). Als zodanig is de methode relatief robuust met betrekking tot het typische probleem van vervagende streep patronen in MR tagging in de hartcyclus.

In Hoofdstuk 2 wordt de voorgestelde optic flow techniek vergeleken met snelheidsgecodeerde MRI (VEC-MRI). Resultaten tonen een sterke correlatie in de radiële richting, maar niet in de tangentiële richting. De correlatie is sterker voor snelheidsvectoren in de systolische fase dan die in de diastolische fase. Om dit probleem op te lossen zijn nog verdere algoritmische verbeteringen nodig, bijvoorbeeld door het optic-flow veld te berekenen in het frequentiedomein in plaats van het spatiële domein [1, 2].

MR tagging is nuttig voor de analyse van myocardcontractiliteit. In de klinische praktijk is MR tagging momenteel niet opgenomen in routine diagnostische protocollen voor ischemische hartziekten. Om die reden hebben we de focus van dit onderzoek verlegd naar de mogelijkheid om myocardcontractie te karakteriseren uit cine MRI-beelden, in plaats van uit MR tagging.

Om de globale en lokale functie van het LV myocard te analyseren in cine-MRI zijn de endo- en epicardiale contouren vereist, zowel in ED als ES. Op basis hiervan kunnen parameters als ejectiefraction, wandverdikking, wanddikte en slagvolume worden berekend. Om de contractie van het myocard te karakteriseren met behulp van statistische modellen, combineren we deze contouren in een vormparametrisatie van myocardcontractie, waarbij landmark punten worden bemonsterd langs equi-angulaire intervallen om puntcorrespondentie tussen contouren te bewerkstelligen. In Hoofdstuk 3 werd onderzocht of het



mogelijk is om met deze vormparametrisatie de contractie van 42 normale vrijwilligers automatisch te onderscheiden van 47 patiënten met ischemische hartziekten. Twee lineair generatieve modellen werden gebruikt om de vormbeschrijvingen te ontbinden in componenten: Principal Component Analysis (PCA) en Independent Component Analysis (ICA). Wat betreft de vormeigenvariëtes leverde PCA globale vormvariëtes op, waar ICA meer lokale vormvariëtes genereerde. Qua onderscheidend vermogen tussen normalen en patiënten gold dat voor PCA alleen de 1e component al voldoende was om beide klassen te onderscheiden. Voor het ICA model gold dat 27 van de 35 componenten (77.14%) componenten nodig waren om hetzelfde onderscheidend vermogen te realiseren. Hieruit kan worden geconcludeerd dat PCA een compactere vormdecompositie oplevert dan ICA.

Voor classificatiedoeleinden kan de PCA decompositie de twee groepen alleen scheiden op globale vormverschillen. Uit de onderscheidende componenten kan geen geometrische interpretatie van het classificatieresultaat worden afgeleid. ICA genereert een minder compacte vormrepresentatie dan PCA, omdat de vormvariatie gelijkmatig over alle componenten is verdeeld. De ICA decompositie daarentegen onderscheidt niet alleen de twee groepen, maar kan ook de positie van de onderscheidende vormverschillen lokaliseren. Deze lokaliteitseigenschap maakt ICA geschikter dan PCA voor het detecteren en lokaliseren van regionale wandbewegingsafwijkingen. Op basis van deze observatie is ICA in de verdere hoofdstukken gekozen als vormdecompositie om lokale vormkenmerken uit myocardvormen af te leiden.

## **9.2 Automatische detectie van afwijkingen in regionale wandbeweging van het LV**

Het tweede doel van dit proefschrift was het ontwikkelen van een algoritme voor automatische detectie en lokalisatie van afwijkingen in LV regionale wandbeweging. Aangezien een Independent Component intrinsiek de lokale geometrie beschrijft van de vormparametrisatie, kan detectie van lokale regionale wandbewegingsstoornissen worden uitgevoerd door “abnormale componenten” te identificeren: dit zijn componenten waarvan de coëfficiënten buiten de op gezonde proefpersonen getrainde statistisch plausibele limieten vallen. Dit concept is beschreven in Hoofdstuk 4, waarbij de kansverdelingen werden geschat op basis van de aanname van een normale kansverdeling. Klassificatiegrenzen werden gedefiniëerd op 99.7% range, of  $\pm 3$  de standaardafwijking.

Een kwalitatieve validatie van deze automatische RWMA methode werd uitgevoerd op MRI beelden van zes infarctpatiënten. De afwijkende componentcoëfficiënten werden geprojecteerd op het myocard in de cine MRI beelden met behulp van een kleurcodering, die is afgeleid van een combinatie van de IC coëfficiëntwaarden, en een vergelijking werd gemaakt met Delayed Enhancement MRI. In alle zes patiënten was een goede overeenkomst zichtbaar tussen de als abnormaal gedetecteerde segmenten en de hyper-enhanced gebieden in de Delayed Enhancement MRI.

De studie in Hoofdstuk 4 liet zien dat de ICA-gebaseerde detectie in staat is om regionale wandbewegingsafwijkingen te herkennen en te lokaliseren. In Hoofdstuk 6 werd de kwantificatie van RWMA gebaseerd op geschatte kansverdelingen, en werd het proces van transformeren van componenten naar het spatiële domein verbeterd. De kansverdelin-

gen van de modelcoëfficiënten van gezonde personen werden omgerekend in kansverdelingen per landmarkpunt; deze propagatie van kansverdelingen is alleen mogelijk door de ICA eigenschap van statistische onafhankelijkheid tussen de componenten. Deze propagatie geeft voor elk landmarkpunt een kansverdeling, die wordt geschat op basis van alle ICs, waardoor contextinformatie uit naastgelegen landmarks geïntegreerd wordt.

Hoofdstuk 6 beschrijft een kwantitatieve validatie op basis van kruisvalidatie. Een vergelijking met visuele wandbewegingsscores werd gemaakt met wandverdikking als referentie, waarbij de automatische RWMA techniek significant beter scoorde. Met visuele wandbewegingsscores als referentie scoort de automatische detectie licht beter dan wandverdikkingsmetingen. Deze studie toonde de potentie aan van de ICA methode voor het automatisch detecteren van myocardsegmenten met abnormale regionale wandbeweging.

### 9.3 Automatische bepaling van functionele verbeteringen in wandbeweging

Het laatste onderzoeksdoel van dit proefschrift was het bepalen van de voorspellende waarde van de automatische RWMA detectie door deze te correleren met andere prognostische indices voor het vermogen tot herstel van het myocard na interventie (viabiliteit). LV contouren in dobutamine stress MR (DSMR) beelden werden gebruikt in de automatische RWMA detectie, en vergeleken met automatisch berekende RWMA waarden in rust. Onderzoekshypothese was dat als de contour sets uit verschillende stressniveaus worden vergeleken, verschillen in automatische RWMA waarden indicatief kunnen zijn voor myocardviabiliteit.

Hoofdstuk 5 onderzocht de verschillen in automatische RWMA waarden tussen rust en stress. Een kwalitatieve evaluatie in zes patiënten met ischemische hartziekten toonde aan dat een verbetering in contractie van rust naar stress correspondeerde met een verlaging van de automatische RWMA waarde, die de mate van wandbewegingsabnormaliteit uitdrukt. In andere woorden, een verbetering in contractiliteit tussen rust en stress correleerde met een statistisch normalere contractie, en omgekeerd. Interessante bevinding was ook dat de methode een verbetering in wandverdikking als abnormaal klassificeerde in geval van diskinetische wandbeweging. Dit geeft aan dat de automatische RWMA methode niet alleen wandverdikking beschouwt, maar tegelijk ook wandbeweging.

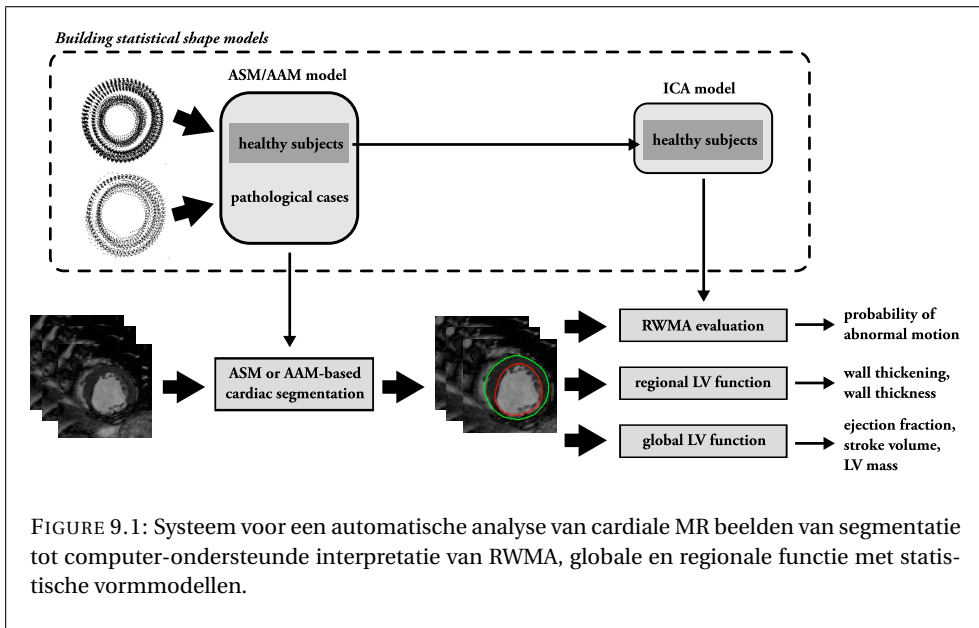
In Hoofdstuk 7 werd deze techniek verder verbeterd om een betere vergelijking tussen contouren uit de beide stressniveaus mogelijk te maken. Na rigide (Procrustes) en niet-rigide registratie, werd een tweede niet-rigide registratie toegepast om vormverschillen tussen het epicardcontouren te elimineren. Alleen relatieve verschillen in endocardbeweging ten opzichte van het epicard werden zo gemodelleerd. Zonder deze aanvullende registratie kunnen er fout-positieve klassificaties optreden omdat sterke contracties in stress anders als abnormaal kunnen worden geklassificeerd.

Idealiter is longitudinale pre- en post-revascularisatie data nodig om een mogelijke prognostische indicator voor myocardviabiliteit te valideren. Dergelijke data was niet voorhanden. Daarom werd in Hoofdstuk 7 een vergelijking beschreven met infarct transmuraliteit afgeleid uit Delayed Enhancement MRI, omdat deze maat correleert met de



mogelijkheid tot functioneel herstel na revascularisatie [3]. De automatische RWMA waarden bleken op alle slice niveaus sterk te correleren met infarct transmuraliteit, waarbij de RWMA waarden monotoon afnamen bij een toenemende infarct transmuraliteit. De methode gaf een hoge successcore bij de detectie van myocardsegmenten met littekenweefsel, zoals bevestigd in DE MRI beelden.

## 9.4 Vervolonderzoek



Dit proefschrift beschrijft een aantal stappen in de ontwikkeling van een systeem voor automatische analyse van wandbeweging in cine MRI ter ondersteuning van de diagnose van ischemische hartziekten. De beschreven methoden kunnen op meerdere manieren worden verbeterd en uitgebreid. Dit betreft de uitbreiding van het vormmodel naar drie dimensies, het toevoegen van meerdere tijdpunten in de hartcyclus, en een validatie op basis van pre- and post revascularisatie data om myocardviabiliteit te identificeren.

De gepresenteerde technieken om automatisch wandbeweging te klassificeren als normaal of abnormaal zouden goed kunnen worden ingepast in een volautomatisch systeem voor beslissingsondersteuning in cardiale MRI. De in dit proefschrift beschreven technieken maken gebruik van handmatig getekende contouren; dit is gedaan om een mogelijk verstoring effect van segmentatiefouten uit te sluiten. Met een robuuste automatische segmentatiemethode kunnen deze contouren ook automatisch worden aangeleverd, bijvoorbeeld door gebruik te maken van segmentatietechnieken gebaseerd op statistische vormmodellen zoals Active Shape Models [4–6] en Active Appearance Models [7, 8]. De ASM en AAM parameters zouden dan direct kunnen dienen als invoer voor de in dit

proefschrift beschreven CAD technieken. Figuur 9.1 illustreert hoe op deze manier een volautomatisch CAD systeem voor cardiale MRI zou kunnen worden gerealiseerd.

De in dit proefschrift beschreven CAD methode voor automatische RWMA analyse is gebaseerd op contouren uit cardiale MRI, maar het onderliggende algoritme is niet afhankelijk van de gebruikte beeldmodaliteit. De beschreven methoden zouden daarom ook toegepast kunnen worden voor bijvoorbeeld de detectie van RWMA in echocardiografie, maar dit vereist nadere experimentele studies.

De diagnostische resultaten van de automatische RWMA analyse zouden ook kunnen worden gecombineerd met andere beeldmodaliteiten, bijvoorbeeld in een combinatie van cine MRI en MR perfusie imaging, FDG-PET imaging, gated SPECT imaging en/of MR infarct imaging (DE-MRI). Ook zou myocard deformatie kunnen worden afgeleid uit MR tagging, strain-encoded MRI, velocity-encoded MR of echo-doppler beelden van het myocard. De integratie van informatie over contractie, vervorming en perfusie zou een volgende stap kunnen zijn in de ontwikkeling van een compleet CAD systeem voor ondersteuning van de diagnostiek van ischemische hartziekten.

## 9.5 References

- [1] L. Florack, H. van Assen, and A. Suinesiaputra, "Dense multiscale motion extraction from cardiac cine MR tagging using HARP technology," in *IEEE 11th International Conference on Computer Vision, ICCV, 2007*, pp. 1–8.
- [2] H. C. van Assen, L. M. Florack, A. Suinesiaputra, J. J. Westenberg, and B. M. ter Haar Romeny, "Purely evidence based multiscale cardiac tracking using optic flow," in *Proc. Computational Biomechanics for Medicine II. A MICCAI 2007 Workshop, 2007*.
- [3] T. A. M. Kaandorp, J. J. Bax, J. D. Schuijf, E. P. Viergever, E. E. van Der Wall, A. de Roos, and H. J. Lamb, "Head-to-head comparison between contrast-enhanced magnetic resonance imaging and dobutamine magnetic resonance imaging in men with ischemic cardiomyopathy," *Am J Cardiol*, vol. 93, no. 12, pp. 1461–4, Jun 2004.
- [4] H. van Assen, M. Danilouchkine, A. Frangi, S. Ordas, J. Westenberg, J. Reiber, and B. Lelieveldt, "SPASM: A 3D-ASM for segmentation of sparse and arbitrarily oriented cardiac MRI data," *Medical Image Analysis*, vol. 10, no. 2, pp. 286–303, APR 2006.
- [5] H. C. van Assen, M. G. Danilouchkine, M. S. Dirksen, J. H. C. Reiber, and B. P. F. Lelieveldt, "A 3-D active shape model driven by fuzzy inference: application to cardiac CT and MR," *IEEE Trans Inf Technol Biomed*, vol. 12, no. 5, pp. 595–605, Sep 2008.
- [6] M. Uzumcu, R. J. van der Geest, M. Sonka, H. J. Lamb, J. H. C. Reiber, and B. P. F. Lelieveldt, "Multiview active appearance models for simultaneous segmentation of cardiac 2- and 4-chamber long-axis magnetic resonance images," *Invest Radiol*, vol. 40, no. 4, pp. 195–203, Apr 2005.
- [7] S. C. Mitchell, J. G. Bosch, B. P. F. Lelieveldt, R. J. van der Geest, J. H. C. Reiber, and M. Sonka, "3-D active appearance models: segmentation of cardiac MR and ultrasound images," *IEEE Trans Med Imaging*, vol. 21, no. 9, pp. 1167–1178, Sep 2002.
- [8] E. Oost, G. Koning, M. Sonka, P. V. Oemrawsingh, J. H. C. Reiber, and B. P. F. Lelieveldt, "Automated contour detection in X-ray left ventricular angiograms using multiview active appearance



models and dynamic programming," *IEEE Trans Med Imaging*, vol. 25, no. 9, pp. 1158–1171, Sep 2006.

## PUBLICATIONS

### International journal

**A. Suinesiaputra**, A. F. Frangi, T. A. M. Kaandorp, H. J. Lamb, J. J. Bax, J. H. C. Reiber, and B. P. F. Lelieveldt, “Automated detection of regional wall motion abnormalities based on a statistical model applied to multi-slice short-axis cardiac MR images,” *IEEE Transactions on Medical Imaging*, vol. 4, no. 28, pp. 595–607, Apr 2009.

**A. Suinesiaputra**, A. F. Frangi, T. A. M. Kaandorp, H. J. Lamb, J. J. Bax, J. H. C. Reiber, and B. P. F. Lelieveldt, “An automated regional wall motion abnormality detection by combining rest and stress cardiac MRI: Correlation with infarct transmuralty from contrast-enhanced MRI,” *submitted*.

### Book chapter

B. M. ter Haar Romeny, L. M. J. Florack, and **A. Suinesiaputra**, *Front-End Vision and Multi-Scale Image Analysis*. Springer, 2003, ch. Multi-scale optic flow, pp. 285–310.

### Peer-reviewed conference proceedings

**A. Suinesiaputra**, L. M. J. Florack, J. J. M. Westenberg, B. M. ter Haar Romeny, J. H. C. Reiber, and B. P. F. Lelieveldt, “Optic SFlow computation from cardiac MR tagging using a multiscale differential method: A comparative study with velocity-encoded MRI,” in *Medical Image Computing and Computer-Assisted Intervention — MICCAI 2003*, Lecture Notes in Computer Science Series vol. 2878, R. E. Ellis and T. M. Peters, Eds., Springer, Nov 2003, pp. 483–490.

**A. Suinesiaputra**, A. F. Frangi, M. Üzümcü, J. H. C. Reiber, and B. P. F. Lelieveldt, “Extraction of myocardial contractility patterns from short-axis MR images using independent component analysis,” in *Computer Vision and Mathematical Methods in Medical and Biomedical Image Analysis*, Lecture Notes in Computer Science Series vol. 3117, M. Sonka, I. A. Kakadiaris, and J. Kybic, Eds., Springer, 2004, pp. 75–86.

**A. Suinesiaputra**, M. Üzümcü, A. F. Frangi, J. H. C. Reiber, and B. P. F. Lelieveldt, “Detecting regional abnormal cardiac contraction in short-axis MR images using independent component analysis,” in *Medical Image Computing and Computer-Assisted Intervention — MICCAI 2004*, Lecture Notes in Computer Science Series vol. 3216, C. Barillot, D. R. Haynor, and P. Hellier, Eds., Springer, Oct 2004, pp. 737–744.

**A. Suinesiaputra**, A. F. Frangi, H. J. Lamb, J. H. C. Reiber, and B. P. F. Lelieveldt, “Automatic prediction of myocardial contractility improvement in stress MRI using shape morphometrics with independent component analysis,” in *Proc. of 19th Information Processing in Medical Imaging 2005*, Lecture Notes in Computer Science Series vol. 3565, G. E. Christensen and M. Sonka, Eds. Springer-Verlag, 2005, pp. 321–332.

L. Florack, H. van Assen, and **A. Suinesiaputra**, “Dense multiscale motion extraction from cardiac cine MR tagging using HARP technology,” in *IEEE 11th International Conference on Computer Vision (ICCV)*, 2007, pp. 1–8.

## Conference proceedings

H. C. van Assen, L. M. Florack, **A. Suinesiaputra**, J. J. Westenberg, and B. M. ter Haar Romeny, “Purely evidence based multiscale cardiac tracking using optic flow,” in *Proc. Computational Biomechanics for Medicine II. A MICCAI 2007 Workshop*, 2007.

N. Baka, J. Milles, E. A. Hendriks, **A. Suinesiaputra**, M. Jerosch-Herold, J. H. C. Reiber, and B. P. F. Lelieveldt, “Segmentation of myocardial perfusion MR sequences with multi-band active appearance models driven by spatial and temporal features,” in *SPIE Medical Imaging*, vol. 6914, San Diego, USA, Apr. 2008, p. 15.

## Published abstract

**A. Suinesiaputra**, L. M. J. Florack, and B. M. ter Haar Romeny, “Multiscale optic flow analysis of MR tagging heart image sequences,” *European Journal of Medical Physics*, pp. 19–48, 2003.

## ACKNOWLEDGEMENTS

This thesis describes results of research that was carried out within the KGB section (Dutch abbreviation for knowledge-guided image processing) of LKEB (Dutch abbreviation for Laboratory for Clinical and Experimental Image Processing), Department of Radiology, Leiden University Medical Center, the Netherlands. The research was performed under the supervision of prof. dr. ir. J.H.C. Reiber and dr. ir. B.P.F. Lelieveldt, and was financed by the Dutch Science Foundation (NWO). Throughout the odyssey of my PhD quest, I am deeply indebted to my colleagues, friends and families for physical and moral support, guidance and assistance. My greatest gratitude to all of them

I would like to express my sincere gratitude to prof. dr. ir. Bart ter Haar Romeny and prof. dr. Luc Florack, who always put their confidence in me from the very beginning. Their support has resulted in my first scientific paper during the first year of my PhD study. I would also like to thank Jos Westenberg for providing me his VEC-MRI data for this publication.

During the rest of my PhD work, I am very grateful to have collaboration with dr. Alejandro Frangi. All remaining chapters of this thesis are the products of a fruitful collaboration with him. Thank you Alex for letting me stay at your group for two months and for giving me a long-distance probabilistic course on Skype. I would also like to thank Dirk Kaandorp for providing the cardiac MR data of his patients and also their visual score assessment, and also Hildo Lamb for his valuable input in helping me understand the clinical problems in this research.

It is my pleasure to have been working at LKEB, especially to witness two generations of KGB section members. Therefore I would like to acknowledge Mehmet, Hansa, Mike, Elco, Julien, Maribel and Mark for making it such a *gezellige* place to work. Many thanks also to Nora, Martin, Vikas, Meng, Peter Kok, Artem and Marta for their scientific drawings on the whiteboard.

In general, I would like to thank all my former and current LKEB colleagues, whom I cannot all mention here. Particularly for Jasper, Patrick and Andrei, thank you for your patience in accepting me as your roommate. I would like also to thank Rob van der Geest for adopting me as a post-doc in the MRI section, while I was still busy finishing this thesis.

I would like to thank Bertie, Fred and Michele for their technical and administrative supports. My special gratitude goes to Istjar Broeijer, my former personal adviser at LUMC. Thank you for helping me (and my wife) dealing with the Dutch foreign police in Eindhoven who lost our residence permit applications.

Upon completion of this thesis, I would like to thank Els Stoopman who has smoothed

the administrative processes. Especially for my nephew, Khairi, who has given up his end-year school vacation term for drawing the cover page, Azar Mawardi and Yusdi Gazali, who have helped him, thank you all for that.

I am very grateful to be surrounded by my family who has given me tremendous love and supports that cannot be written by words. *Kami cuma bisa berdo'a, Allah melimpahkan kasih sayang buat papah/bapak dan mamah/mamak dalam kehidupan dunia dan akhirat.* Your material supports, your continuous praying and your abundance love are our banisters of life that we always be grateful to.

In the same light, I would like to thank all my brothers-in-law and sisters-in-law for their instant help whenever we are in trouble, regardless where and how far we are. For Bang Rhiza, Kak Ika, Bang Warli, Nimah, Bang Hakim, Kak Upha, Isan and Vita, *jazakallahu khairan kathira.* Also to Anggy, Dodo, Dita and Wendy. To all my nephews and nieces who always lighten our life, you are all so adorable.

## CURRICULUM VITAE

Avan Suinesiaputra was born in Jakarta, Indonesia on 7 April 1974. After completing his pre-university education (SMA) at SMA Negeri 3 Bandung, he studied computer science at the Department of Informatics Engineering, Institut Teknologi Bandung, Indonesia, in 1992. In 1998, he completed his final bachelor project on texture segmentation with Gabor wavelet transform. After two years working as an assistant lecturer in the same institute, he arrived in the Netherlands to continue his study at the Section of Computational Science group, University of Amsterdam, in 2000. He finished his master of science in the computational science program *cum laude* in 2002. In his master studies, he finalized his thesis entitled “Multiscale optic flow analysis for magnetic resonance imaging” at the Department of Biomedical Engineering, Technische Universiteit Eindhoven. Starting in September 2002, he joined the Laboratory for Clinical and Experimental Image Processing (LKEB) at Leiden University Medical Center to work as a PhD student. His main topic of research was developing a novel method to integrate information in different cardiac MR protocols towards a one-stop shop cardiac MRI analysis. The results of his research are manifested in this thesis with the focus on building a computer-aided diagnosis method for cardiac MRI. Currently, he is still working at LKEB as a post-doctoral researcher. He is developing a 3D semi-automated vessel segmentation method from MR angiographic data. His main research interests include statistical shape modeling of medical data, morphometric analysis, probabilistic methods for computer-aided diagnosis, and model-based image analysis.



*Words are so inapt  
to express my gratitude  
for your sincere benevolence,  
for your deep understanding,  
and for your affectionate solicitude.*

*Only to God  
that I always be grateful to,  
for having you.*